CANMET

Canada Centre for Mineral and Energy Technology

Centre canadien de la technologie des minéraux et de l'énergie

Efficiency and Alternative Energy Technology Branch

Direction de la technologie de l'efficacité énergétique et des énergies de remplacement

DEVELOPMENT OF LARGE-AREA AMORPHOUS SILICON PHOTOVOLTAIC CELLS ON A FLEXIBLE SUBSTRATE

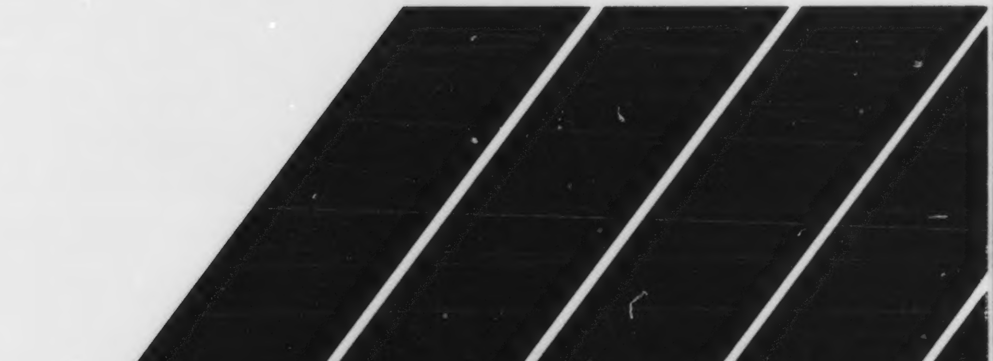

Energy, Mines and Resources Canada
Énergie, Mines et Ressources Canada

Canada

THE ENERGY OF OUR RESOURCES · THE POWER OF OUR IDEAS

L'ENERGIE DE NOS RESSOURCES · NOTRE FORCE CREATRICE

DEVELOPMENT OF LARGE-AREA AMORPHOUS SILICON PHOTOVOLTAIC CELLS ON A FLEXIBLE SUBSTRATE

PREPARED FOR:

Efficiency and Alternative Energy Technology Branch
Energy, Mines and Resources Canada
Ottawa, Ont.
DSS Contract No. 23283-7-6140
December, 1989

PREPARED BY:

Le Centre de Développement Technologique
de L'École Polytechnique de Montréal
Campus de l'Université de Montréal
C.P. 6079, Succursale A
Montréal, Qué.
H3C 3A7

SCIENTIFIC AUTHORITY:

Jimmy Royer
Efficiency and Alternative Energy Technology Branch
Energy, Mines and Resources Canada
580 Booth Street
Ottawa, Ont.
K1A 0E4

155 pp

MICROMEDIA

91-01227/

CITATION

Currie, J.F., École Polytechnique de Montréal. Development of Large-Area Amorphous Silicon Photovoltaic Cells on a Flexible Substrate. DSS Contract No. 23283-7-6140. Efficiency and Alternative Energy Technology Branch, Energy, Mines and Resources Canada, Ottawa, Ontario. 1989 (96 pp.)

Copies of this report may be obtained through the following:

Efficiency and Alternative Energy Technology Branch
Energy, Mines and Resources Canada
580 Booth Street, 7th Floor
Ottawa, Ont.
K1A 0E4

or

Document Delivery Service
Library and Documentation Services Division
CANMET
Energy, Mines and Resources Canada
562 Booth Street
Ottawa, Ont.
K1A 0G1

DISCLAIMER

This report is distributed for informational purposes only and does not necessarily reflect the views of the Government of Canada nor constitute an endorsement of any commercial product or person. Neither Canada nor its ministers, officers, employees or agents makes any warranty in respect to this report or assumes any liability arising out of this report.

NOTE

Funding for this project was provided by the Office of Energy Research and Development, Energy, Mines and Resources Canada.

© Minister of Supply & Services Canada 1990
Catalogue No. M91-7/118-1990E
ISBN. 0-662-18164-6

TABLE OF CONTENTS

Page

EXECUTIVE SUMMARY.. v

RÉSUMÉ... vi

1. INTRODUCTION.. 1

2. HIGH PURITY a-Si:H...................................... 3

   2.1 Deposition.. 3
   2.2 Electro-optical characterization.................... 5
      2.2.1 Current vs. voltage measurements as a function of temperature.................. 6
      2.2.2 C-V: Capacitance vs. voltage measurements............................. 6
      2.2.3 PC: Photoconductivity.......................... 7
      2.2.4 TOF: Time-of-fight mobility.................... 7
      2.2.5 FRA: Frequency response analysis............... 13

3. DUAL-MODE FREQUENCY DEPOSITION OF a-Si:H FILMS.......... 16

   3.1 Deposition.. 16
   3.3 Infrared characterization........................... 26

4. DOPING a-Si:H BY COSPUTTERING........................... 33

   4.1 Deposition.. 33
      4.1.1 p-Type doping.................................. 33
      4.1.2 n-Type doping.................................. 39
   4.2 Surface analysis.................................... 41

5. DEVICE FABRICATION...................................... 49

   5.1 Preparation... 49
   5.2 Electro-optical characterization of p-i-n devices... 51

Page

5.3 Identification of the sources of difficulty in obtaining high quality devices.......................... 54

6. DOPING BY THERMAL DIFFUSION..................................... 71

6.1 Preparation... 71
6.2 Electro-optical characterization........................ 71

7. GAS PHASE DOPING... 74

7.1 Modification of film deposition laboratory.............. 74
7.1.1 Gas phase doping of a-Si:H......................... 74
7.2 Deposition.. 77
7.3 Studies of doping mechanisms............................ 79
7.3.1 Effect of coordination (bond angles)............. 79
7.3.2 Band bending..................................... 79
7.3.3 Fermi level shifts of P-doped a-Si:H............. 82
7.4 Electrical characterization of amorphous silicon........ 91
7.4.1 I-V-T current versus voltage measurements for gas-phase doped samples doped.................... 91
7.4.2 FRA: A.C. impedance measurements for intrinsic a-Si:H prepared by simultaneous RF and microwave irradiation............................ 95

8. CONCLUSIONS... 95

RÉFÉRENCES... R-1

APPENDIX A - Key extracts of Z. Lu's Ph.D. theses on the fundamental doping mechanisms in a-Si:H............. A-1

APPENDIX B - Members of the Thin Film Group (GCM)................ B-1

EXECUTIVE SUMMARY

The work summarized herein was undertaken by the Thin Film Group of the École Polytechnique/Université de Montréal with a specific goal in mind. It was clear to us, even before the outset, that, with our limited resources, we could not hope to compete with industries which had previously dedicated large amounts of funding and manpower to the production of inexpensive, large scale photovoltaic devices. Rather, it was our hope that we could do what they were prevented from doing because of time restraints: we hoped to explore a technique which previous work in our laboratory had indicated was an attractive candidate for low cost, controlled, non-toxic doping. This technique is the cosputtering of dopant metal into the silane gas plasma from which the hydrogenated amorphous silicon is being deposited.

While we were able to show doping by this method, funding constraints and product orientation precluded attempts at optimization, for the time being. We reoriented our direction toward the already proven gas phase (i.e., diborane or phosphine) technique. At the termination of this project, we had demonstrated gas phase doping, and had made significant studies in describing both the doping mechanisms and the effect of dopant on the film surface.

Schottky cells have been produced with efficiencies of 5.9 %, while our best p-i-n cells have efficiencies of only 2.8 %. Our data suggest this latter value to be due to problems with Ohmic contact to the p-level. We believe that, should further funding become available, the use of more concentrated diborane dopant feed stock will raise the p-i-n efficiency to the 10 % range.

RÉSUMÉ

Les travaux résumés ici ont été entrepris dans un but bien précis par le Groupe des couches minces de l'École Polytechnique/Université de Montréal. Même avant le début des travaux, il nous paraissait évident que nos ressources limitées ne nous permettraient pas d'entrer en concurrence avec des industries qui avaient auparavant consacré d'importantes ressources financières et humains à la production sur grande échelle de dispositifs photovoltaïques peu coûteux. Nous espérions plutôt pouvoir faire ce que ces industries ne pouvaient faire en raision de contraintes de temps : étudier une technique qui, selon des travaux effectués antérieurement dans notre laboratoire, semblait bien se prêter à un dopage non toxique contrôlé de faible coût. Cette technique est la codiffusion de métal dopant dans un plasma de silane à partir duquel est effectué un dépôt de silicium amorphe hydrogéné.

Bien qu'il ait été possible de démontrer un dopage selon cette méthode, des contraintes de financement et d'orientation des produits empêchent pour le moment toute tentative d'optimisation. Nous avons réorienté nos travaux vers la technique de la phase gazeuse (diborane ou phosphine), qui a déjà fait ses preuves. A la fin du projet, nous avons démontré le dopage en phase gazeuse, et nous avons mené des études élaborées en vue de décrire les mécanismes de dopage et l'effet du dopant à la surface de la couche.

Des cellules Scottky présentant une efficacité de 5.9 % ont été produites, alors que nos meilleures cellules p-i-n n'offrent une efficacité que de 2.8 %. Nos données rélèvent que cette dernière valeur résulte de problèmes de contact ohmmique au niveau p. Si des fonds supplémentaires deviennent disponibles, nous croyons que l'utilisation d'un dopant de diborane plus concentré permettra de porter l'efficacité des couches p-i-n dans la plage de 10 %.

1. INTRODUCTION

This final report attempts a logical, rather than a historical, presentation of the research on hydrogenated amorphous silicon photovoltaic cells carried out over a period of 2 1/2 years by the Thin Film Group of the École Polytechnique/Université de Montréal. The historical version is contained in bimonthly progress reports issued to the scientific officer of EMR/photovoltaics division. It was our initial hope that a novel technique of doping, that of cosputtering a metal during plasma deposition, could be improved to the point where it could be incorporated into the manufacture of p-i-n solar cells and the technology transferred to TPK International, of Nepéan, Ontario, a manufacturer of crystalline silicon solar cells.

This was ultimately found to be unfeasible because:

a) the solar conversion efficiency was limited by the cosputtering process, through the introduction of traps, and

b) TPK International went into receivership.

Initial attempts at the thermal diffusion of surface-deposited metals offered no advantages, and were not pursued.

At this point, we received permission from EMR to:

a) redirect our efforts to gas-phase doping, and
b) concentrate on understanding the mechanism(s) involved.

Here, we were significantly more successful, proposing a mechanism which accounts for all the features of gas phase doping (presently in the process of publication). We have shown that we obtain p-type doping for B_2H_6/SiH_4 reactant gas mixtures and n-type doping for PH_3/SiH_4 reactant gas mixtures, and how these are affected by plasma deposition parameters. We have also shown the significant effect of the surface due to contamination, and how the information derived may tell us something of the dopant.

This final report is set out in six chapters, covering the progression

Chapter 2. High purity a-Si:H - equal to the highest purity material manufactured by others.

Chapter 3. Dual-mode frequency deposition of a-Si:H - leading to good photovoltaic material deposited at high deposition rates.

Chapter 4. Doping a-Si:H by cosputtering - demonstrating our success in doping by the cosputtering of a metal into the reactant gas mixture.

Chapter 5. Device fabrication - indicating the limited success of producing p-i-n devices due to the introduction of traps by the cosputtering process.

Chapter 6. Doping by thermal diffusion - showing a lack of initial success.

Chapter 7. Gas phase doping - demonstrating our success with this method.

Our conclusions are given in chapter 8.

2. HIGH PURITY a-Si:H

2.1 Deposition

The first objective of the program was to demonstrate that our equipment and procedures produced high purity a-Si:H, and that this material had excellent electronic properties. The system used for this purpose, shown schematically in Figure 1, was a capacitively coupled arrangement of plane parallel electrodes, of 300 cm^2 surface, and 5 cm spacing. The vacuum system was constructed of stainless steel, and was operated with a base pressure of 10^{-8} Torr.

The best results were obtained under the following conditions:

- Substrate temperature:	300°C
- R.F. power:	5 to 60 Watts
- R.F. frequency:	100 KHz
- Pressure:	0.2 Torr
- D.C.Bias:	-80 to -300 V.

While good results were obtained with silane-argon mixtures, better results were obtained with pure silane, using a flow rate of 16 sccm. With the range of R.F. power indicated above, growth rates ranged from 0.3 $\mu m\ h^{-1}$ to 2 $\mu m\ h^{-1}$. Samples were grown on several different substrates: Corning 7059 glass, silicon wafers, and highly polished stainless steel. Thicknesses ranged from 0.5 to 15 μm. As the principal technique used for characterizing the quality of the films was time-of-flight mobility, thicker films, of 5 to 15 μm, were of greatest interest.

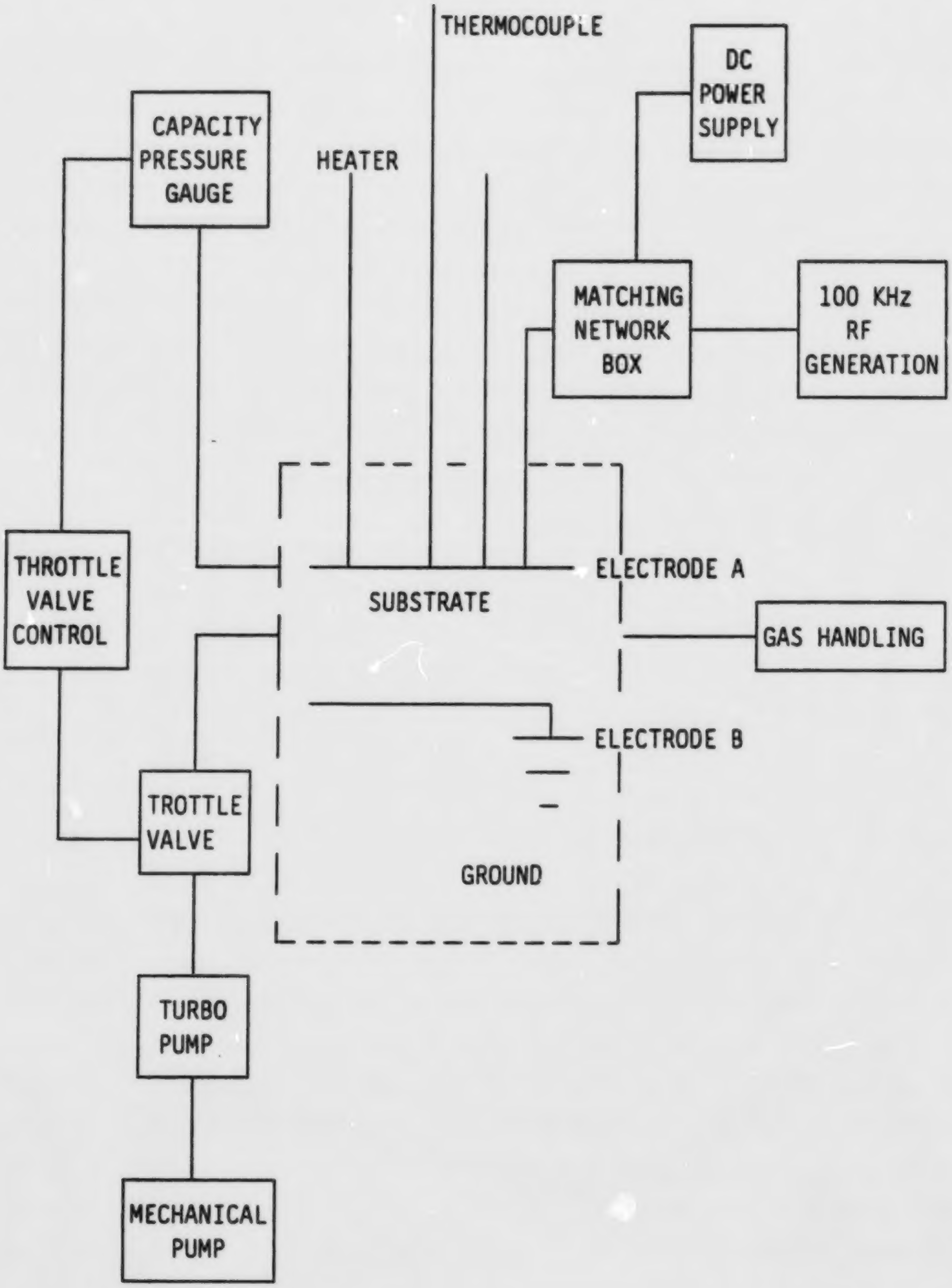
THERMOCOUPLE
DC POWER SUPPLY
CAPACITY PRESSURE GAUGE
HEATER
MATCHING NETWORK BOX
100 KHz RF GENERATION
THROTTLE VALVE CONTROL
ELECTRODE A
SUBSTRATE
GAS HANDLING
ELECTRODE B
TROTTLE VALVE
GROUND
TURBO PUMP
MECHANICAL PUMP

Figure 1 Schematic of apparatus used to deposit hydrogenated amorphous silicon by glow discharge in silane plasma.

The best samples had mobilities as high as those reported by Xerox, Palo Alto. These were prepared at the slowest rates, in accordance with our observations, and those of others, that high rates at radio frequencies lead to columnar material, and to a deterioration of sample properties. The samples with the highest mobilities were those prepared on the stainless steel sheet. This suggests that strains may play a significant part in sample properties.

Thus, the intrinsic material made in our laboratory is of quality comparable with that made anywhere else. Unfortunately, we suffer from the same difficulty as other laboratories; truly high quality material is made only at very low deposition rates. This is a serious problem for the production of photovoltaic material for commercial application. Our laboratory has, for many years, been involved in the study of the effect of plasma excitation frequency on deposition rates and on material quality. In particular, we have found that very much higher deposition rates can be obtained at microwave frequencies. Unfortunately, we have also found that this material is always columnar, and that it does not have good properties for photovoltaic applications. However, recent findings from our laboratory, reported later, indicate that these properties may be improved.

2.2 Electro-Optical Characterization

The following standard experimental methods have been used to characterize the amorphous silicon films:

a) Current versus voltage measurements as a function of temperature (I-V-T);

b) Capacitance versus voltage measurements: (C-V);

c) Photoconductivity measurements: (PC). In addition more extensive measurements were made on a selected number of samples by the following techniques;

d) Time-of-flight: (TOF);

e) Frequency response analysis: (FRA).

All of the above measurements are useful for the characterization of the intrinsic material. The TOF measurements require relatively thick samples, (>5 micron) which, for good quality intrinsic material, requires very long deposition times for sample fabrication. Because of this, a limited number of samples was studied by this technique.

2.2.1 Current vs voltage measurements as a function of temperature

A temperature-controlled sample chamber was used to obtain current-voltage curves at different temperatures of samples having a known coplanar electrode geometry, thus allowing the conductivity to be determined. An Arrhenius plot of $\ln(\sigma)$ versus $1/T$ then was used to extract an activation energy for the conduction process. The best intrinsic material yields room temperature conductivities of 10^{-9} $(\Omega\ \mathrm{cm})^{-1}$ and activation energies of about 0.7 eV, values very similar to those obtained in other laboratories.

2.2.2 C-V: Capacitance vs voltage measurements

We have not made extensive measurements using this technique during the term of this contract; however, a generalization of the technique, Frequency Response Analysis (FRA), has been used on selected samples and is described below.

2.2.3 PC: Photoconductivity

These measurements have been used to determine the ratio of the conductivities in the dark and under AM1 illumination (using semi-transparent Schottky barriers and coplanar electrodes). Typically the ratio $\sigma_{dark}/\sigma_{photo} > 10^4$ for good low deposition rate samples with no doping.

2.2.4 TOF: Time-of-flight mobility

In this technique, a short (1-3 ns) light flash of known intensity and photon energy illuminates a high impedance, (intrinsic or compensated) sample of amorphous silicon through a semi-transparent electrode. Using fast recording equipment, we measure the photocurrent response of the sample as a function of time under different experimental conditions. The parameters that are varied are the temperature, the voltage applied to the sample (and, hence, the electric field) and the incident light intensity. The TOF technique is probably the one most suited to determine the caracteristics of high impedance material. Since the proposed p-i-n device contains intrinsic material, it was deemed important to establish unequivocally the quality of our intrinsic material and to demonstrate our capability of fabricating it reproducibly.

Figure 2a shows a typical transient photocurrent of a high quality sample, 4.3 µm thick, where the transport is non-dispersive and the arrival time of the electron packet created by the absorption of the photons is easily visible. The transit time is also visible in Figure 2b which is a plot of the log of the photocurrent versus the log of the time. The mobility deduced from these data taken at 342 K was 2.2 $cm^2(Vs)^{-1}$. Figure 3 and 4 show similar curves for the same sample, this time taken at 184K. At this temperature, the transport is dispersive in nature and an equivalent transit time can only be determined from the log-log plot. In this case the mobility was found to be 0.03 $cm^2\ (Vs)^{-1}$. Figure 5 is an Arrhenius plot of the mobility

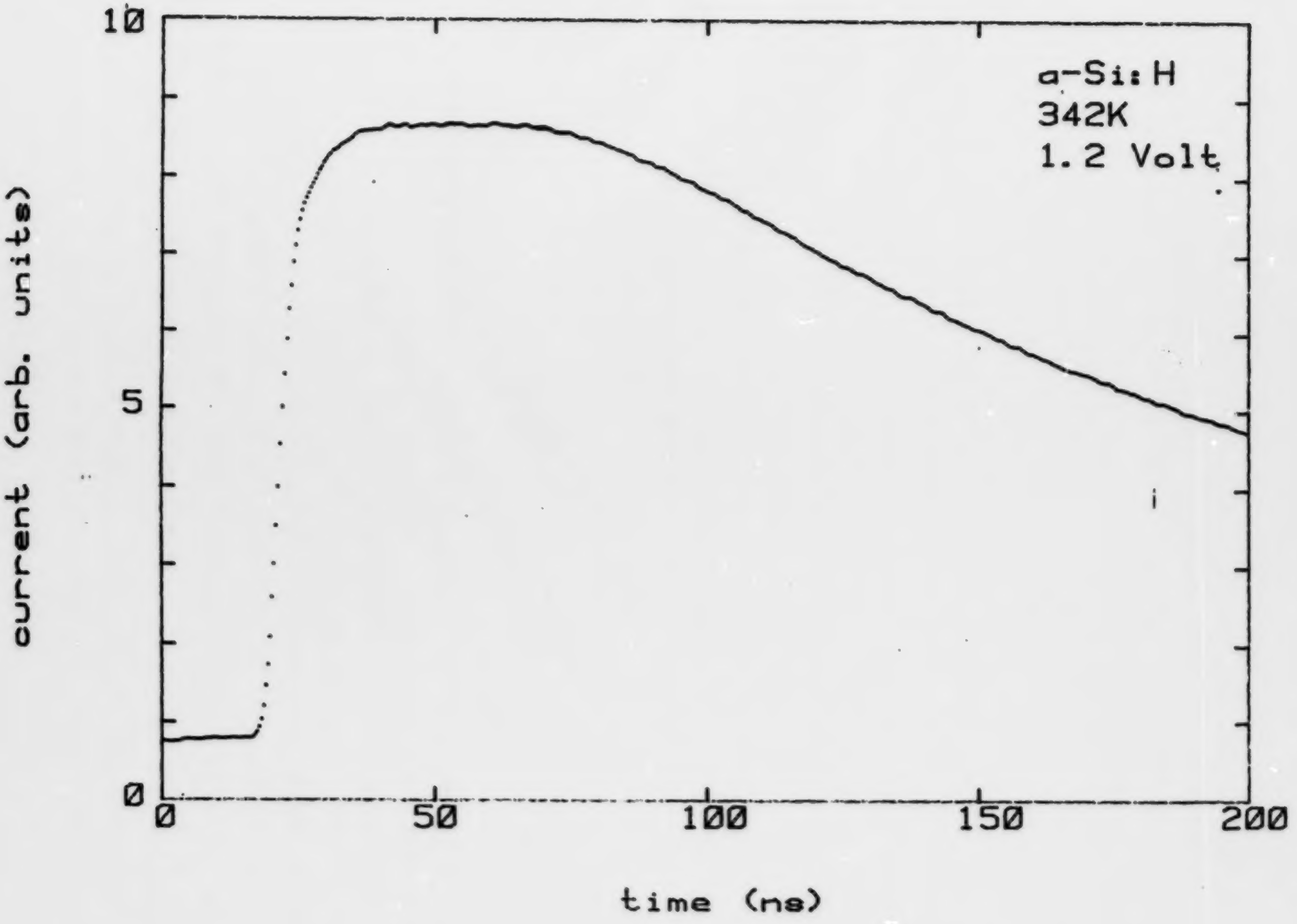

Figure 2a Time-of-flight current transient.

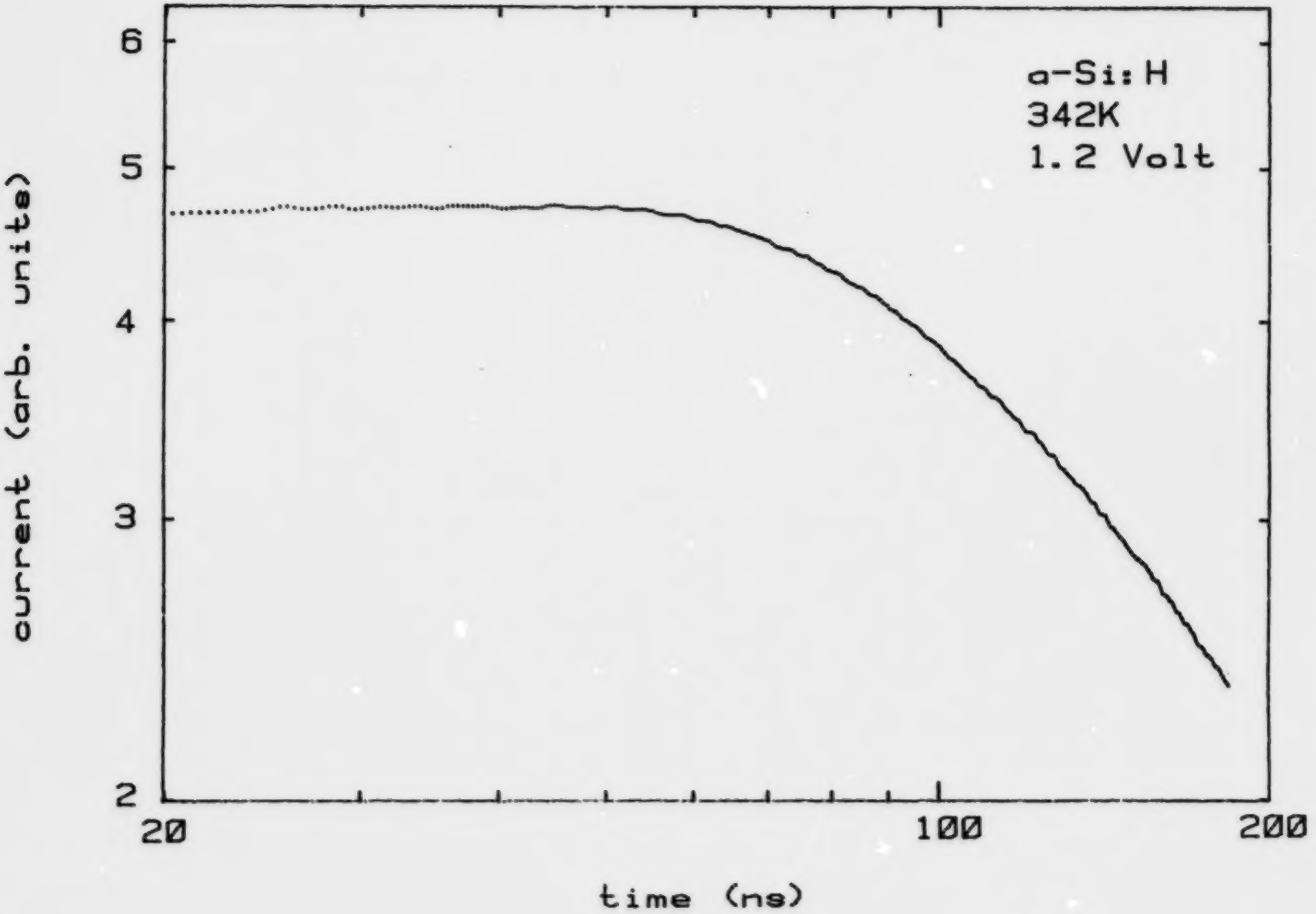

Figure 2b Log-log plot of figure 1.

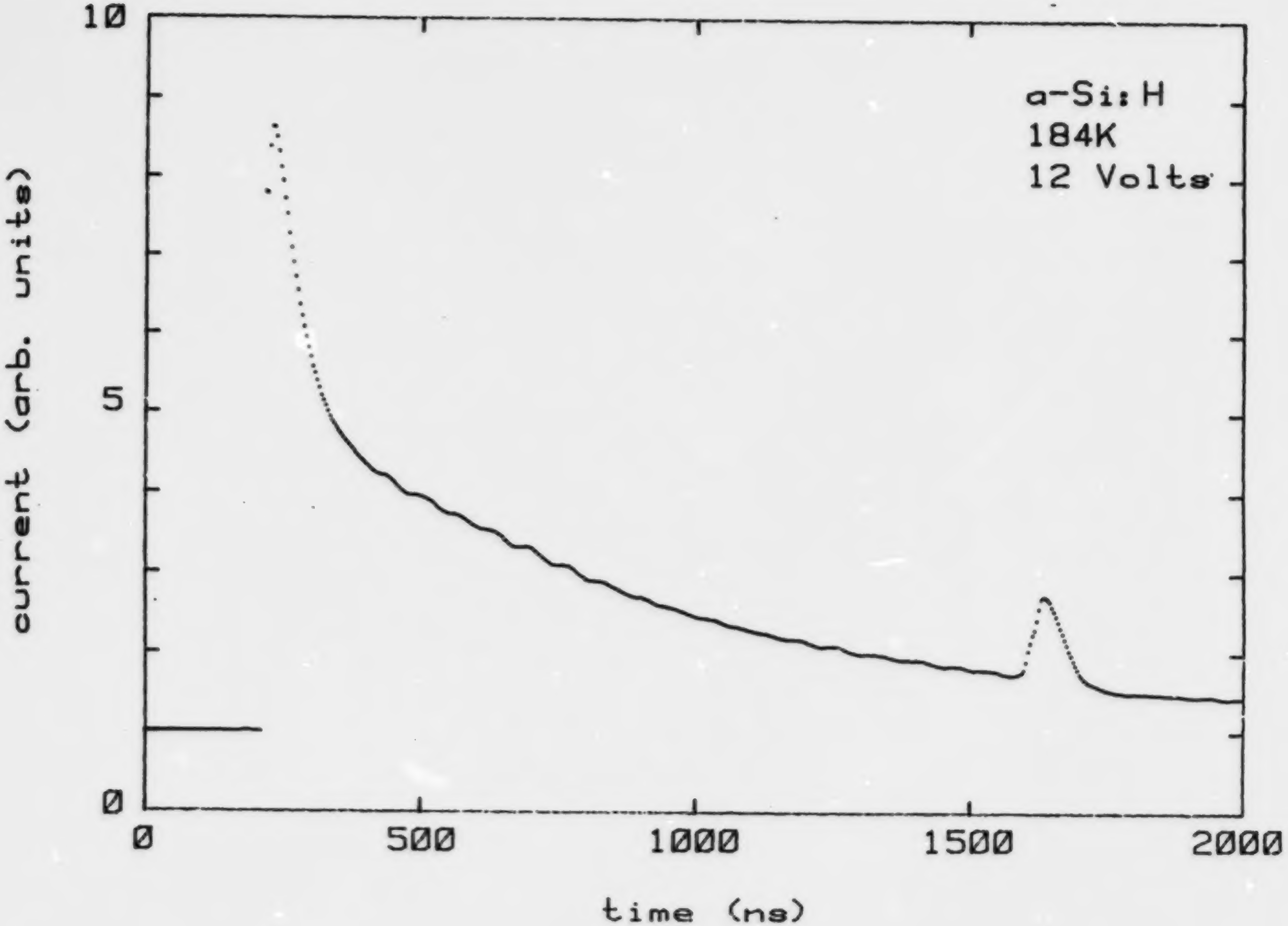

Figure 3 Low temperature time-of-flight current transient.

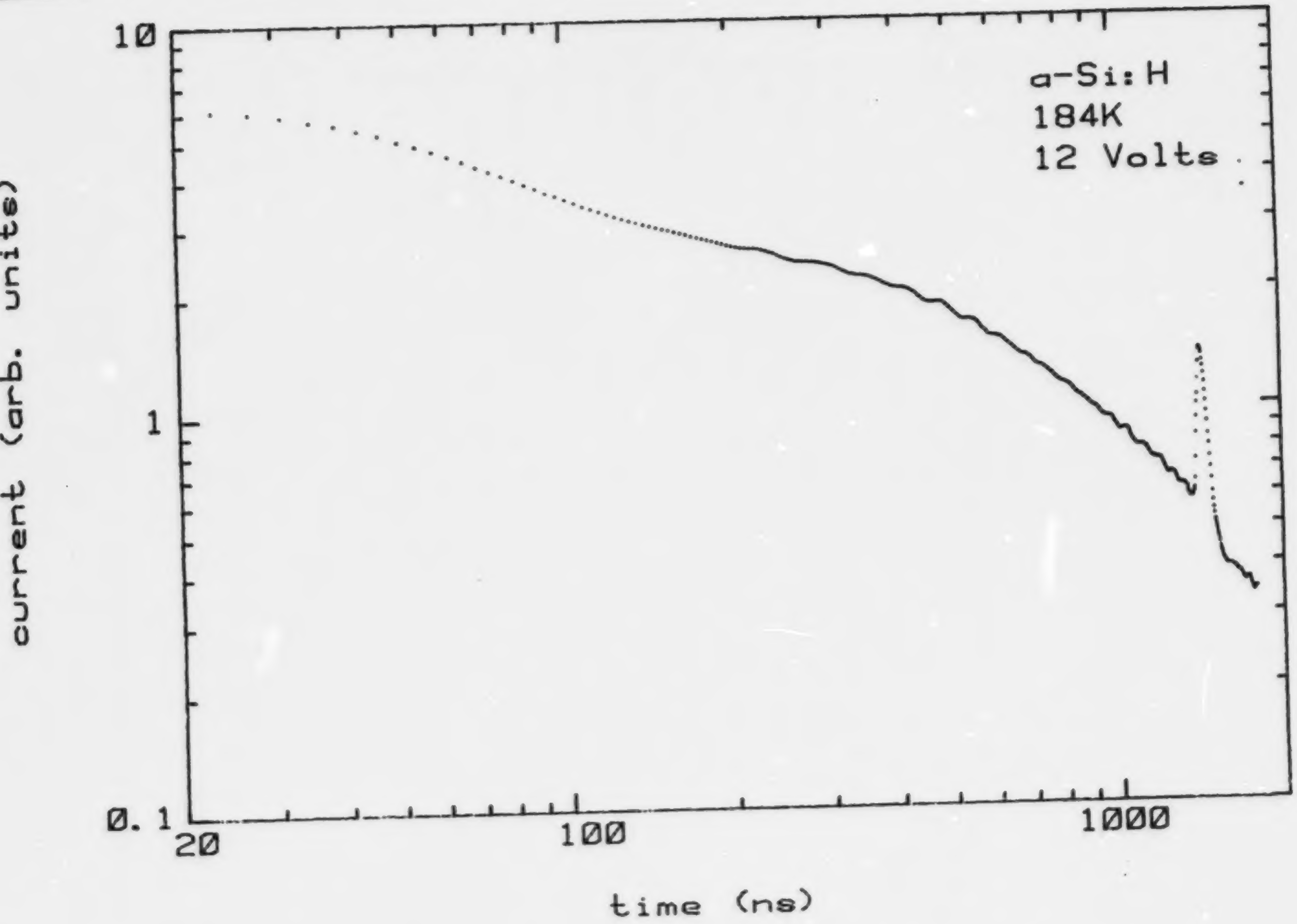

Figure 4 Log-log plot of figure 3.

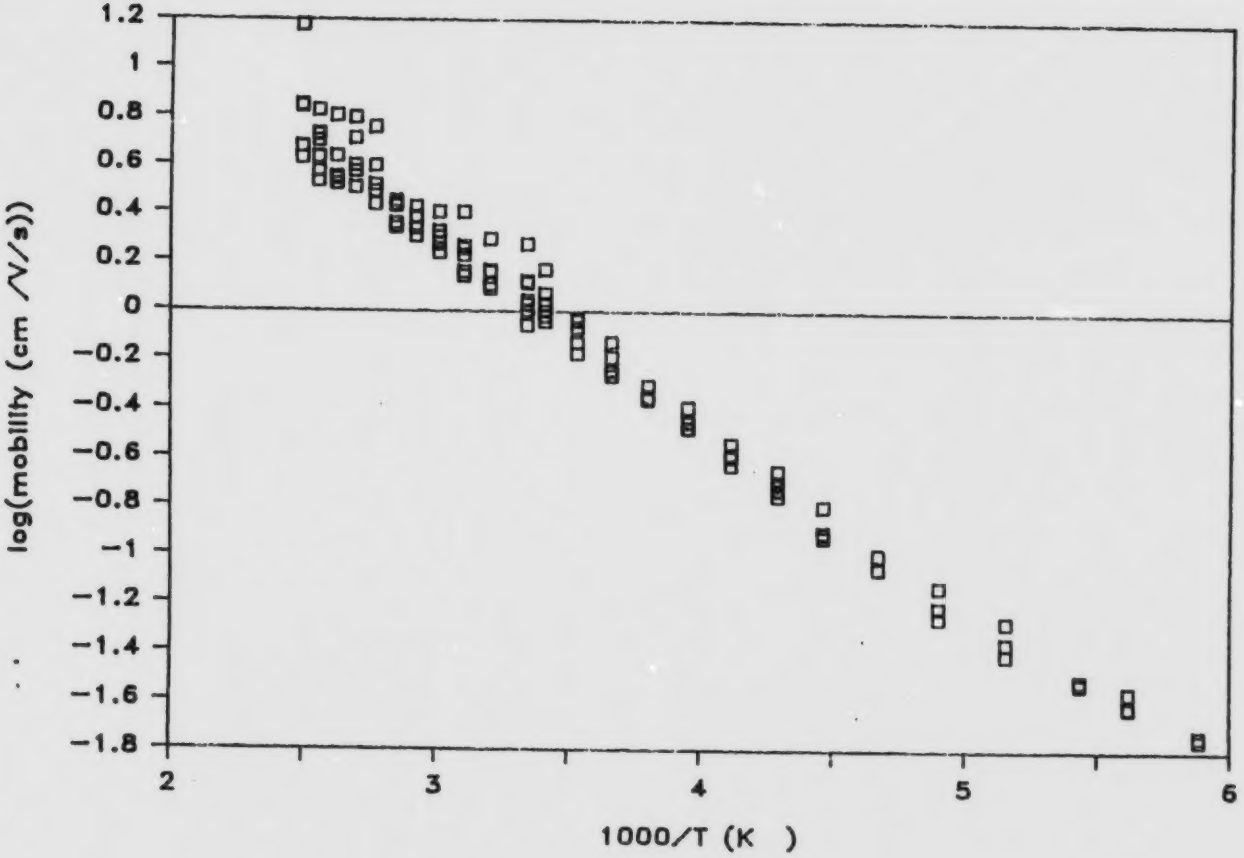

Figure 5 Arrhenius plot of mobility vs temperture.

as a function of temperature. An activation energy of 0.16 eV was obtained for this high quality intrinsic sample, over a wide temperature range, with a trend to a smaller activation energy at low temperature. Different values of the mobility at a given temperature were obtained for different applied fields. These results are essentially the same as those for the best intrinsic material produced by Xerox.

2.2.5 FRA: Frequency response analysis

Using a frequency response analyser, we have measured the real and imaginary parts of the capacitance of two structures over the range of 10^{-3} Hz to 10^{3} Hz and for temperatures ranging from 220K to 350K. The spectra obtained are shown in Figures 6 and 7 for Cr/a-Si:H/Cr and n^{+}/Sb structures, respectively. Activation energies have been derived by constructing a master curve for the individual spectra and noting the relative displacement of each curve with respect to the result at 303K. This is known as the Superposition Principle. The Arrhenius plot for the Cr-Cr structure gives an activation energy for a barrier process of 0.9 eV and for a bulk process of 0.88 eV. The bulk and barrier processes are identified by their frequency signature and the near equality of activation energies is almost certainly accidental. The n^{+} Sb sample, on the other hand, shows a barrier process activation energy of only 0.17 eV and bulk process activation energies of 0.44 and 0.2 eV.

While there is no immediate explanation of these results, it is worth noting that this technique can be used to study structures and can in principle give information on processes occuring at interfaces; it may be very well suited to the analysis of solar cell structures. It is also worth noting that this marks the first application of FRA to amorphous silicon.

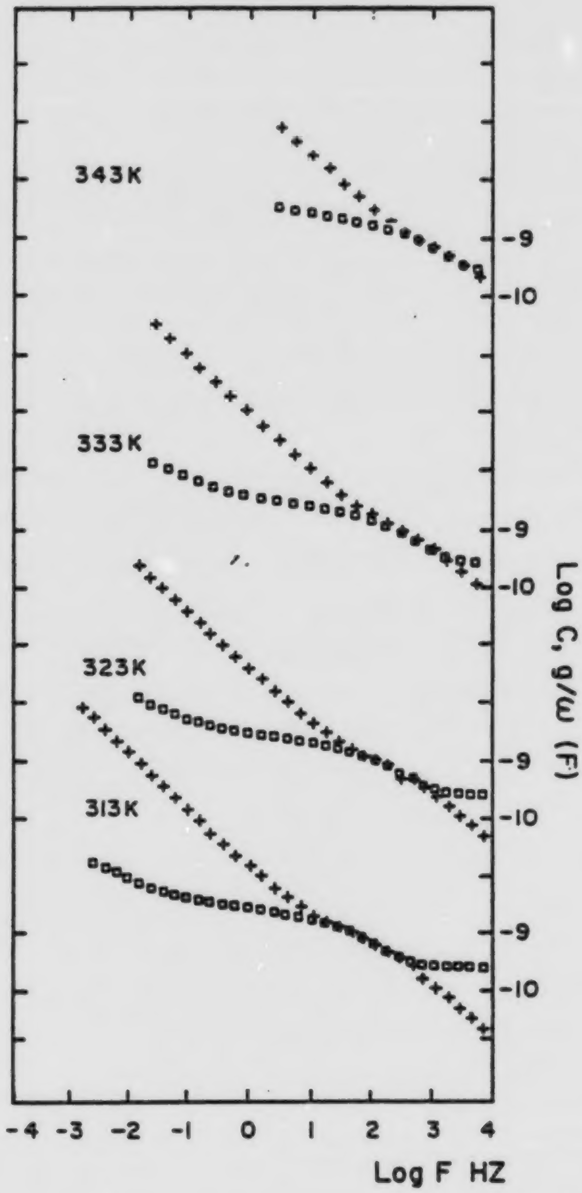

Figure 6 Capacitance (■) and conductance (+) of a Cr-a-Si:H sample over the temperature range 313K to 343K.

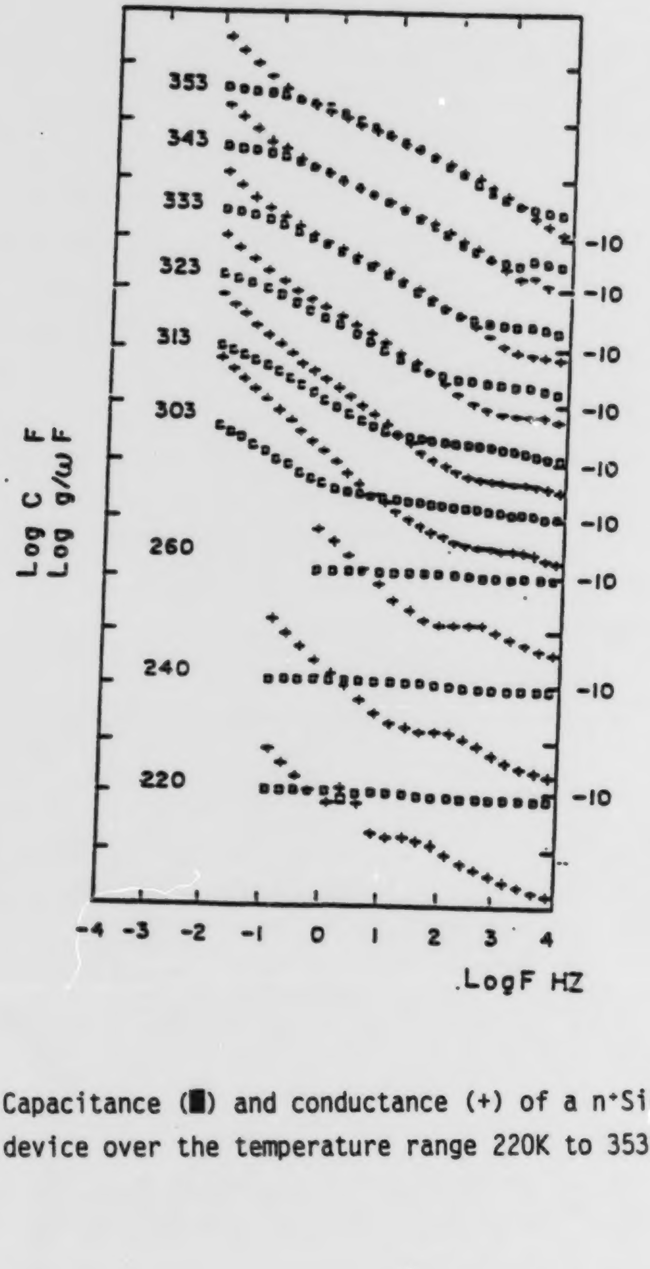

Figure 7 Capacitance (■) and conductance (+) of a n^+Si-a-Si:H-Sb device over the temperature range 220K to 353K.

3. DUAL-MODE FREQUENCY DEPOSITION OF a-Si:H FILMS

3.1 Deposition

Hydrogenated amorphous silicon (a-Si:H) has been one of the most actively studied materials during the last two decades. Films of a-Si:H are efficiently obtained by decomposition of silane SiH_4 (or disilane, Si_2H_6, in some cases) in a low temperature non-equilibrium plasma (low pressure electrical discharge), and the achievements in this field have been well reviewed [1-3]. Nevertheless, many questions are still open from both the technological point of view as well was in the basic understanding. Particularly, the recent trends in macroelectronics (the fabrication of devices for photovoltaic energy conversion, flat panel displays, and xerographic applications) demand large area deposition (>100 cm^2) at sufficiently high rates to satisfy the economical requirements. Also, the design of plasma deposition systems is oriented towards high gas conversion efficiency, to minimize waste of the expensive silane feed.

On the other hand, the electronic properties of a-Si:H structures are experimentally and theoretically quite well understood, and related to the residual hydrogen concentration (linked with the defect density) in the films and the film microstructure. Particularly the crucial role of hydrogen (usually 4-40 atomic percent) and microstructural features have been the subjects of numerous recent research studies, since they strongly depend on the discharge variables. Therefore, studies of processes in the plasma region and at the plasma-surface interface, where the films are actually growing, have been the focus of many investigations.

In usual cases, dc or rf discharges are used for the deposition of a-Si:H films, and different reactor configurations, most often parallel plate electrodes but also tubular systems, have been used [4]. High quality films are deposited from pure silane or its mixture with a diluting gas (most often Ar), at a total pressure of several hundreds of millitorrs, and at substrate temperatures ranging typically from 200 to 350°C. The deposition rates are usually between 1 and 5 Å/s in the above mentioned discharges, depending on whether the films are grown on the "anode" or "cathode" surface [5].

The deposition is believed to proceed predominantly via electron impact decomposition of the parent SiH_4 molecule, forming SiH_x ($x = 0$ to 3) radicals which become the potential precursors of the film growth. The primary reaction products and corresponding enthalpies [5] are as follow:

$$SiH_4 \rightarrow SiH_2 + H_2 \qquad (\Delta H = 2.2\ ev) \qquad (1)$$
$$SiH_4 \rightarrow SiH_3 + H \qquad (\Delta H = 4.0\ ev) \qquad (2)$$
$$SiH_4 \rightarrow Si + 2H_2 \qquad (\Delta H = 4.4\ ev) \qquad (3)$$
$$SiH_4 \rightarrow SiH + H_2 + H \qquad (\Delta H = 5.9\ ev) \qquad (4)$$

The subsequent growth process proceeds via diffusion of the radicals towards the substrate surface, where they are adsorbed and incorporated into the growing layer. Since the inelastic interactions of electrons with the gas molecules are most intensive at the end of the cathode fall (for dc discharges), or the plasma sheath (for rf discharges), the probability for the radicals to diffuse to the cathode is higher than to the anode, which has been put forward to explain the observed differences in the respective growth rates [5].

Microwave (MW) plasma deposition, instead of lower frequency excitation, has been shown to yield at least an order-of-magnitude higher deposition rates, as demonstrated for a-Si:H, organosilicone, silicon oxide and silicon nitride films [6]. This is attributed to higher concentrations of precursors in the gas phase, due to differences in the electron energy distribution functions, EEDF [7]. However, a-Si:H films deposited in a large volume microwave plasma (LMP^R) apparatus [8] displayed poor quality because of dominant columnar morphology and consequent post-deposition reactions with atmospheric constituents to give insulating a-Si:(H,C,O) alloys.

Recently, we have concentrated on the use of a "dual frequency mode" plasma, in which differing amounts of radio frequency (13.56 MHz) power were applied to the substrates, while sustaining the plasma with constant microwave (2.45 GHZ) power [8]. Results for deposition of silicon oxide and organosilicon films have manifested important effects of the rf-induced negative dc self-bias voltage on the deposition rate, film composition and dielectric properties. This new technique has been proposed for producing "tailored" films, while preserving the advantages of high deposition rates and low substrate temperatures.

The aim of this study, based on the above-mentioned objectives, has been to deposit high quality a-Si:H films at high deposition rates (several tens of Å/s) over large areas (>100 cm^2). At the same time, the film microstructure and composition should be favorably affected by applying different substrate biases to control the surface bombardment and consequently the plasma-surface interactions, leading to the desired high quality a-Si:H deposits.

The a-Si:H films were prepared in a high vacuum system schematically illustrated in Figure 8. The deposition chamber consisted of the upper stainless-steel plate containing lead-throughs, a cylindrical pyrex vessel 280 mm in diameter, and a quartz bottom

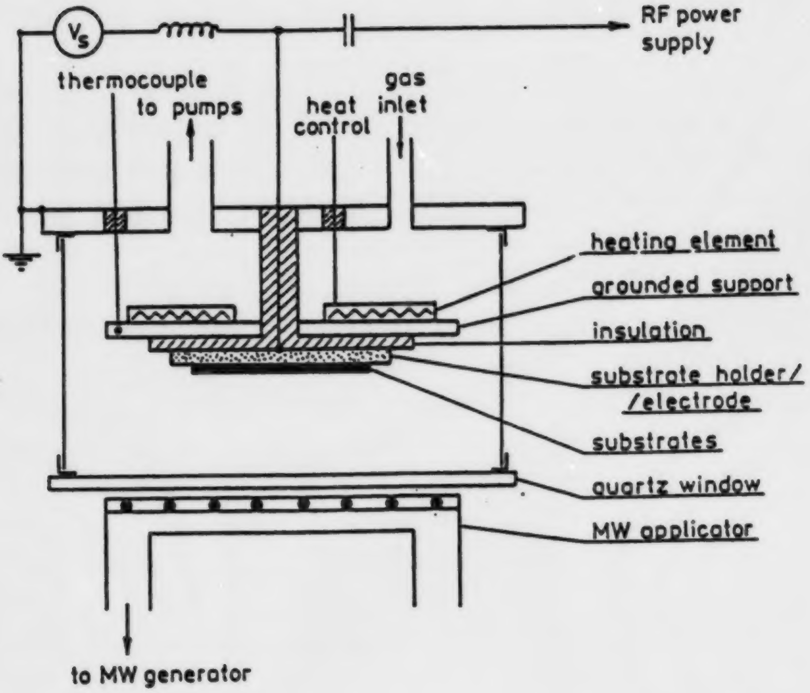
V_s
RF power supply
thermocouple
to pumps
heat control
gas inlet
heating element
grounded support
insulation
substrate holder/
/electrode
substrates
quartz window
MW applicator
to MW generator

Figure 8 Schematic arrangement of the deposition system for "dual-frequency-mode" grown a-Si:H films.

window for microwave power application; it was evacuated by combined turbomolecular and rotary pumps. The chamber interior comprised a grounded copper support plate with a heating element. This support was electrically insulated from the substrate holder/electrode (150 mm in diameter) using polyimide (Kapton^R) foils or mica. This electrode was connected to an RF (13.56 MHz) power supply via a blocking capacitor and a matching network. The substrate holder's surface temperature was calibrated using a thermocouple attached to the rear of the copper support. MW power was introduced from a slow wave structure, connected via rectangular waveguides to a 2.45 GHz, 2kW power supply.

The parameters controlled during the deposition process were (1) the MW power P_{MW}; (2) P_{RF} [and corresponding self-developed negative dc bias potential, called the substrate bias V_s]; (3) the feed gas flow rate Q of silane or its mixture with argon; (4) the substrate temperature T_s; (5) the total working gas pressure p, and (6) the deposition duration t. After initial optimization experiments, the following parameters were kept constant throughout:

P_{MW} = 150 W
Q_{SiH_4} = 8 sccm
T_S = 270°C
p = 100 mTorr

The a-Si:H films were deposited onto undoped crystalline silicon wafers (5.1 cm in diameter) and glass slides with pre-evaporated chromium electrodes. The d.c. electrical conductivity was determined by measuring the current I using a planar electrode arrangement with an interelectrode distance of 1 mm, in ambient atmosphere, applying different voltages of 10, 20 and 50 V. The photoconductivity ratio is $R = I_{ph}/I_d$, where I_d is the dark current while I_{ph} is the current measured under AM 1.5 (~100 mWcm^{-2}) sample illumination, using an Oriel Model 81100 solar simulator. Film thicknesses d were measured by the stylus method, using a Sloan-Dektak instrument.

In a first series of experiments, we concentrated on the growth of a-Si:H films from a SiH_4/Ar mixture; the results of deposition rate r_D and photoconductivity ratio R measurements are illustrated in Table 1 and Figure 9. The deposition rate in a pure MW discharge can attain 20 Å/s, but R remains relatively low (-1000). When a small amount of RF power is applied simultaneously, the deposition rate is seen to drop substantially (to about 6 Å/s) accompanied by an increase in R (10 000 to 70 000). Experiments were conducted also by applying only RF power; whereas the resulting films exhibited fairly high R values, r_D remained small, about 2-3 Å/s. Subsequently, the first attempts were made to use undiluted SiH_4 as the feed gas; these resulted in a substantial increase in the deposition rate (33 Å/s for pure MW discharge and above 20 Å/s for the combined dual-frequency discharge). The accompanying increase in R (see Table 2 and Figure 9) was also very promising.

Table 1 SiH_4/Ar (42 sccm) Mixtures

T_s	Power (w)		Deposition Rate D (Å/s)	$R = \sigma_{ph}/\sigma_d$
	RF	MW		
280	0	120	20	10^3
280	120	0	1.5	2.0×10^4
280	125	0	1.0	1.5×10^4
250	3	120	5.0	1.8×10^4
250	5	120	5.0	1.8×10^4
250	5	120	5.0	2.5×10^4
250	10	120	5.5	3.6×10^4
250	10	120	5.5	7.0×10^4

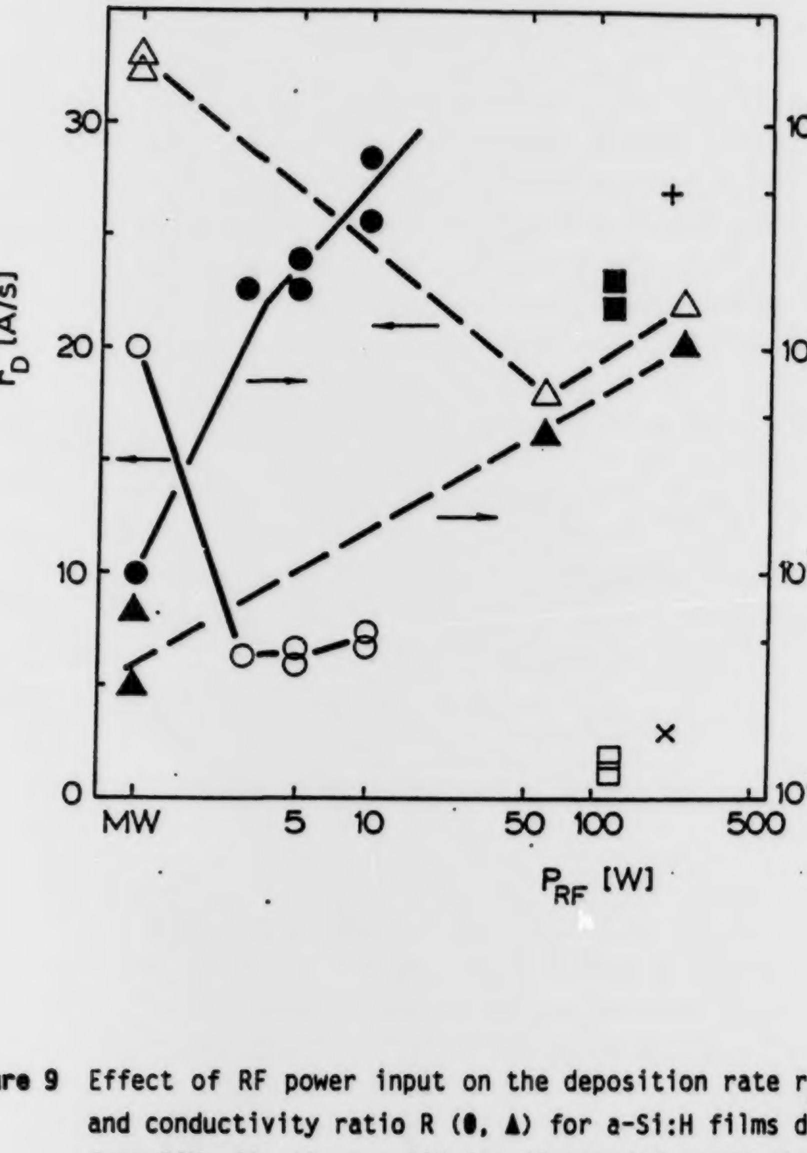

Figure 9 Effect of RF power input on the deposition rate r_D (○, Δ) and conductivity ratio R (●, ▲) for a-Si:H films deposited from SiH_4 (Δ, ▲) or a SiH_4/Ar (8 sccm/42 sccm) mixture (○, ●). The values for r_D (■, x) and R (■, +) for films deposited in "pure" RF discharge in SiH_4 (+, x) and SiH_4/Ar mixture (□, ■) are also shown.

Table 2 Pure SiH_4

power MW [W]	power RF [W]	Bias V_s [V]	Deposition rate r_D	Ration $R = \frac{\sigma_{ph}}{\sigma_d}$
150	-	-	33	300
150	-	-	33	700
-	210	150	3	50 000
150	60	55	18	4 000
150	170	150	15	400
150	170	168	20	1 000
150	250	185	20	16 000

All further depositions were performed in pure silane. The effect of negative substrate bias voltage V_s (the result of increasing RF power input, ranging from 0 to 200 W) on r_D and R is shown in Figure 10. According to the behavior of the r_D (V_s) dependence, three different regimes of V_s

A) Pure MW discharge (V_s = 0), resulting in high r_D of 33 Å/s, but in relatively low R (around 1 000).

B) When low V_s values are applied (0 to -300 V), these result first in a sharp drop in r_D (18 Å/s), followed by a slight increase up to 22 Å/s at V_s = -300 V. In this regime, R increases to values ranging between 10 000 and 50 000.

C) For V_s values exceeding -300 V, r_D again decreases slightly, while R appears to remain constant.

Optimum conditions for the deposition of a-Si:H films by dual-mode-frequency discharge occur at the boundary between regimes B and C, where both the highest r_D (22 Å/s) and R (50 000) values are encountered, under discharge conditions defined by p, Q, P_{MW} and T_s values noted above.

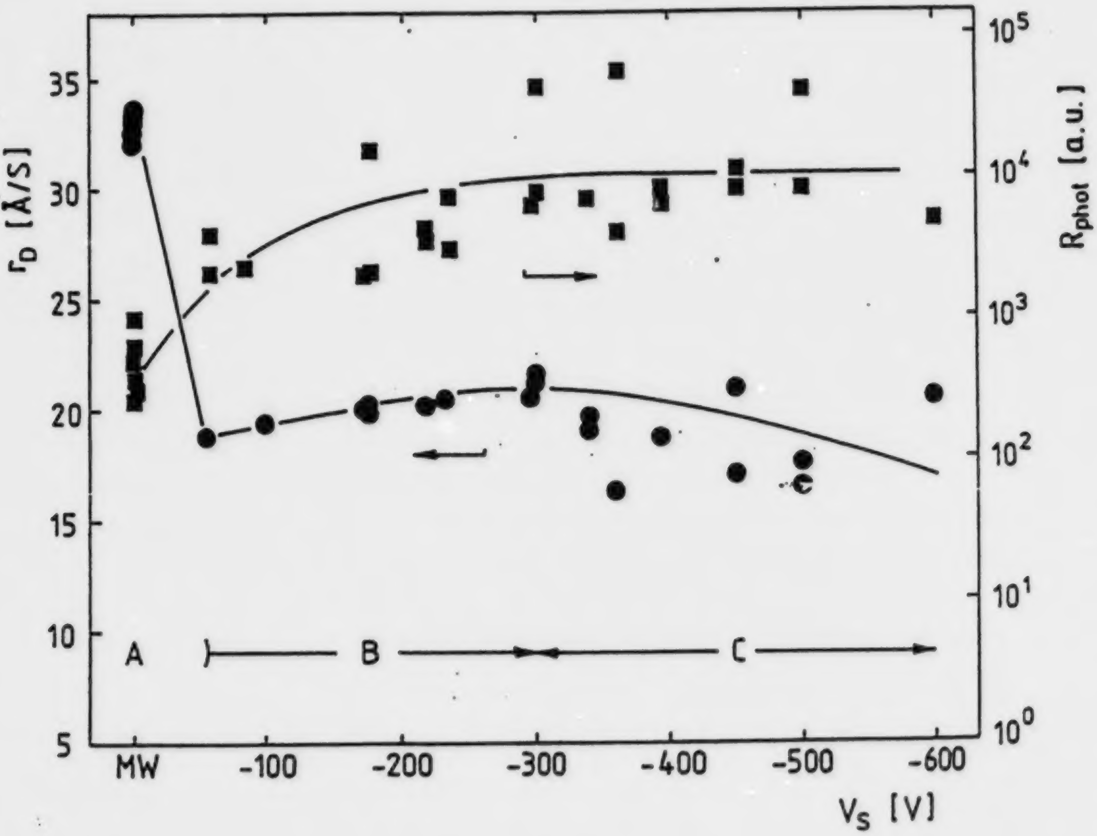

Figure 10 Effect of the negative substrate bias voltage on the deposition rate and photoconductivity ratio for "dual-frequency" deposited a-Si:H films.

It is useful to discuss the above described results in terms of a mechanistic model involving the following three steps:

i) initiation, or creation of reactive precursors;
ii) propagation, or reactions between precursors;
iii) termination of reactions to produce the final solid reaction product.

The rate and location of these steps in the reactor can be affected separately by changes in plasma parameters, and they are influenced in different ways in MW and RF discharges.

The results in regime A ($V_s = 0$) are typical for MW discharges, where the efficiency of radical formation is higher than in lower frequency discharges, leading to the observed high deposition rate. On the other hand, these radicals diffuse towards the substrate surface, forming a relatively porous, columnar film structure with a high density of defects in composition and in microstructure. This is reflected by the low R values in regime A.

By superimposing relatively low values of V_s (regime B), the interactions of charged species (positive ions) with the surfaces begin to play an important role, a phenomenon which is typical for lower frequency discharges [9]. This affects the propagation step (ii) because the low energy ion bombardment reduces the adsorption rate of film-forming precursors, causing the observed drop in r_d. The increase in V_s is brought about by higher RF input power, causing the observed rise of r_D in regime B. Low energy ions can favor retention of certain precursors over others because of their different sticking probabilities, so that different ratios of the SiH_x (x = 0 to 3) radicals in the films can be expected.

Ionic surface bombardment during film growth also affects surface migration of precursors before the reactions are terminated. This generally results in smoother, featureless films, in agreement with the modified structure zone model of Messier et al. [10] and with our own previous observations [8]: the enhanced surface mobility causes a reduction in nucleation and growth of columnar features leading to the more densely packed and chemically more stable structures. The selection of SiH_x radicals and the denser microstructure are believed to be responsible for the observed increase in R in regime B. Still more energetic ion bombardment in regime C (V_s > -300 V) further decreases the net adsorption rate of the growth precursors, due to physical sputtering; hence, the drop in r_D. However, the film composition and microstructure seem to be almost unaffected, as suggested by the constant R values in Figure 10.

Detailed confirmation of the mechanistic growth model above requires in-depth analysis of the films by infrared spectroscopy, scanning microscopy, and other techniques sensitive to the effects of composition and morphology on a-Si:H film properties.

3.2 Infrared Characterisation

The conditions for the deposition of mixed MW/RF a-Si:H were discussed in the previous section. As was noted there, the photoconductivity/dark conductivity ratio (σ_{ph}/σ_d = R) was used as a criterion of acceptability. This ratio, R, is normally in the range of

50 000 for RF-deposited material and more than an order of magnitude lower for MW-deposited material. Mixed MW/RF deposition not only raises R to the 20 000 range but has the distinct further advantage of increasing the film deposition rate to about 20 A/s, an order of magnitude higher than that obtained with RF. The use of mixed MW/RF deposition is, thus, an attempt to glean the benefits of both types of deposition.

The ratio, R, is, however, only a first criterion and it is necessary to further characterize this material. This report is concerned with the IR characterization. Before discussing it, something should be said of this mixed frequency deposition and just how it differs from the separate types of deposition. Radio frequency deposition, at 450 KHz, takes place in a capacitive discharge, using either the self-bias of the system (at some -50 V) or an additional positive bias of the substrate, to overcomme the negative self-bias. This has the effect of varying the energy, as well as the sign, of the charged species which deposit.

Microwave frequency deposition uses a slow wave guide [12] at 2.45 GHz, with its field directed parallel to the sample, which lies coplanar to the guide. The species which deposit are then controlled only by drift, their impact energies significantly lowered. Their enhanced deposition rate comes from the fact that more of the reactant gas is converted to free radicals and ions at this higher frequency.

In the mixed frequency case, with the electrode biased by a 13.56 MHz RF component, there is an alternating low frequency bias perpendicular to the sample, which causes deposition at enhanced energies and clearly leads to simultaneous sputtering of the deposited material.

The MW-deposited material has consistently been found to have poor photovoltaic properties, as witness its R values near 1000. The enhanced R value of the mixed frequency deposition must then be due to the effect and direction of the RF field. The sputtering certainly causes physical compaction and, probably, preferential sputtering. Because this mixed frequency deposition is fundamentally different from either RF or MW deposition, alone, it may well be that the criteria used to judge the photovoltaic characteristics of this material may be substantially different. One of these is structure, where it is generally felt that the better photovoltaic materials have a concentration ratio of Si-H/Si-H$_2$ > 1 and no Si-H$_3$. As will be seen, mixed frequency deposition also results in an absence of Si-H$_3$ but the Si-H/Si-H$_2$ ratio is invariably < 1.

The samples were deposited under the constant conditions given in the previous report, with the RF bias ranging from 0 to 600 V. Thickness was measured by profilometer ($t_{profile}$) and calculated from the IR fringing (t_{IR}). The profilometer measurements invariably disagreed with the IR data in a random manner, as seen in Table 3.

Table 3 Spectroscopic Data for Mixed Frequency-Deposited a-Si:H

Bias	$t_{profile}$ (μm)	$t_{profile}/t_{IR}$	Si-H/Si-H$_2$	Percent Si-H$_n$(b)
0	1.5	1.33	0(a)	2
0	1.6	1.69	0.48	3
100	0.55	0.81	0.90	9
175	1.2	1.14	0.62	14
300	0.70	0.83	0.87	9
360	0.30	0.35	0.84	22
500	0.52	0.68	0.80	15
600	0.58	0.63	0.42	17

(a) No Si-H detected.

(b) Estimated from data in reference 15.

IR spectra were obtained on a BOMEM DA3 FTIR spectrometer. An example, showing the mild fringes from which the thickness was calculated, is seen in Figure 11 and the Si-H_n stretching region, near 2 000 cm^{-1}, is seen in Figure 12 for a sample deposited at a bias of 500 V. Unfortunately, the programs available on the FTIR are not applicable to peak deconvolution. Thus, in order to separate and study the component peaks, it was necessary to transfer the data from the BOMEM to a personal computer and to carry out the deconvolution with the MATLAB programs available there.

This was done by using an available program on the BOMEM's PDP11 to transform the spectrum into text format. The BOMEM was then cable-connected to the PC and the data transfer was made using the public domain KERMIT programs. Finally, a program was written to transform the newly arrived data into the format the MATLAB programs can handle. The IR spectrum in the Si-H_n stretching region was then deconvoluted, as seen in Figure 13.

The deconvolution was performed using Gaussian peaks having full widths at half maxima of 130 cm^{-1}. One peak, representing Si-H, was placed at 2 000 cm^{-1} and a composite of peaks at 2 055 and 2 080 cm^{-1} was used to represent Si-H_2; this composite is based on our previous IR deconvolution studies [13-14]. The Si-H/Si-H_2 ratios are found in Table 3, along with concentrations using estimates based on the IR data of Brodsky and coworkers [15]. Note, however, that these workers made certain assumptions about peak heights, numbers and positions which have since been shown [13, 14, 16, 17] to be in error.

As is common in plasma deposition, even when every attempt has been made to control the deposition parameters, there is a certain amount of scatter in the data. Thus, the data discussed here in should be considered as representative of this scatter and not as indicative of any trends. Comparison of several sets of data, to be taken under similar circumstances, will be necessary for the observation of any trends.

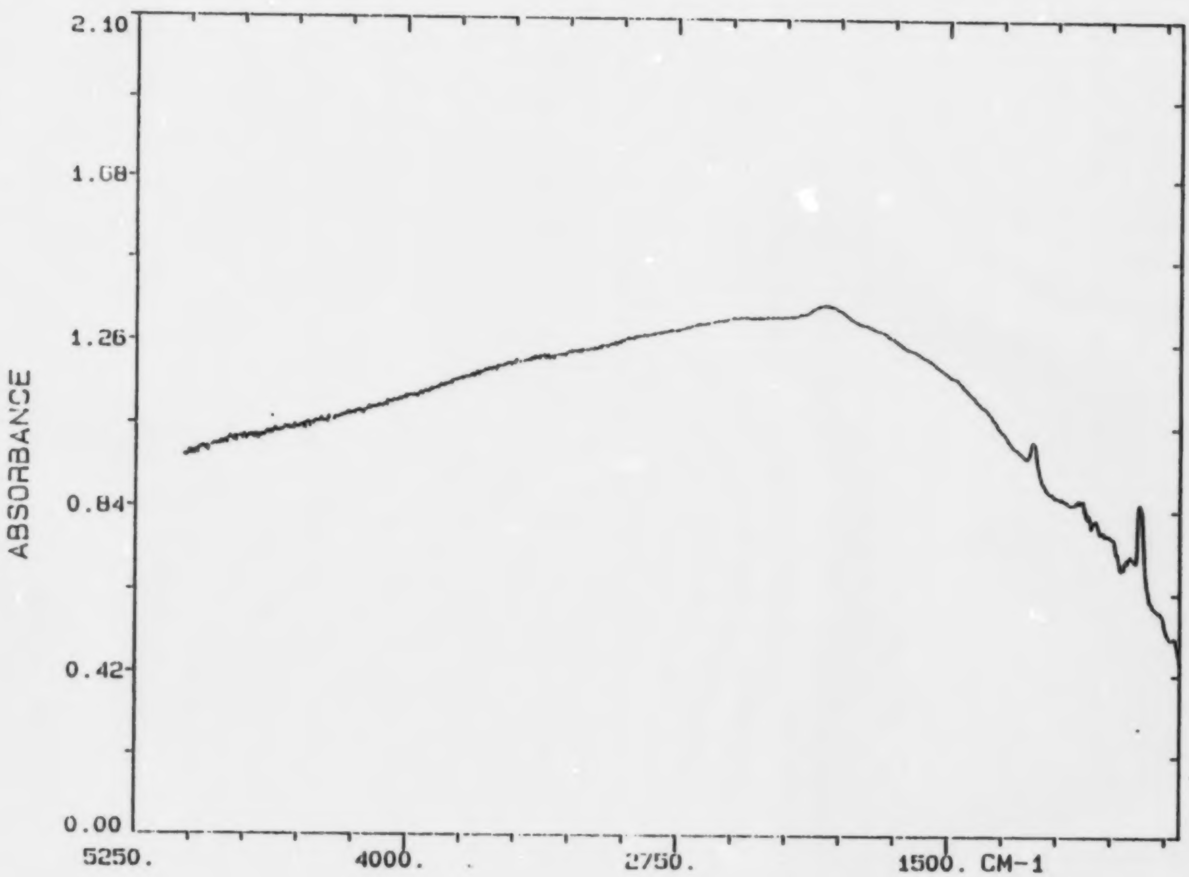

Figure 11 IR spectrum of a-Si:H deposited with a 500 V bias.

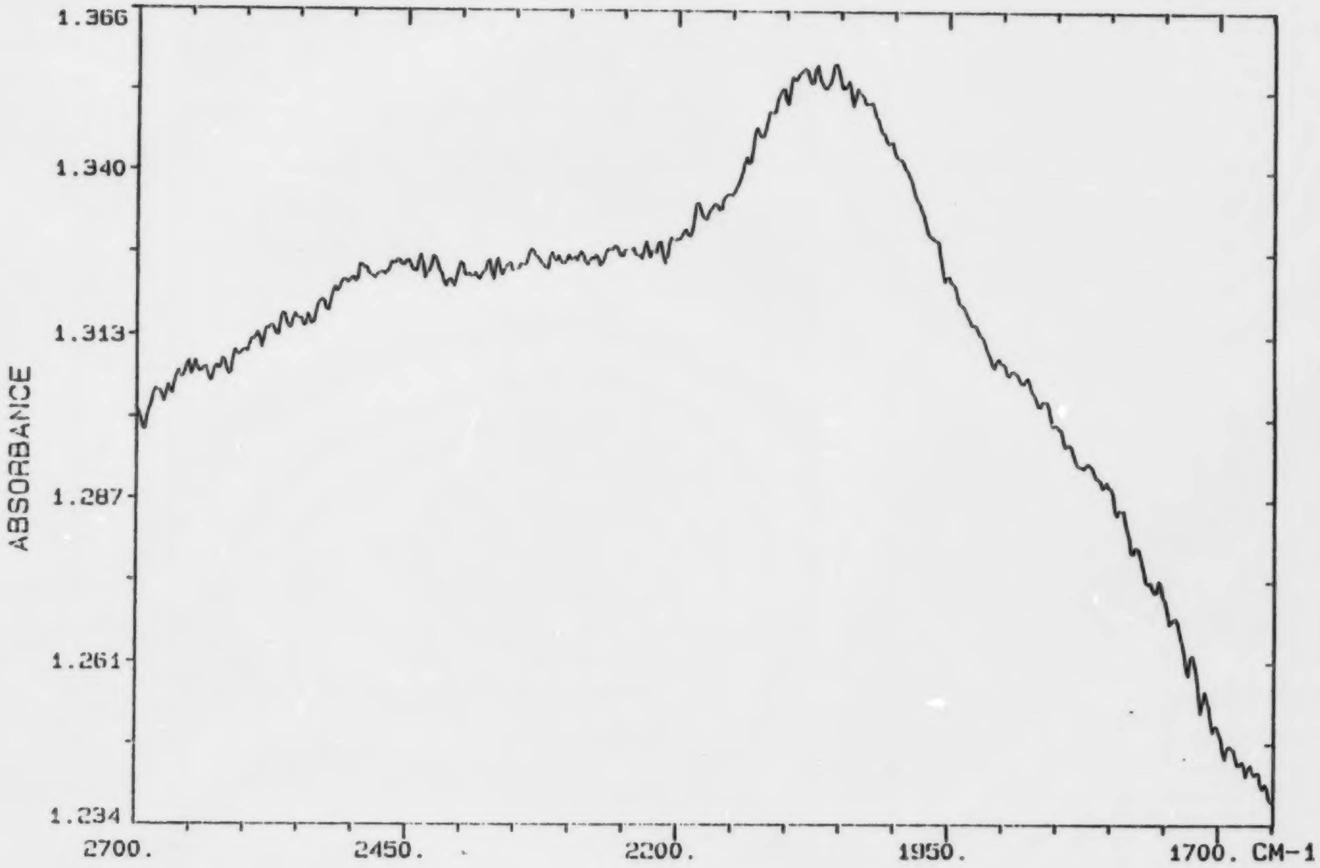

Figure 12 Same as figure 11, showing an enlargement of the $Si-H_n$ stretching region.

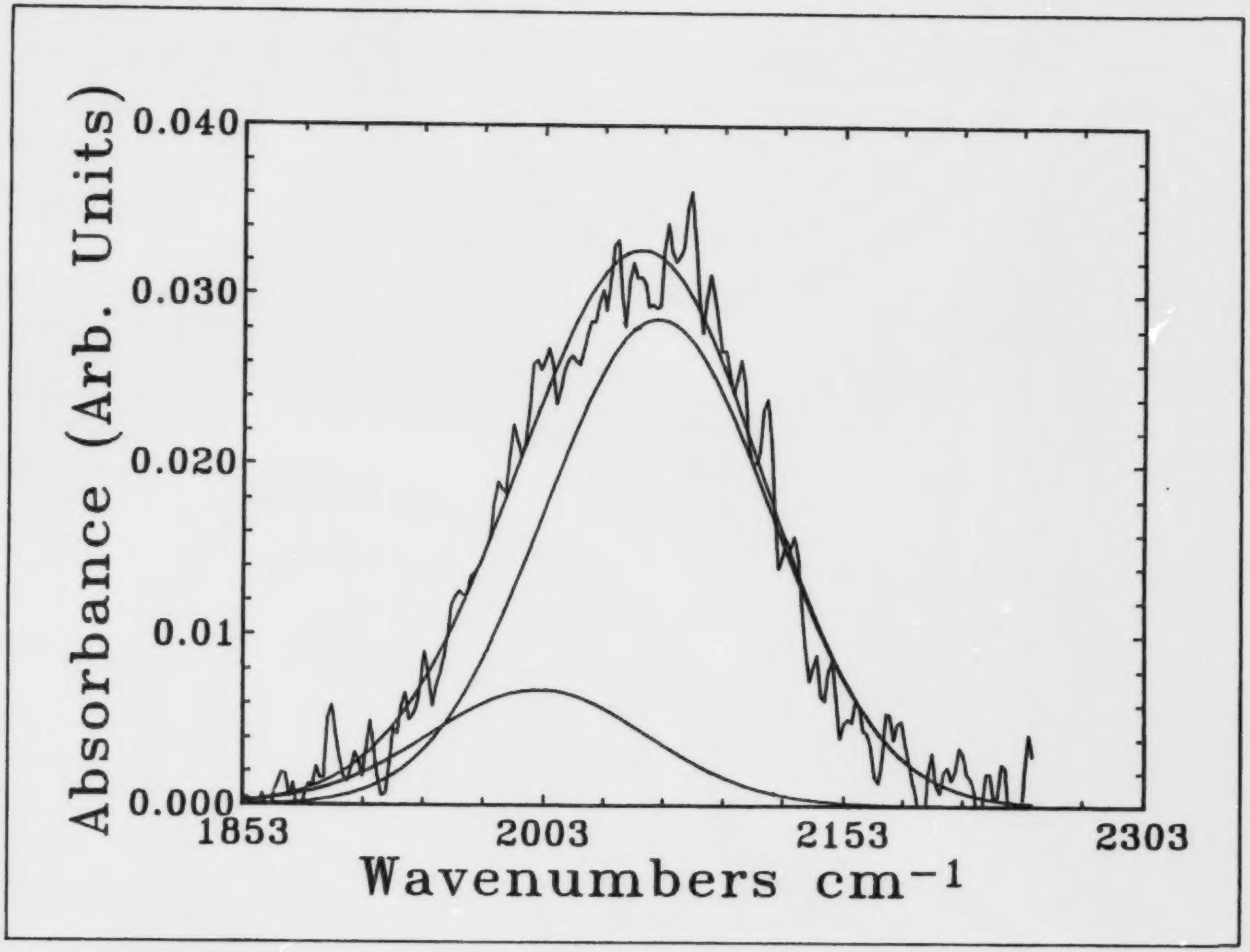

Figure 13 Same as figures 11 and 12. MATLAB deconvolution of the Si
SiH_n stretching region.

4. DOPING a-Si:H BY COSPUTTERING

4.1 Deposition

Instead of using toxic or explosive gaseous dopants, such as arsine and diborane, as is generally done, we have employed metallic dopants, which may be obtained by evaporating or sputtering into the silane plasma. This has potential cost advantages over the conventional method.

In our earlier work, we found that both cosputtering and gas phase procedures led to electronic doping of the semiconductor. Most of our earlier work was on the simpler metal evaporation procedure. However, due to the difficulties in monitoring the evaporation rate, it was decided that we should concentrate on the more readily controllable sputtering procedure.

In the early phases of this work, we concentrated on the questions of the amount of doping and the efficiency of doping obtainable, including the optimum deposition conditions, and on the level of control and of reproducibility to be obtained using the sputtering process.

4.1.1 p-Type Doping

As p-doping is well known to be more difficult than n-doping, we began with it. We chose to concentrate on Al as the most promising element to provide p-doping by sputtering. In an initial series of measurements, we changed only the flow rate of SiH_4, assuming that this modifies the relative Al content in Al-Si layers. The rest of the deposition parameters were kept constant as follows:

- frequency: 100 KHz
- substrate temperature: 250°C
- total pressure: 100 mTr
- flow rate of Ar: 25 sccm
- bias voltage: 300 V
- power: 200 W
- deposition time: 5 h

After 5 hours of deposition, the sample thicknesses were 0.5 µm (14 Å/min).

The DC conductivity measured in the coplanar geometry is shown in Figure 14. It is seen that the conductivity increases dramatically for SiH_4 flow rates less than 0.50 sccm. The change covers 7 orders of magnitude between 3.10^{-11} $(\Omega\ cm)^{-1}$ for 3 sccm and 2.10^{-4} $(\Omega\ cm)^{-1}$ for 0.3 sccm of SIH_4. From Figure 14, it is seen that the aluminum is incorporated into a-Si:H, changing the conductivity. We can conclude, as well, that the compensation of undoped n-type a-Si:H is observable at high SiH_4 flow rates. Indeed, the conductivity increases for SiH_4 flow rates less than 2.50 sccm, the Si-Al layers become p-type. The order of the conductivity change is comparable with results obtained elsewhere [18]. We have also performed the photoconductivity measurements shown in Figure 15. There, one sees the quenching of the photoconductivity, which is of the same order as that in Ref. [20]. We have also measured the current-voltage characteristics vs temperature, to study the activation energy.

The Arrhenius plots of the current vs inverse temperature as in Figure 16 show two regions of different activation energies for a sample with 0.40 sccm silane flow. Figure 17 shows the high temperature activation energy values as a function of silane flow.

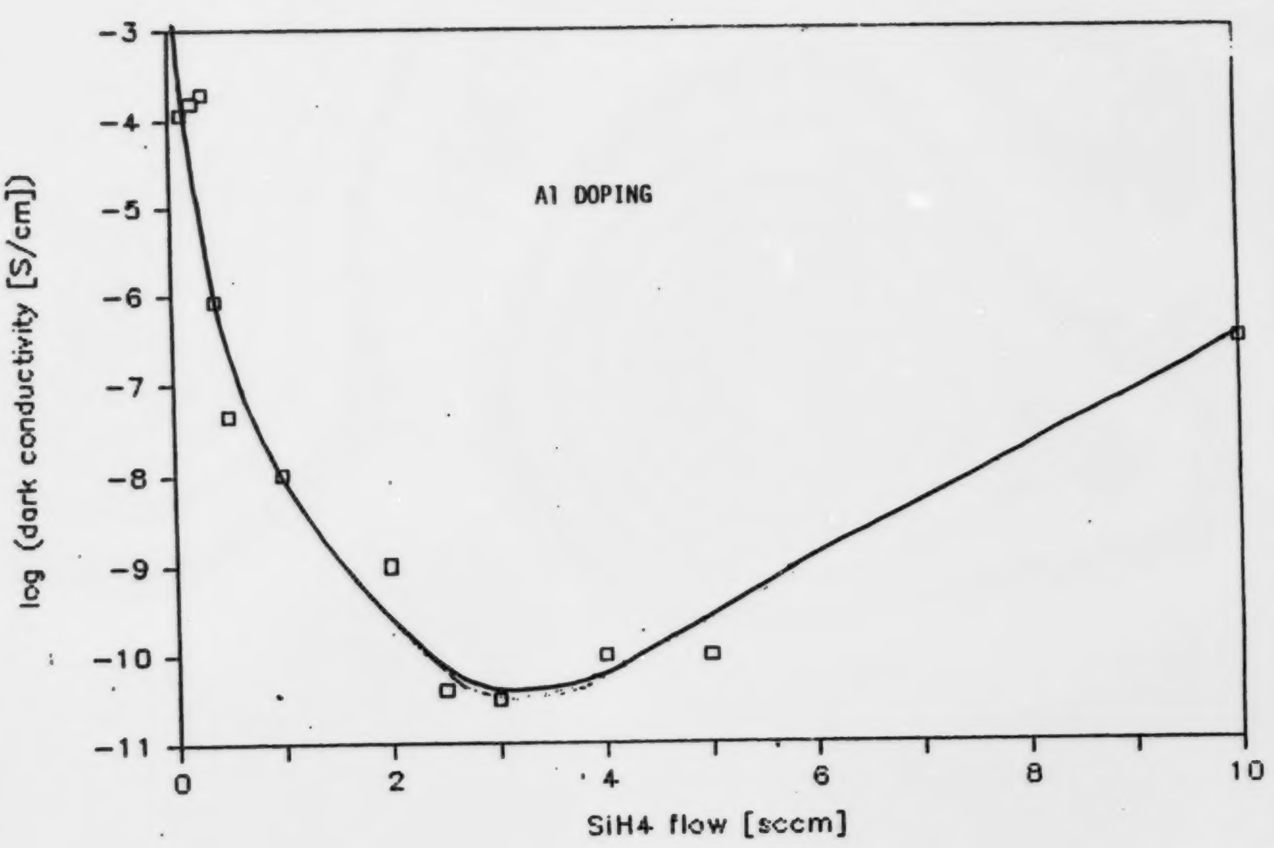

Figure 14 Coplanar Dark Conductivity vs Silane Mass flow in Glow Discharge.

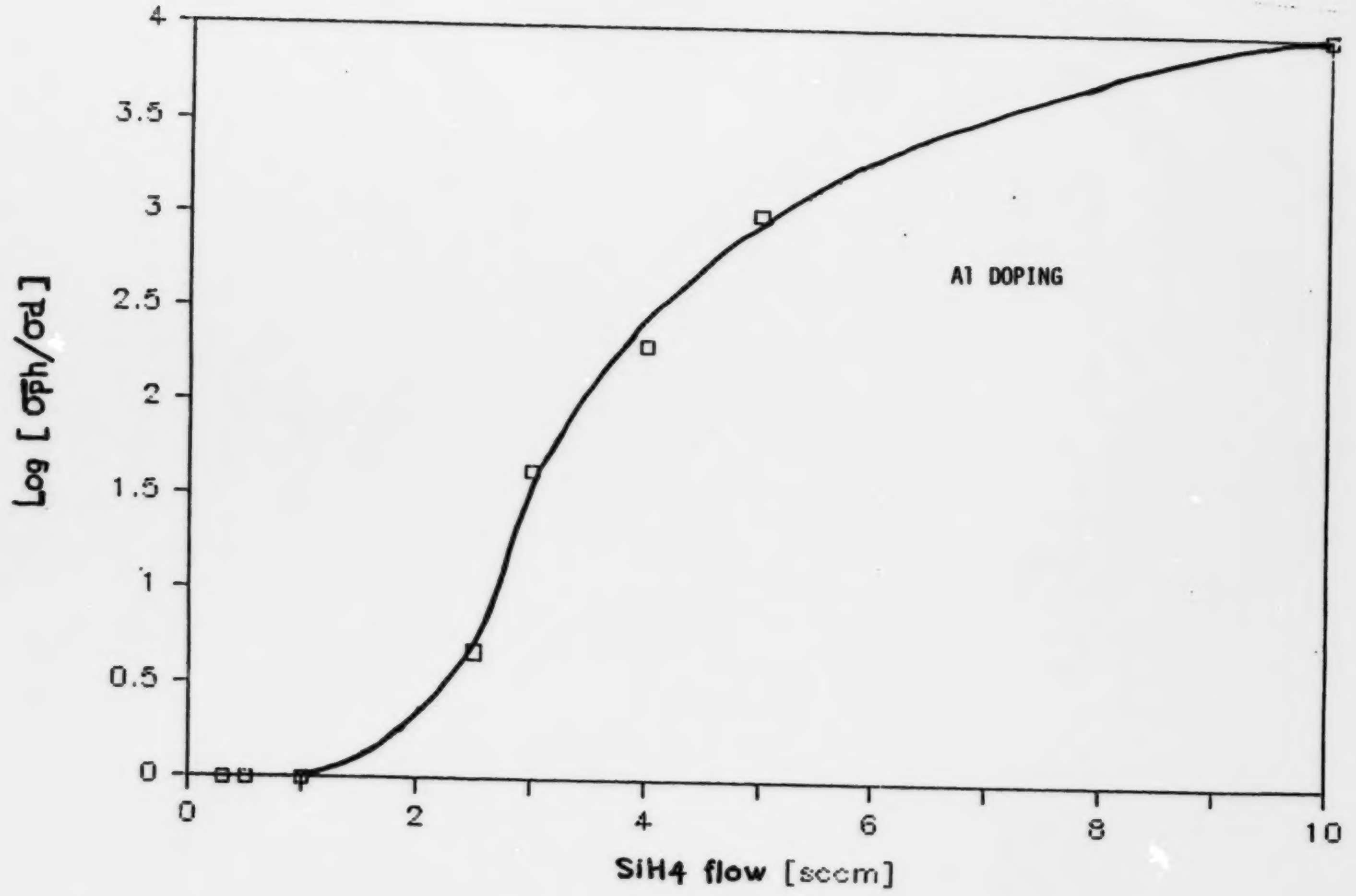

Figure 15 Ratio of the Planar Photoconductivity to Dark Conductivity vs Silane Mass flow in the Glow Discharge.

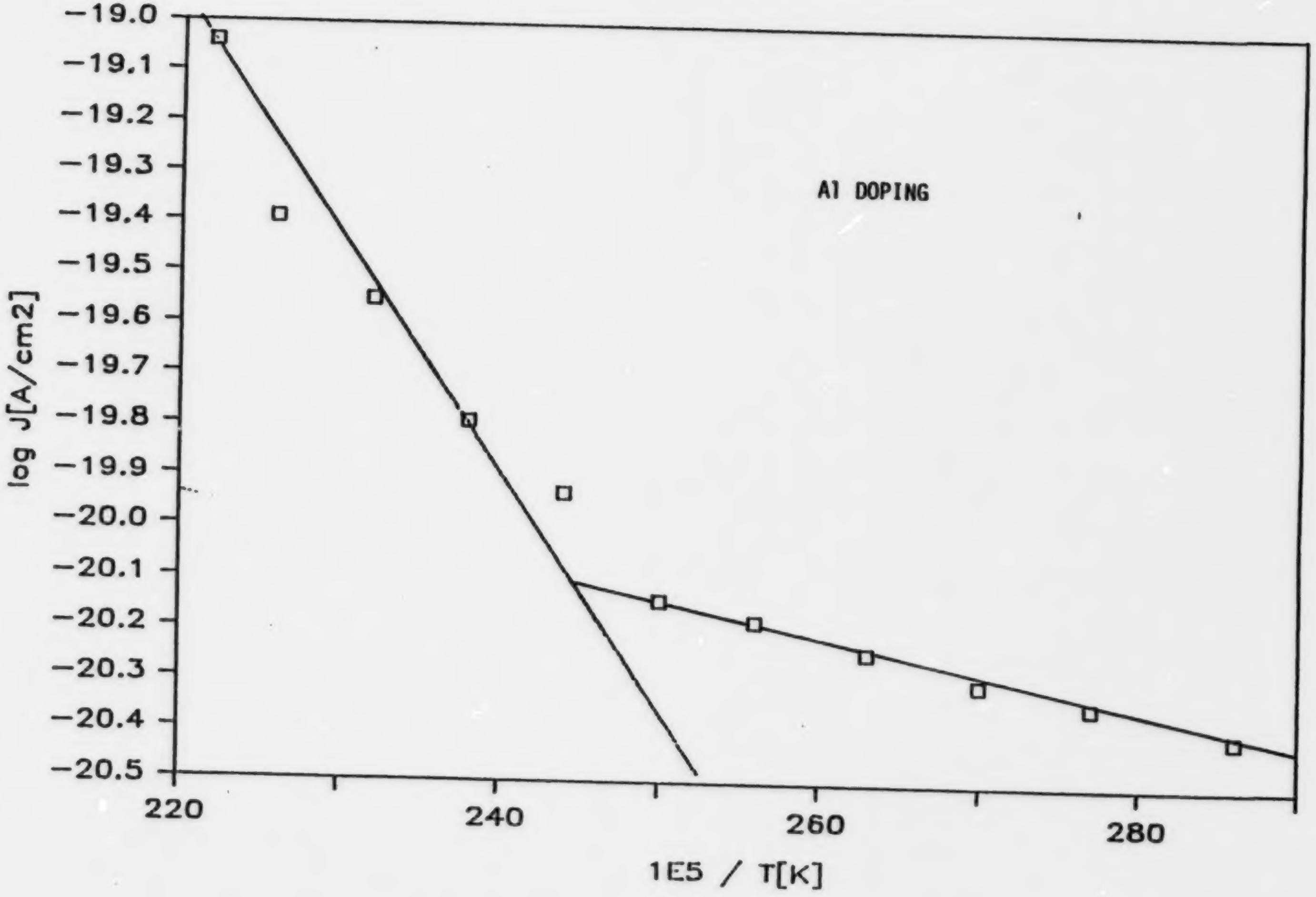

Figure 16 Arrhenius Plot of the DC Coplanar Current Density, Modified Arrhenius Plot.

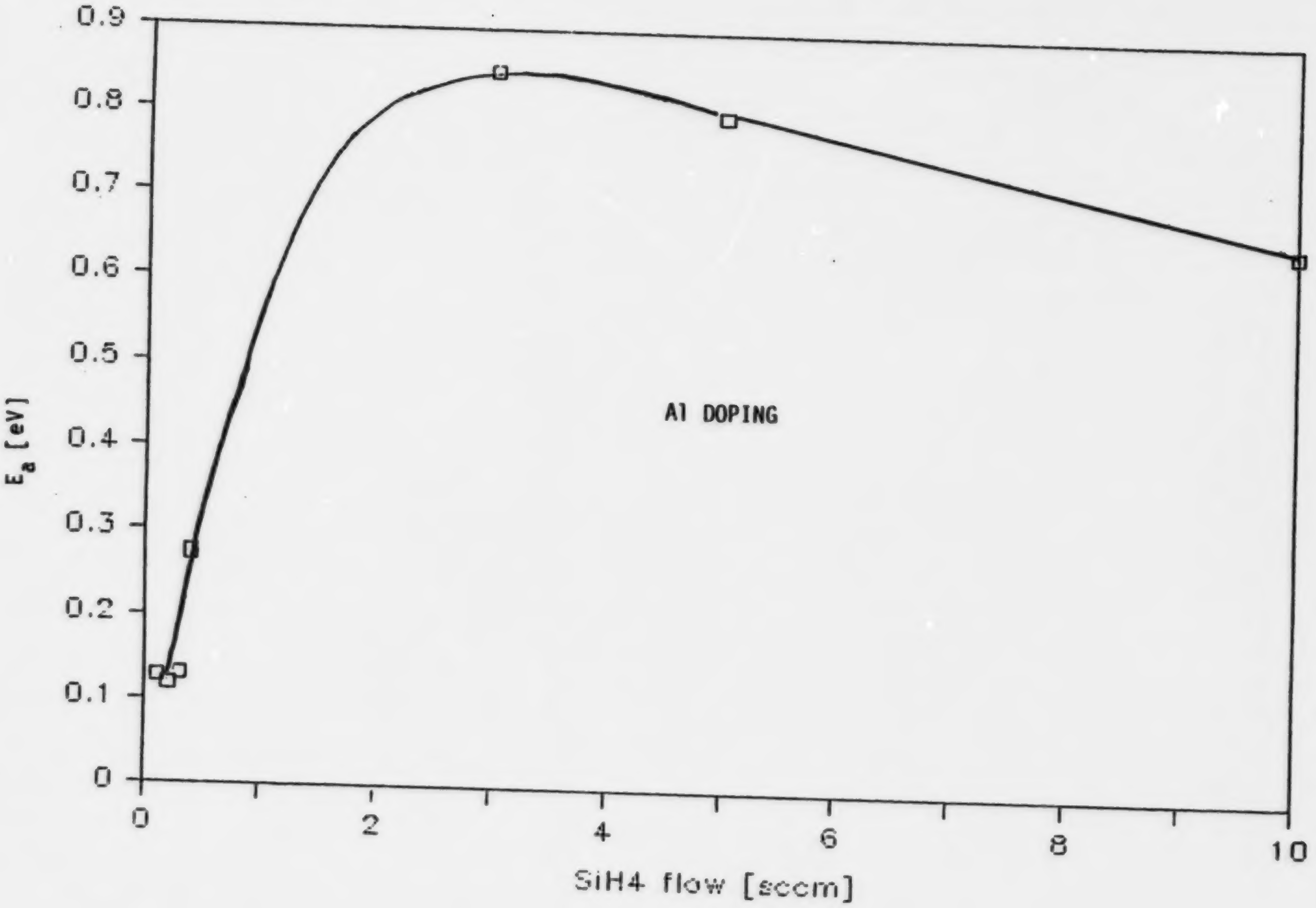

Figure 17 Activation of the Dark Conductivity vs Silane Mass Flow in the Glow Discharge.

There is some disagreement among the values of the activation energy E_a reported in the literature [18-24]. Fortune and Marshall [24] show that the change of activation energy is between 0.78 to 0.37 eV between 0 % and 8.5 % of Al, whereas Thompson and Reinhard [21] report that E_a ranges from 0.45 to 0.18 eV between 2 % and 10 % Al. In our measurements, Figure 17 shows a range from 0.83 eV for the compensated sample to 0.132 eV for the most heavily p-doped.

These results appeared quite promising. However, it was clear that, for p-i-n devices, we had to obtain conductivities higher than 10^{-3} S cm^{-1}, if at all possible. In order to understand the results presented above and to make further progress, it was necessary to know the relationship between silane flow and Al concentration, and between Al concentration and electronic doping. We also needed to know if the Al atoms were isolated (as we would hope) or whether they were clustered. In order to study these questions, we performed both XPS and SEM measurements. These are described later.

4.1.2 n-Type doping

As we had already achieved some success using Sb in evaporation doping and in making ohmic contacts, Sb was chosen as our n-type dopant. In a first series of experiments, the antimony doped layers were obtained by cosputtering Sb from the same electrode used for Al-doping, but covered with a 1 μm layer of Sb. Except for a power of 150 W and the a bias voltage between 250-280 V, the deposition parameters were unchanged.

In figure 18, we show the change of dark conductivity vs flow rate of SiH_4. A change of 5 orders of magnitude may be seen. In

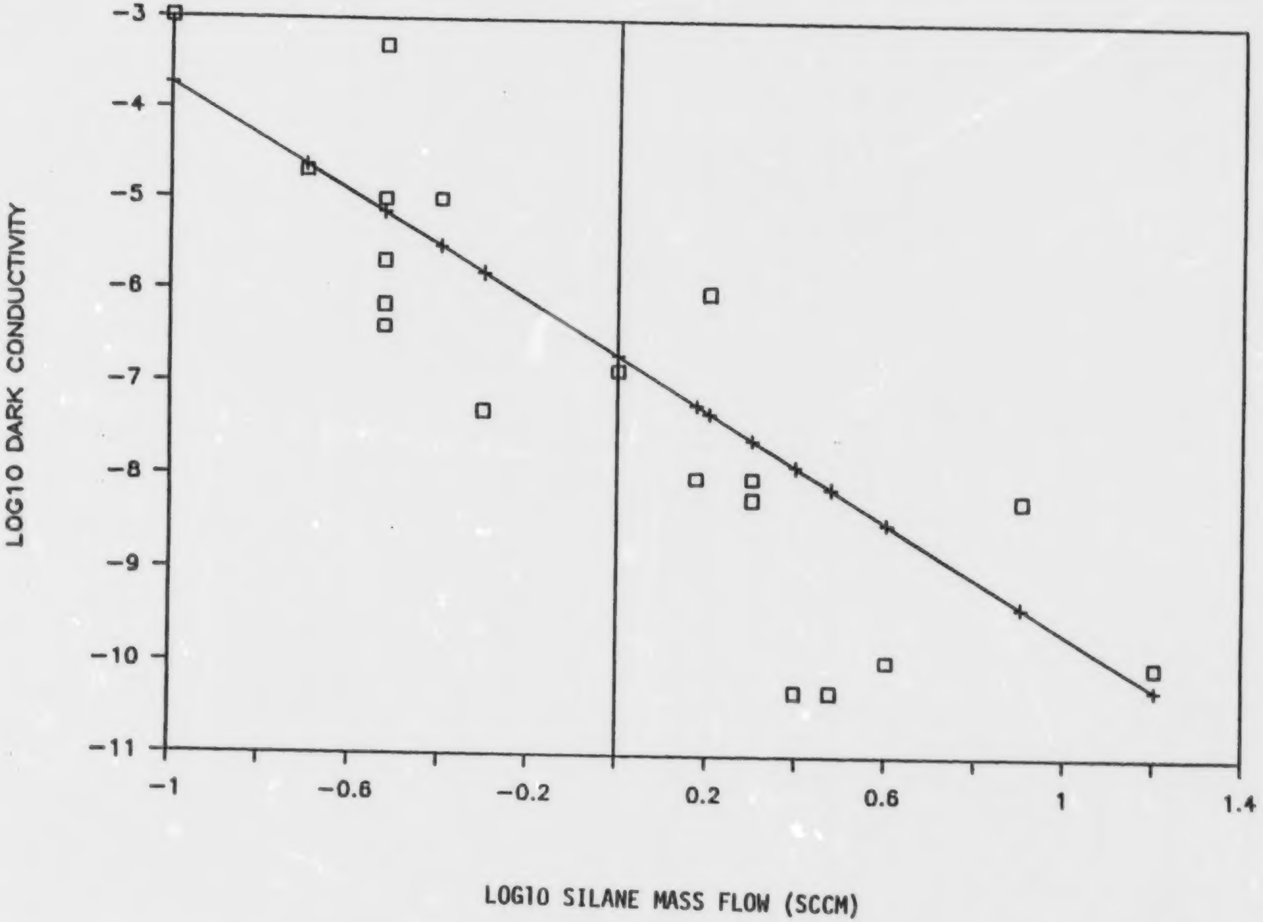

Figure 18 Log-Log Plot of Coplanar Dark DC Conductivity of Sb-Doped Amorphous Silicoon Vs Silane Mass Flow in SCCM
■: experimental points, +least-squares linear fit to data.

Ref. [25], the conductivity changes between 1 x 10^{-10} (Ω cm)$^{-1}$ for 0 % Sb to 10^{-5} (Ω cm)$^{-1}$ for 5.3 %, which is comparable to our results. As in the case of Al, we have observed the quenching of photoconductivity with increased Sb concentration. We concluded that we observed Sb-doping by cosputtering.

In a second series of measurements, results from two different deposition systems were compared. The conditions in the two systems are given in Table 4.1. The electrical properties of these samples were measured, as were XPS spectra. The results may be summarized as follows: the properties of the samples are very sensitive to deposition conditions. The XPS results suggest that this sensitivity is due to the presence or absence of clustering, depending upon these conditions. Hence, very careful and extensive studies of the effects of different deposition conditions will be necessary before optimum conditions can be established. We were not able to perform such studies with the time and budget available in this contract.

It is to be noted that the higest conductivity shown in Figure 17 is again 10^{-3} (Ω cm)$^{-1}$, much lower than we would wish for p-i-n devices.

4.2 Surface Analysis

Of primary concern here is the question of whether the dopant has been introduced in the proper chemical state to function electronically. The actual technique employed is known as ESCA

Table 4.1 Sensitivity to deposition conditions

	Parameters	Parallel Plate	Cylindrical Reactor
Substrate	Frequency (KHz)	100	100
Temperature	(°C)	300	250
Pressure	(mT)	100	100
Power	(W)	110	150
Volume	$V(cm^3)$	125	2 000
Power Density	(W/cm^3)	-0.9	-0.08
Air Flow Rate	D_{Ar} (sccm)	28	25
SiH_4 Flow Rate	D_{SiH_4} (sccm)	1.6	0.2-2
Bias Voltage	V_{DC} (V)	-400	-270
Interelectrode Separation	$\ell_{interelectrode}$ (cm)	5	2
DC Electric Field	F_{DC} (V/cm)	80	135

(Electron Spectroscopy for Chemical Analysis), or as XPS (X-ray Photoelectron Spectroscopy). It is a rather simple type of experiment, involving the measurement of photoelectrons emitted from a sample on X-ray irradiation. This simplicity is a distinct advantage here, because it aids interpretation. Appendix A gives more details on the technique itself and on its application to amorphous silicon, as reported in the literature.

The XPS spectrum contains peaks superimposed on a background, as seen in Figure 19. The peaks represent the electrons emitted from the various electron orbitals of the atoms probed, lying within about 20 A of the surface. In order to use this information, the background is computer-subtracted and the chemical shifts of the peaks are studied. Such chemical shifts are seen in Figure 20, where it is clear that they are determined by both their valence state and the ability of adjacent groups to influence the electron density about the atom of interest.

The first task was to calibrate the XPS data, and this was done by comparing them with data on the same samples, obtained by nuclear scattering. However, the nuclear scattering separation of Al and Si is not trivial. One sample, for example, gave an estimated 13 ± 3 % Al by nuclear scattering and a rather clear 10 % Al by XPS. Because of such difficulties with nuclear scattering, the determination of percentage of dopant was henceforth confined to XPS.

Two dopants were used, Al and Sb, and XPS indicates that both were incorporated chemically. This is based on spectral deconvolutions and comparisons with literature data. For Sb, doped in the cylindrical sputtering unit, under the following conditions: freq = 100 KHz, T_s = 250°C, p = 100 mT, P = 150 W. Flow rate_{Ar} = 25 sccm and flow rate_{SiH_4} = 0.2-2 sccm, it was found that the concentration of Sb incorporated into the film fit the equation:

$\text{Log}_{10}[\text{Sb}] \pm 0.19 = (-0.97 \pm 0.06) \times \text{flow rate}_{SiH_4} + 1.87$, with a statistical significance of > 99.95 %. A plot is seen in seen in Figure 21.

Antimony, Sb Atomic Number 51

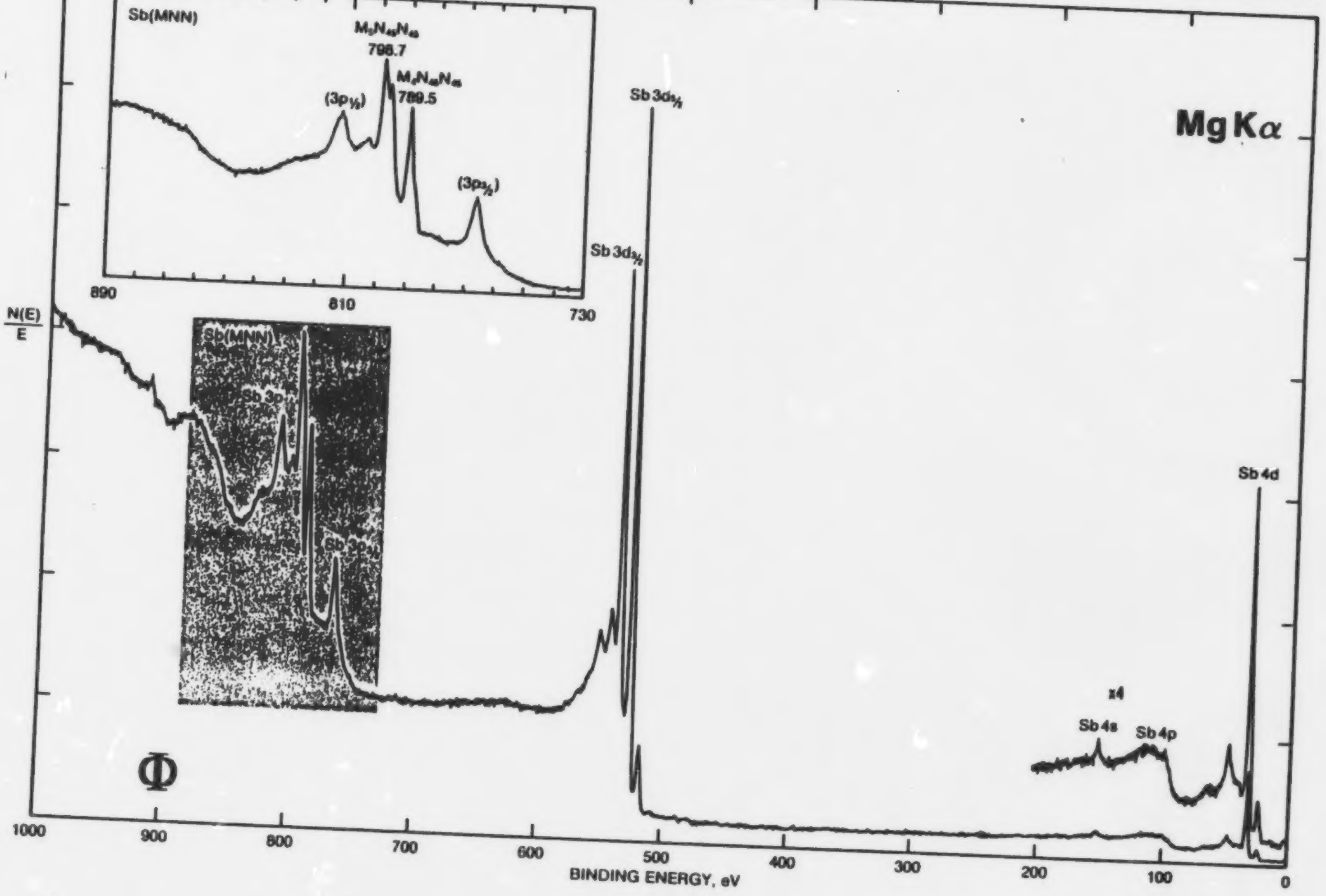

Figure 19

Antimony, Sb Atomic Number 51

HANDBOOK OF X-RAY PHOTOELECTRON SPECTROSCOPY

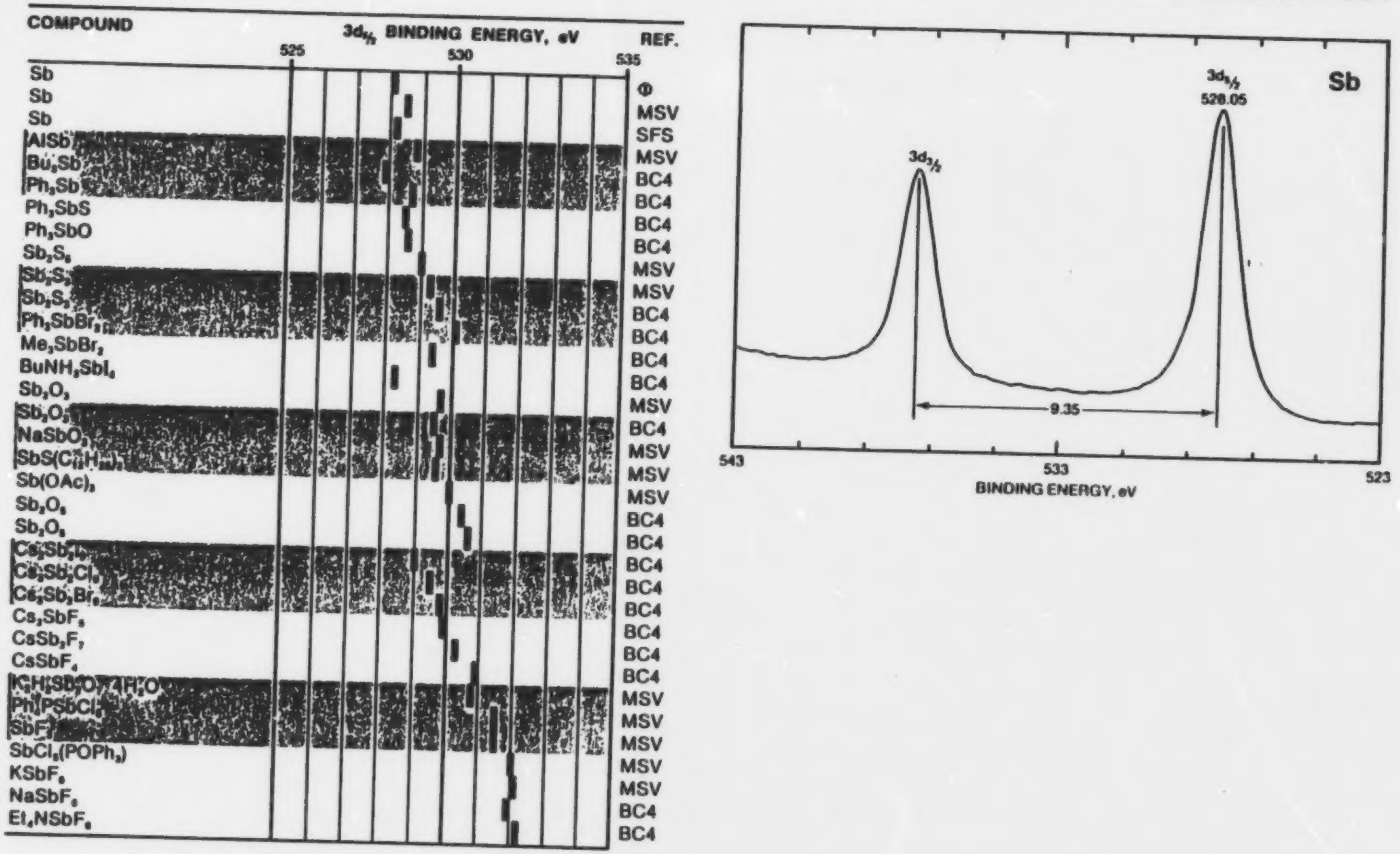

Figure 20

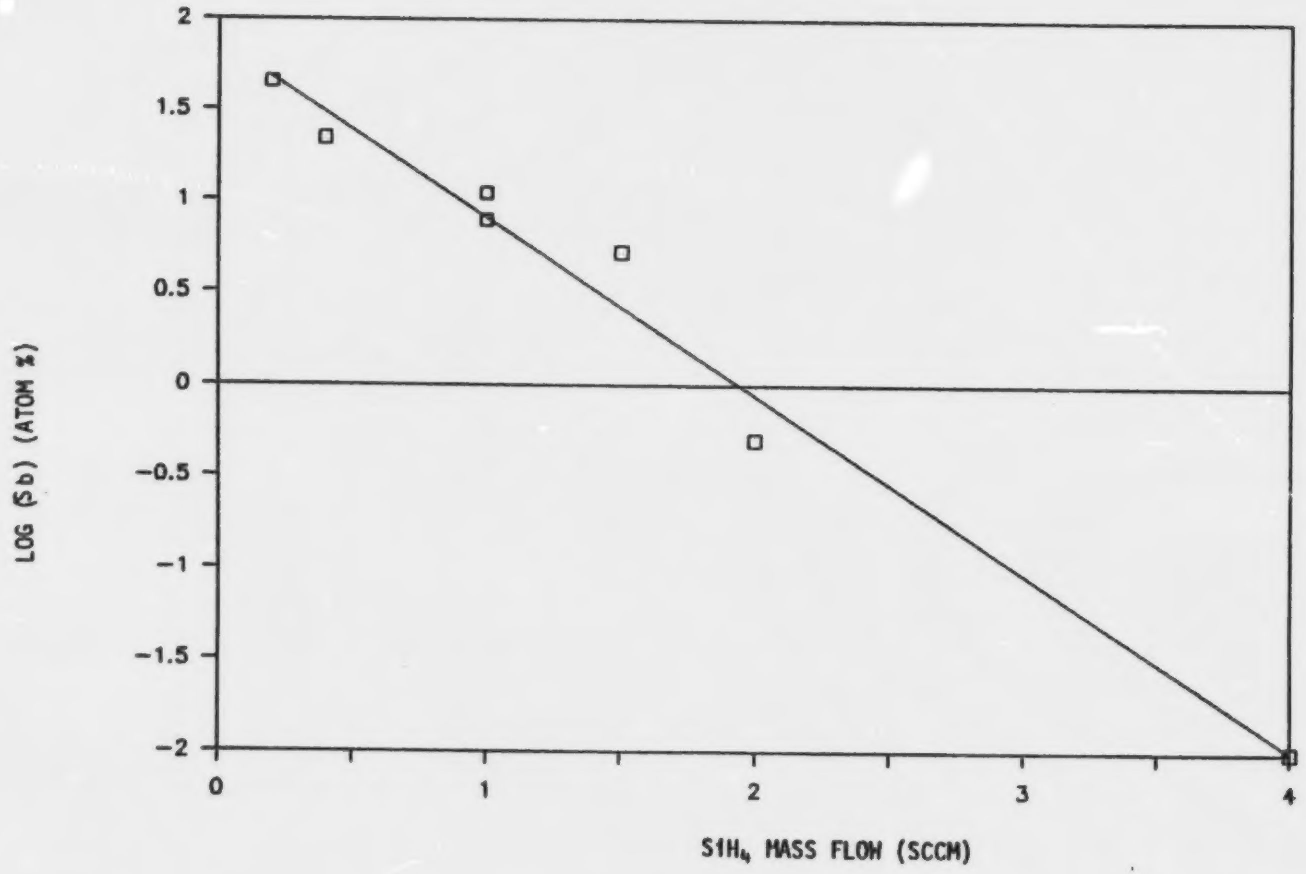

Figure 21 Semi-Log of Sb Concentration in atomic % in Amorphous Silicon vs Silane Mass flow Rate in sccm.

Deconvolution of the XPS peaks in the 530 eV range was carried out for two samples, #70303 (45 % Sb) and #70327 (5.2 % Sb). The resultant component peaks and their attributions are given below:

Table V XPS Results for Sb Doping

Peaks (eV)		Attribution	
#70303	#70327	Element	Type of Bonding
528.7	528.6	Sb $3d_{5/2}$	bonded antimony
529.9	530.1	Sb $3d_{5/2}$	Sb_2O_3
530.7	530.6	Sb $3d_{5/2}$	Sb_2O_3
531.8	531.8	O 1s	bonded oxygen

The Sb_2O_3 and Sb_2O_3 peaks correlate exactly with literature data, while the peak at 528.7 eV is assigned to bonded Sb rather than Sb° on the basis that it falls exactly where metallic bonded Sb (AlSb)is found. The difference between Sb° and Sb in AlSb is well within the resolution limits of the instrument.

Angle-resolved XPS showed that O/Sb increased as the take-off angle changed from 90° to 30°. Since the 90° angle probes - 2 nm in depth and the 30° angle probes - 1 nm (= 2 nm x sin 30°), it is clear that the oxidation occurs at the surface, a phenomenon which is well known and on which we have reported over the past few years. It is due to the existence of a surface layer rich in dangling bonds, due to the deposition process, itself.

In the parallel plate doping unit, the results are entirely different: in no case is doping by Sb indicated. Even at a 25 % Sb content, there is but one peak, at 527 eV, the proper value for Sb°.

The effort put into Al doping was not as intense as that put into Sb doping. Only one sample, containing 40 % Al, was deconvoluted. This was due to a manufacturer's error, in using an X-ray anode window thicker than specified in our XPS apparatus, reducing the sensitivity of the system to Al. In spite of this, the Al peak near 74 eV was obviously composite and was deconvoluted as follows:

Table 6 XPS results for Al Doping

Peaks (eV)		Attribution
#61216	Element	Type of Bonding
72.8	Al 2p	elemental
74.8	Al 2p	Al_2O_3
76.3	Cr 3s	elemental

Note that Cr, as an impurity, was confirmed by a survey scan showing the 2p doublet near 580 eV. Interestingly, while the study was incomplete, the Si 2p peak is at 98.3 eV, rather than at 99.1 eV; this suggests a negatively charged Si, such as might be expected for AlSi. That is, some fraction of the peak assigned to Al_2O_3 peak at 74.8 eV may, in fact, be due to AlSi.

Clearly, our knowledge accumulated on the Sb- and Al-doped samples has indicated that these doping techniques are not very efficient, since much of the dopant exists in the elemental or oxide forms.

5. DEVICE FABRICATION

5.1 Preparation

In the preparation of devices, essentially p-i-n photocells, we have attempted to devise an approach which involves as small a number of chambers and as small a number of transfers from one chamber to another, as possible. This has been for two reasons: first, in minimizing the number of chambers and of transfers one expects to reduce manufacturing costs. Second, since our material and equipment resources are limited compared with those of industrial laboratories, we cannot permit ourselves to build very elaborate systems.

When one turns from making individual layers to making multilayer devices, new problems, which had not affected the production of single layers, may arise. It is therefore necessary to find procedures which eliminate or minimize these problems. The first, most obvious, problem is that of cross-contamination.

This problem was thought to be far less serious in our case, using metallic dopants, than with volatile dopants such as arsine, phosphene our diborane, but it arises nonetheless.

Two approaches were taken to resolve this problem. First, rigorous cleaning procedures between use were instituted. Second, a sequence of deposition steps which we hoped would minimize the problem was established. The following sequence was initially employed:

1° Evaporation of Cr electrodes on glass,

2° The exterior electrode, covered with evaporated Sb film about 1 μm thick, is covered with a pure aluminum foil, so that Al may be sputtered, 3° A p-layer is deposited,

4° An i-layer is prepared under conditions yielding a light-to-dark conductivity ratio σ_{ph}/σ_d of about 10^5,

5° We wait about 6-7 hours for the samples to cool, and then the reactor is opened for 2-3 min. to remove the Al foil,

6° The n-layer 200-300 µm thick is deposited by cosputtering Sb,

7° The diode is completed by evaporating a 100-200 µm layer of Sb.

This led to a considerable reduction in cross-contamination, but did not substantially improve photovoltaic yields. Electrical measurements indicated that neither the n nor the p regions were behaving as they should. XPS measurements indicated that there was not sufficient interdiffusion between the n-layer and its contact. When the contact is made first, this interdiffusion is produced by sputter-cleaning the electrode as the semiconductor is deposited. If the semiconductor is deposited and the contact is evaporated onto it, this effect does not take place and the contact resistance is too high.

In subsequent work, the order was reversed, with the Sb and n-layers deposited first, and the p-layer last. This procedure yielded n-layers and contacts of very high quality as demonstrated by the fact that it has produced Schottky cells with 5.9 % efficiency versus our previous maximum value of 5.3 %. Moreover, our p-i-n structures now had efficiencies of > 2.5 %.

The p-layer continued to pose difficulties; these difficulties arise from three sources. First, the opening and closing of the system creates several opportunities for contamination. Second, as is always the case, p-doping of a-Si:H is more difficult than n-doping. Third, p-doping may be complicated by clustering problems.

We also fabricated a few cells with conducting oxide layers instead of semitransparent metal. In principle, this structure should increase the yield, as it should substantially decrease light losses both from reflextion and from absorption in this layer. These cells, fabricated on commercial oxides on glass, were not satisfactory.

5.2 Electro-Optical Characterization of p-i-n Devices

The proper functioning of a solar cell depends on its electrical properties, determined in both the absence and presence of solar illumination. These measurements include I-V characteristics to obtain photovoltaic efficiencies, fill factors FF, open circuit voltages V_{OC} and short circuit currents J_{SC}. Solar cell efficiencies are then given by

$$\eta = \frac{FF \cdot V_{OC} \cdot J_{SC}}{P_{IN}}$$

where P_{IN} is the power density (in W/cm²) arriving on the cell and the fill factor is $FF = (V_M\ J_M)/(V_{OC}\ J_{SC})$, and V_M and J_M are the voltage and current density corresponding to the maximum power density product.

We have characterized two principal p-i-n structures shown in Figure 22. Our studies of p-i-n junctions are mostly done on glass substrates with the Cr-Sb evaporated electrode (structure A). We have assumed, based on studies in our laboratory, that the antimony, diffusing from the electrode to the intrinsic layer of a-Si:H deposited by glow discharge of SiH_4, gives the thin n-layer necessary for good chemical contact. The p-layer is made in the second step of deposition by cosputtering Al from the Al foil covering the electrode.

A few preliminary trials were made with ITO (Indium Tin Oxide) thin layers as substrates (structure B). In this case we obtain p-i-n junctions illuminated from the under side.

(A) Structure Glass + Cr - Sb

GLASS	Cr - Sb	i-a-Si:H	a-Si:H(Al)		hν
	2000-400Å	5000-7000Å	300-400Å	100Å	←
	N	I	P		

(B) Structure Glass + ITO

hν

→	GLASS	ITO	i-a-Si:H(Al)	a-Si:H	a-Si:H(Sb)	Sb or Al
		500Å	200-300Å	5000-7000Å	300-400Å	1000Å

Figure 22 p-i-n Structures

Table 7 presents the maximum and average open circuit voltages V_{OC}, short circuit currents J_{SC}, fill factor FF and efficiency for the first structure. While these measurements were done under 35 mW/cm² illumination, we have recently begun to measure photovoltaic efficiencies with a 100 mW/cm² solar simulator. By employing an ITO transparent conductive top contact and adjusting its thickness to minimize reflection losses, efficiencies are improved by at least 40 %.

Maximum efficiency values are in the range 2 to 3 %. This is a factor of two lower than our target. Various problems have to be considered in order to increase η. While the fill factors, FF, are good but not optimized (which should be ~ 0.6 - 0.7), the J_{SC} ~ 18 mA/cm² and V_{OC} ~ 0.88 V under 100 mV/cm²; for 35 mW/cm² we can estimate that J_S ~ 6 mA/cm²).

Table 7 Maximum and average open circuit voltages V_{OC}, short circuit currents J_{OC}, fill factor FF and Efficiency η for the "A" structure under 35 mW/cm² Illumination

Structure		V_{OC} ((mV)	J_{SC} (mA/cm²)	FF	η
(A) glass + Cr/Sb	Maximum	500	4.5	0.4	2.8
	Average	450	4.5	0.35	2.0

5.3 Identification of the sources of difficulty in obtaining high quality devices

A.C. Electrical characterisation of amorphous silicon

Amorphous silicon produced in the cylindrical reactor at the École Polytechnnique has been studied using a dielectric spectroscopic technique. The technique uses a Solartron Frequency Response Analyser to generate a sinusoidal waveform at several discrete frequencies in the range 10^{-2} to 10^{4} Hz. The waveform is placed across the series configuration of sample and measuring box (which contains the reference impedance(s)). The potential across the reference impedance is measured with respect to ground by the FRA input (correlator) which sees an input signal which is different in amplitude and phase from the generated waveform. An integration of the input signal is performed by multiplying the input signal by appropriate sine and cosine functions. The results are then proportional to the in-phase and quadrature components of the voltage respectively. Having obtained the magnitudes of the components of the voltages the complex capacitance components of the sample are obtained by comparing the products of admittance and voltage (expressed in complex form).

Dielectric spectroscopy of semiconductors allows us to study the displacement motions of charge groups under the action of an imposed external field. In semi-insulating materials, we may imagine dividing up the sample into three distinct regions:

a) Interface between metal and semiconductor which may be composed of a thin oxide layer or in the particular case of a-Si:H a silicide layer formed by chemical reaction of deposition metal and reactive surface.

b) Schottky barrier or, at least, some internal surface which resembles a classical Schottky barrier. To this extent, we require that the parallel barrier conductance should show some distinct bias dependence which should approximate to the familiar current-voltage characteristics of a diode. In addition, some distinct bias dependence of the capacitance should also be expected.

c) Volume response. The volume or bulk of the semiconductor is defined as that region of the semiconductor which extends from the edge of the depletion layer at the top contact (small area) to the back contact. We assume that the back contact is ohmic, in the sense that its contribution to the total impedance is small compared to the other contributions, since its geometric area is much larger than that of the top contact.

Cases (b) and (c) will be considered in some detail while case (a) represents a very low frequency effect and is not encountered in the present work.

Our samples are prepared in a sandwich geometry. In most cases the active area of the back contact is large although comb-like electrode arrangements are equally manageable.

5.4 A.C. Characterisation of samples in terms of their deposition parameters

A number of samples were chosen which had reportedly been grown under identical power conditions (5 W) but the effective deposition rate for each sample was different. It was postulated that with all else being equal, we would expect to observe some change in the frequency position of the deep-trap signature as a function of growth rate. The above term relates to the fact that a deep-trap may be considered to release its charge at a low rate (- 0.1 to 10 s at 300 K). In a frequency response measurement, the complex capacitance components exhibit some frequency dependence according to the mechanism which leads to an overall change in the occupancy of a trapping centre. In addition, as the number of ionized centres in the depletion region increases (i.e., as the occupation of the centres approaches its equilibrium value), so the amplitudes of the components of the complex capacitance also increase. This may or may not lead to a truly static low frequency capacitance. The total description is completed by a parallel geometric capacitance (either geometric of volume or depletion region).

A typical result is shown in Figure 23 for sample 60430 on a steel substrate with a small area Cr top contact. The characteristics show a geometric capacitance which is largely independent of frequency above 100 Hz with an increment in the capacitance below this frequency. A peak in the dielectric loss is observed at approximately 3 Hz. The frequency dependence of the high frequency slope of the loss is -0.89; no slope for the low frequency side of the loss-peak can be assigned; however, typical values obtained from other samples suggest a value of 0.1. The value of the low frequency slope is masked by the parallel d.c. conductance. In the absence of supporting evidence from other techniques, we assume that the origin of the deep-centre response arises from dangling bond defects in the middle of the gap.

Figure 24 shows a typical room temperature result for sample 70105. The frequency of maximum loss occurs at approximately 100 Hz. However an additional lower frequency process may be observed [MRS Proceedings, 1988]. In this case the high frequency slope is of the

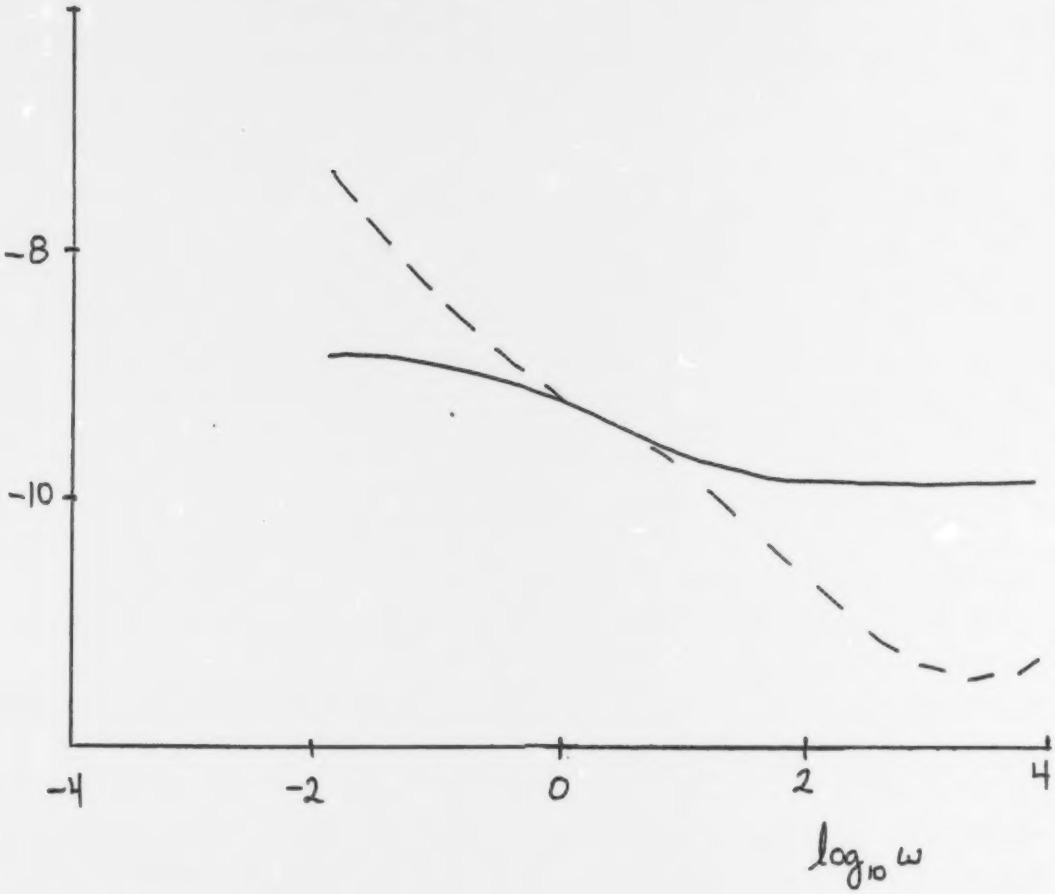

Figure 23 Log-log plot of the AC capacitance, C(——), and of the conductance, G/ω (---) vs angular frequancy, ω, for sample #60430 as measured at 297°K.

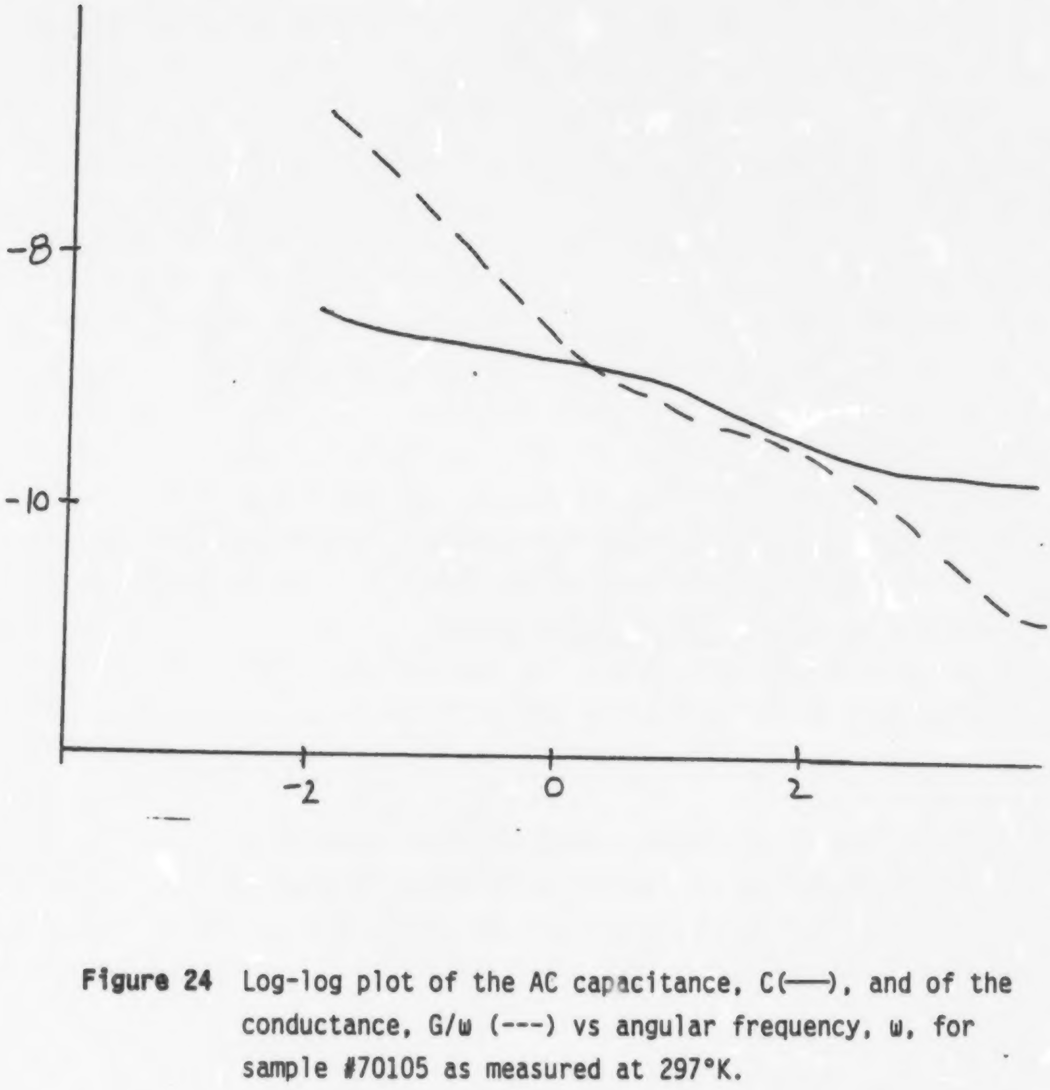

Figure 24 Log-log plot of the AC capacitance, C(——), and of the conductance, G/ω (---) vs angular frequency, ω, for sample #70105 as measured at 297°K.

Table 8 Amorphous Silicon Deposition Conditions
Electrical Characteristics

Dep. Rate (μm/hr)	peak freq (Hz)	act. energy W1 (eV)	act. energy W2 (eV)
0.25	2 000	0.44 - 1.25	0.17
0.25	1 000	-	-
0.27	10	- 0.6	-
0.5	20	0.72	0.74
0.5	100	0.7	0.72
0.6	3	-	-
1.3	2	0.77	0.93
1.5	1	-	-

order of -0.85. Table 8 shows typical results obtained for these and other samples. The peak frequencies are estimates although more exact values have been obtained using simple dielectric response functions.

Having estimated the peak as shown in Table 8, this value was plotted against reported deposition rate and the result is shown in Figure 25. Although the experimental evidence is sparse and the peak frequencies are estimates, there does appear to be some discernible trend in the behaviour. For those samples for which we have activation energies (frequency response of sample measured at several fixed temperatures), we obtained Figure 26, which represents a plot of deposition rate against peak activation energy. Clearly, a trend is obtained. This suggests that to minimize the position (and possibly number) of mid-gap states, it is necessary to regard a deposition rate of 0.25μm/hr in the capacitive plasma unit as a critical point, above which the depth of the mid-gap centre is a strong function of the deposition rate.

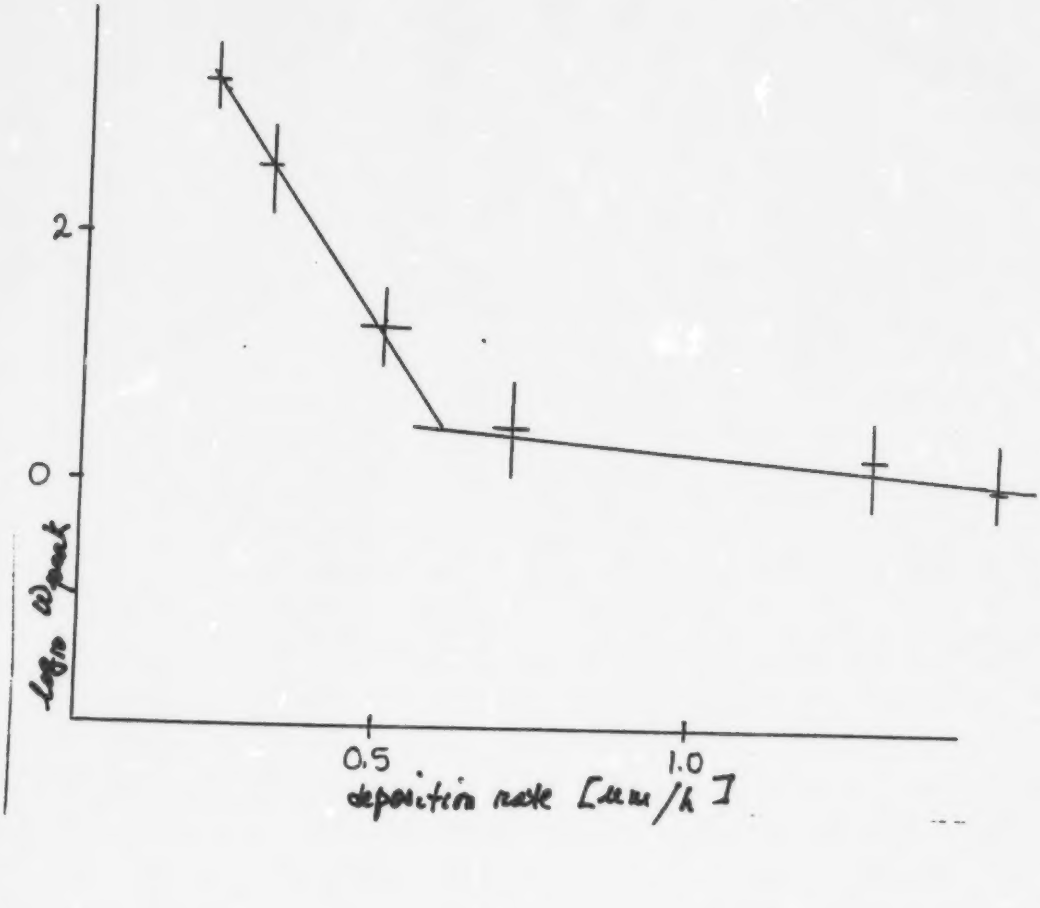

Figure 25 Semilog plot of the frequency [Hz] of peak AC loss vs deposition rate [μm/h].

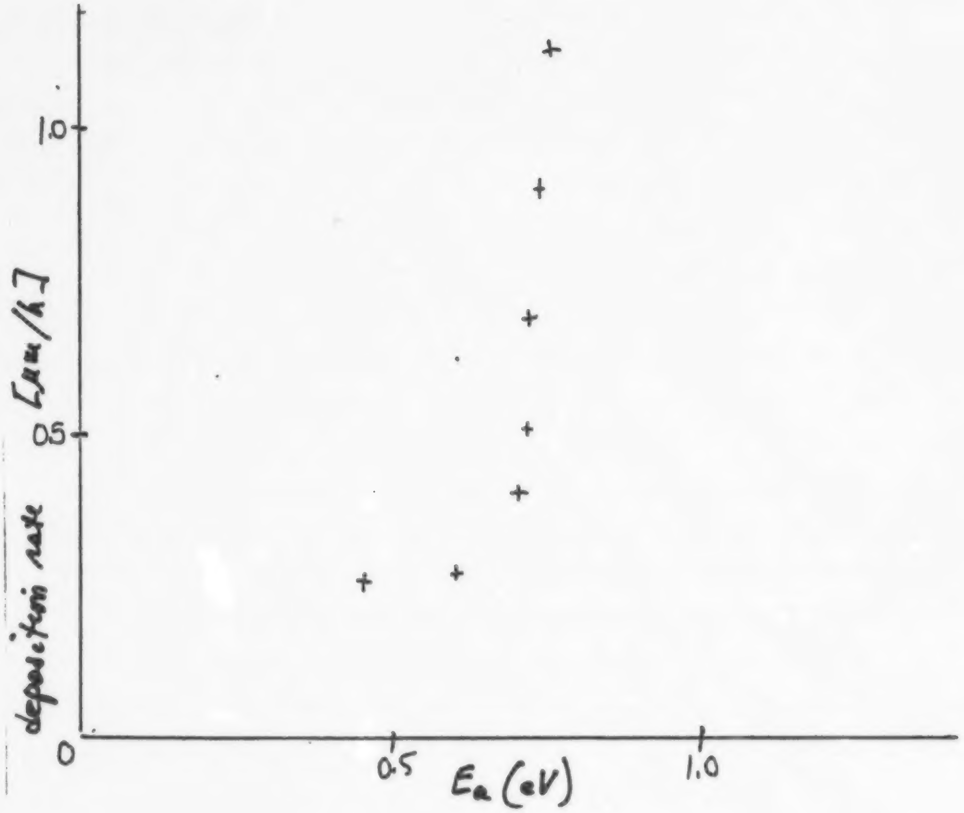

Figure 26 Plot of film deposition rates [μm/h] vs measured activation energies [eV] of AC peak loss frequencies.

This suggests that the thermalisation time for trapped charge is significantly longer in material which is grown under fast rate conditions. It may of course be possible to optimize other parameters in order to speed up the deposition rate and still have low trap density annd short thermalisation time of carriers in the trap state.

Figure 27 shows typical activation energy curves for sample 60430. The characteristic activation energy for the deep centre (i.e. energy separation of trap from a band edge) is 0.77 eV. The activation energy of the parallel conductance is 0.93 eV. A complete summary of the observed critical frequencies and activation energies for several typical samples is given in the Table 8.

5.5 Surface Analysis

Surface analysis was carried out with several instruments, including:

XPS - Xray photoelectron spectroscopy: core electrons
UPS - Ultraviolet photoelectron spectroscopy: valence electrons
IR - Infrared spectroscopy: structural vibrations
AES - Auger electron spectroscopy: electronic transitions

Each has certain advantages and disadvantages, the advantages of one being used in an effort to overcome the disadvantages of another. Two questions were addresses:

1. What is the chemical structure of the a-Si:H matrix?
2. How does the dopant incorporate within that structure?

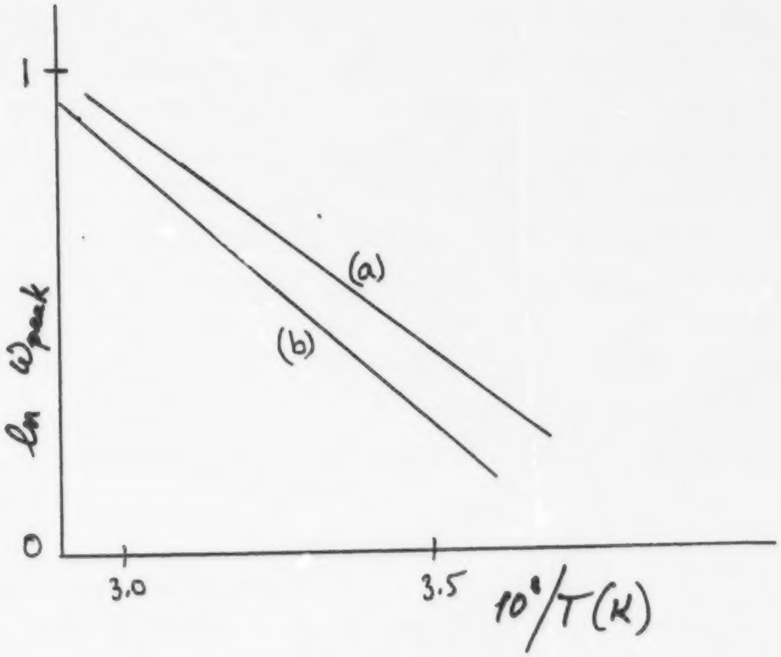

Figure 27 Arrhenius plot of the logarithm of the peak AC loss angular frequency vs 1 000/T[°K] for sample #60430 as deduced from (a) capacitance, and (b) conductance curves. The two activation energies are (a) 0.7 eV, and (b) 0.93 eV.

5.5.1 Matrix Structure

The chemical structure of the matrix is important. There is evidence [18] that the photovoltaic efficiency increases as the fraction of Si-H increases. This fraction is estimated from the IR spectrum in the 2 000 - 2 100 cm^{-1} region, where $\nu_{\text{Si-H}}$ and $\nu_{\text{Si-H}_2}$ differ by some 70 cm^{-1}. We, too, have attempted to use IR as a tool for gauging the Si-H fraction but, as seen in Figure 28, it is a qualitative tool. This is supported by our recent demonstration [13] that this region contains several other peaks which do not correspond to Si-H_n, as yet unattributed. Instead, we have used XPS to separate the Si-H_n fractions, as in ref. [20]. Here, we use the Si 2s photoelectron peak, avoiding the necessity of separating the spin-orbit multiplets of the more commonly used $2p_{3/2,\ 1/2}$ peaks. An example is seen in Figure 29. In every case, this quantitative determination agreed with the qualitative IR spectrum. Both techniques revealed that, all other parameters held constant, the Si-H fraction increased with decreasing Ar flow and with decreasing plasma power. In no case was Si-H_2 or Si-H_3 eliminated, as seen in Table 9.

Table 9 Si-H_n production as a function of plasma parameters

Temperature (%)	Pressure (mT)	Power (W)	$\text{Si-H:Si-H}_2\text{:Si-H}_3$
250	200	60	5 : 2 : 1
250	200	10	7 : 2.5 : 1
250	100	100	0.5 : 1.3 : 1
300	200	10	7 : 2.5 : 1
300	200	10	15 : 4 : 1

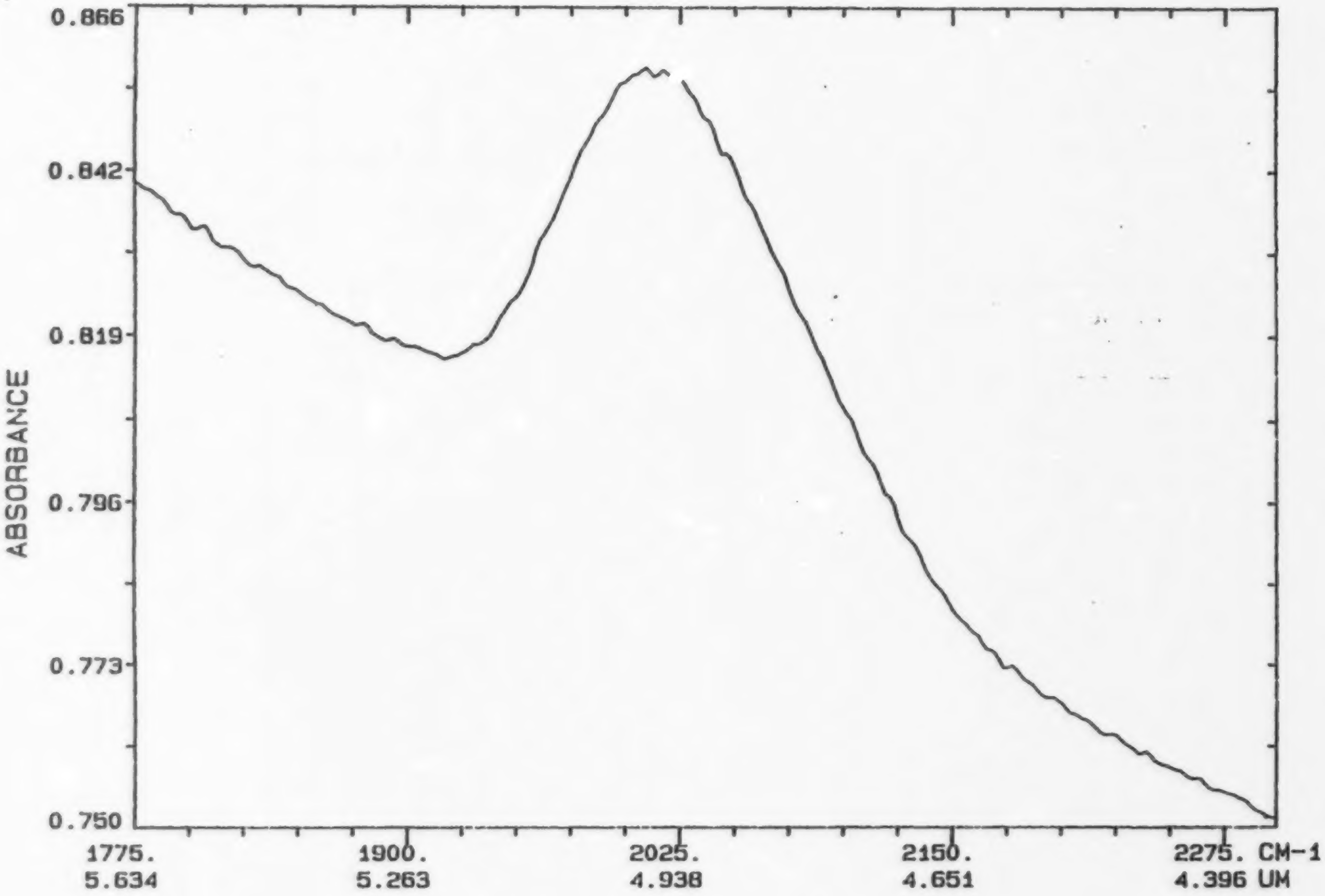

Figure 28 An IR spectrum of sample 80425, showing a qualitatively greater fraction of Si-H (2 000 cm^{-1}) than Si-H$_2$ (2 070 cm^{-1}) and Si-H$_3$ (2 120 cm^{-1}).

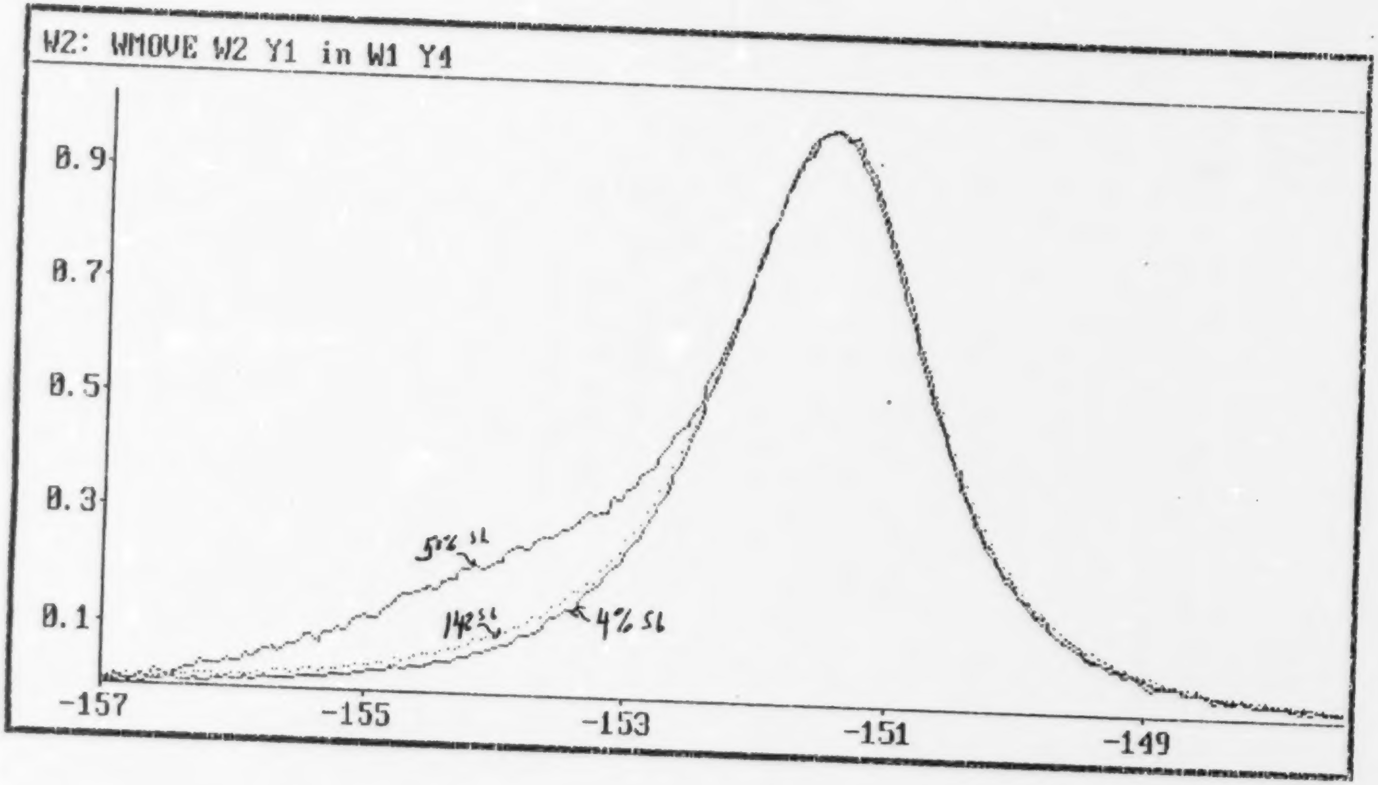

Figure 29 An XPS spectrum of the 2s emission of Si for three different Sb concentration: 4 %, 14 % and 53 %.

5.5.2 Dopant incorporation

Contrary to most views on the subject[21], the low dielectric constant of a-Si:H does not support the existance of free ions. Further, reactions in a-Si:H are understandable in terms of reactions known to occur to monomeric silanes.

For example, a special type of second order nucleophilic substitution, referred to as S_Ni-Si [22], is known to occur in silanes; it involves a cyclic transition state (presumably due to d-orbital participation) and, unlike such reactions in hydrocarbons, leads to a retention of configuration. This latter point is emphasized because it permits direct substitution at a surface. Note that nucleophilic substitution requires that a nucleophile (i.e. an electron rich moiety, such as an n-type dopant) be incroporated though substitution. Electrophiles (i.e., an electron deficient moiety, such as a p-type dopant) are expected to add by normal free radical or electrophilic addition (as opposed to substitution). The literature contains clear evidence for both, as determined by nuclear scattering profiles: Sb and As found to substitute H [23, 24] and As was found to substitute Si [25], while B did not correlate with any of the other elements present [26], as expected for an addition.

In the case of Sb, which we have studied most extensively such a substitution reaction would lead to the Sb giving up its electrons to the Si, leaving it more positive and the Si more negative. In terms of XPS spectra, this would mean that a component of the Sb spectrum has shifted to higher energy and a component of the Si spectrum has shifted to lower energy. On the other hand, given their calculated electronegativities [27] of 4.92 for Si and 5.15 to Sb, one might expect to see the opposite XPS shifts.

One should note that a positively charged nucleophile is the species normally considered [21] to participate in doping. Although the electronegativity calculations are for individual atoms and the situation may well change for Sb bonded to Si, the data at least suggest that the more stable form of Sb in the a-Si:H matrix is one in which the Sb attracts electron density. This is, indeed, what is found experimentally: Figure 30 shows the 2s XPS spectrum of a-Si:H doped with Sb. There is clear evidence of a component at higher energy, indicating the Sb-Si bond is polarized so that Si is more positively charged. A similar spectrum shows Sb to be more negatively charged. This finding leads to several serious questions about the existance and the mechanism of doping in a:Si-H, as it is presently considered to occur in c-Si.

One of the drawbacks of the sputtering process is the tendency to introduce the dopant in an unreactive form. Ultimately, this neutral Sb is able to migrate, as seen in Figure 31. Here, it is clear that Sb migration has led to Cr/Sb intermetallic compound formation at the Cr electrode. While this may be corrected through the use of gaseous dopant, another migration problem, also seen in Figure 31, may be more difficult to correct: the interaction of the outer (in this case, Pt and Al) electrode with the Si. Note that the outer electrode is deposited by sputtering: where measured [28, 29], the depositing species have average energies of ~40 eV, with tails extending to much higher energies. It is clear [30] that such depositions provoke chemical reactions. Even evaporating such electrodes releases a latent heat of condensation [30], enough to provoke chemical reactions. Silicon is particularly reactive, many silicides being known [31], making it unlikely that such reactions can be avoided.

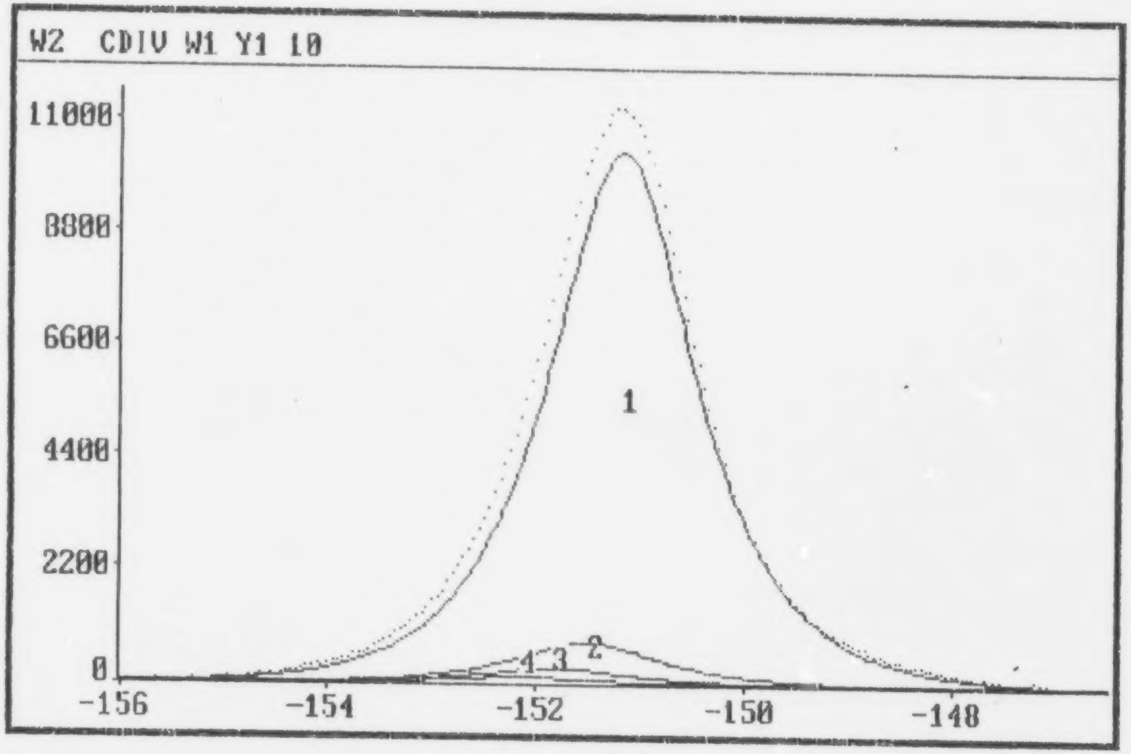

Figure 30 An XPS spectrum of the 2s emission of Si, showing Si(1), Si-H(2), Si-H_2(3) and Si-H_2(4).

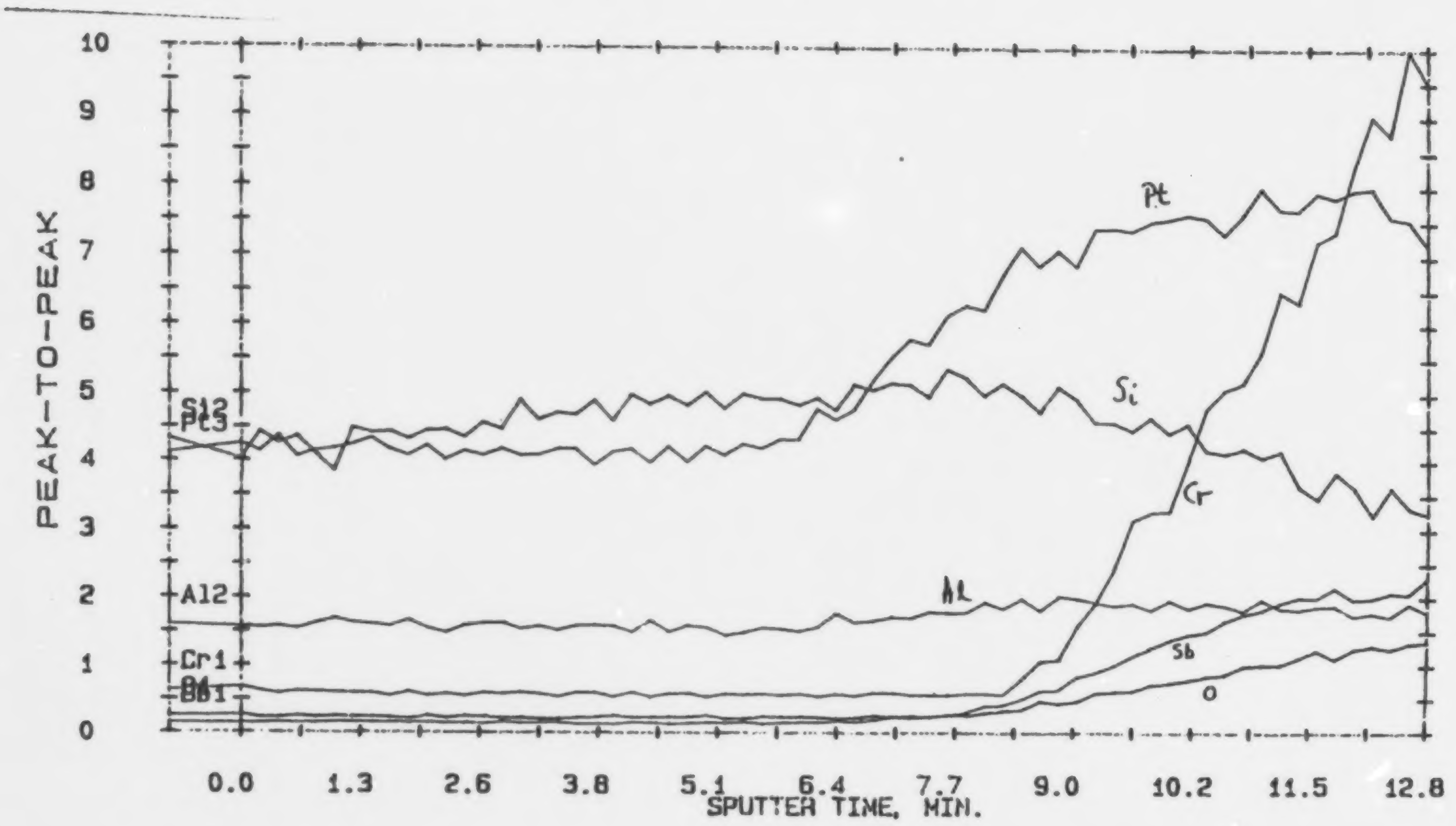

Figure 31 An Auger profile of sample 71127-1, showing Sb migration into the Cr back electrode and Pt migration into the Si.

6. DOPING BY THERMAL DIFFUSION

6.1 Preparation

We have tried two methods of thermal diffusion which differ by the preparation of the deposited layer. Silicon wafers and glass were used as substrates. The intrinsic layer of glow-discharged amorphous silicon, about 2-3 μm thick, was deposited at 270°C.

In the first method a layer of antimony was sputtered on amorphous a-Si:H layer, which had been previously deposited in the same reactor. Without breaking the vacuum we could diffuse at 300-350°C for few hours. After diffusion, the excess antimony was removed in acid and aluminum electrical contacts were thermally evaporated.

The second method differs only in the way the dopant is applied. We have used a commercially available spin-on glass layer rich (~ 1% at.) in dopant metal. The glass layer appears to act as a diffusion cap which keeps hydrogen from escaping from the silicon film.

6.2 Electro-Optical characterization

For the first method of metal diffusion, the I-V measurements for an intrinsic a-Si:H layer (Fig. 32) and for a Sb-doped one (Fig. 33) show evidence of doping. The I-V measurements done at different temperatures give the estimated value of energy activation 0.2 eV.

The second, (spin-on), method has not yet given reproducible current-voltage results. In most cases, the conductivity is low, barely a decade higher than that of intrinsic a-Si:H.

A lack of initial success caused us to drop this method, in favor of gas phase doping.

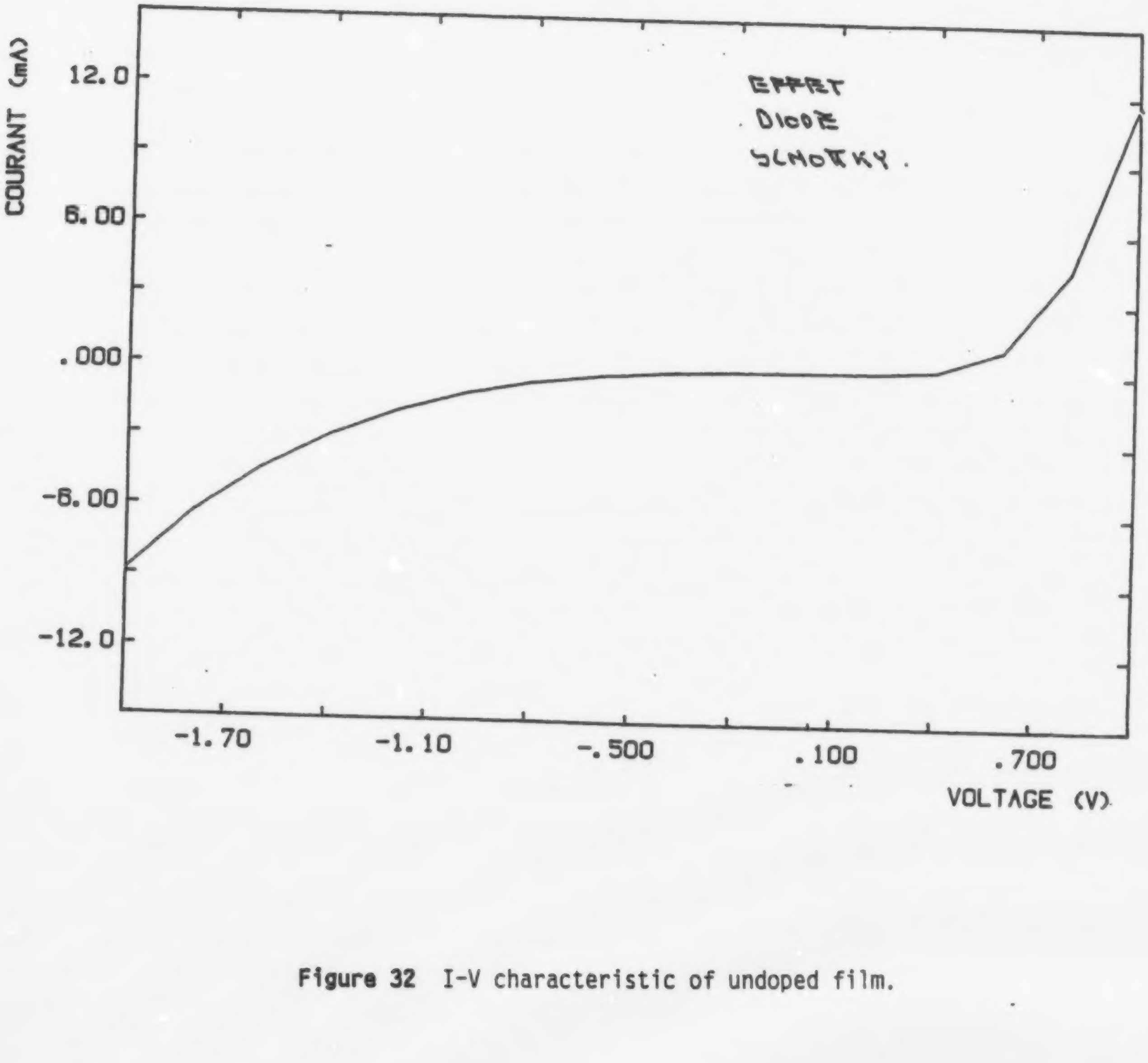

Figure 32 I-V characteristic of undoped film.

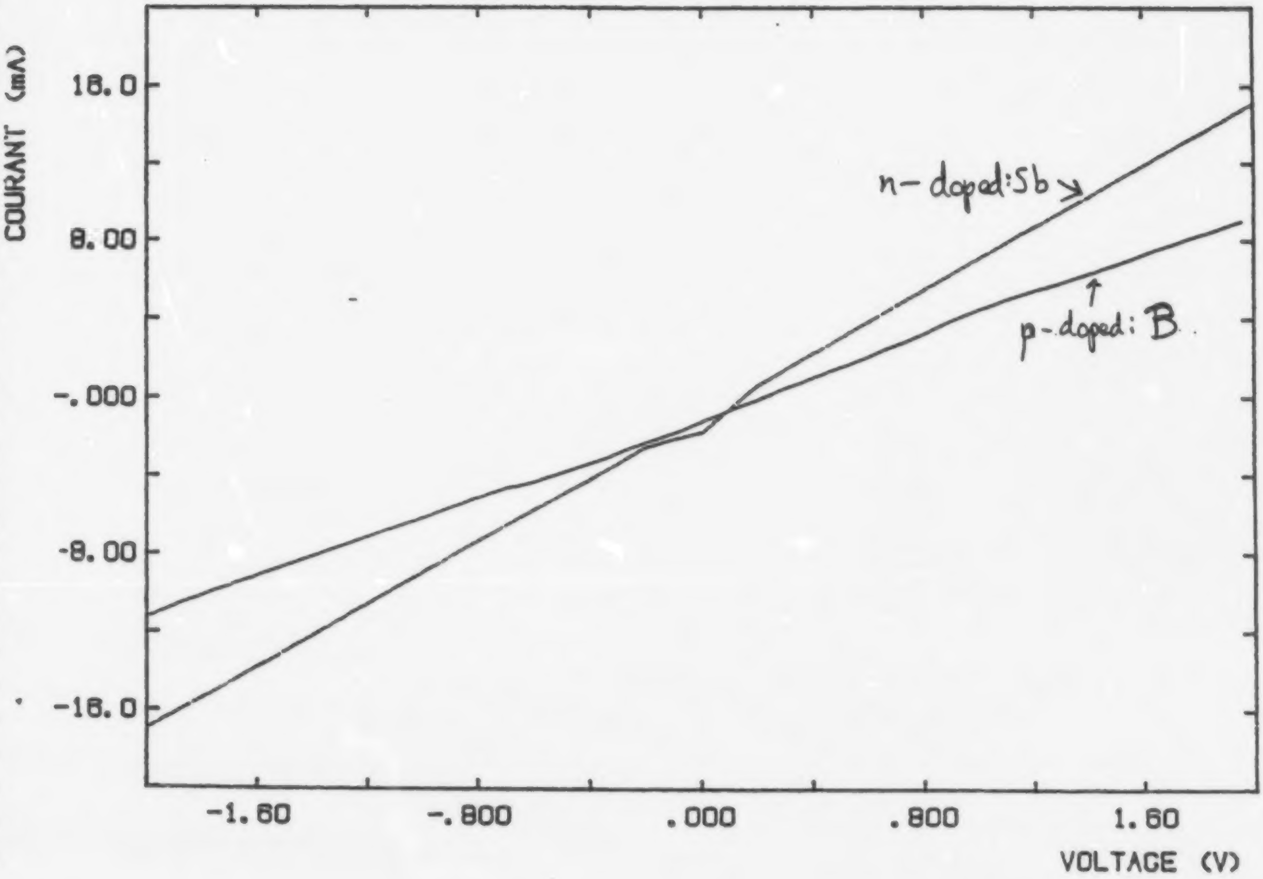

Figure 33 I-V characteristics of metal-diffused films.

7. GAS PHASE DOPING

7.1 Modification of film deposition laboratory

The use of diborane and phosphine gases requires even more care than silane. These gases are toxic at the level of a few parts per billion. Their use requires the installation of a highly specialized gas distribution system, leak detection, and effluent burning systems, as well as modified laboratory partitioning and ventilation.

Included in Figure 34 are three photographs showing:

(1) The installed doping gas cabinets, and behind them the command electronics for the mass flow controllers.

(2) A close-up of the doping gas piping and mass flow controllers installed inside the cabinets.

(3) The film deposition system to which the doping gases are delivered. Visible at the left is the new HEPA filter block used to eliminate particulates during handling.

7.1.1 Gas Phase Doping of a-Si:H

Use of phosphine and diborane, both highly toxic hydrides, require special handling capabilities. To this end we constructed a clean isolated room capable of a "negative pressure" regime, inside which we installed gas cabinets which contain the hydrides. The gas cabinets are specially designed for hazardous toxic gases with exhaust stacks, self-closing, self-latching doors and sprinkler heads. Each hydride bottle is connected to a panel mounted 5-valve purge manifold (from Semi Gas Systems Inc.). These manifolds include many safety features, such as an emergency pneumatic shutoff valve which allows remote shutdown of process gas flow. A toxic gas monitor, capable of

(1)

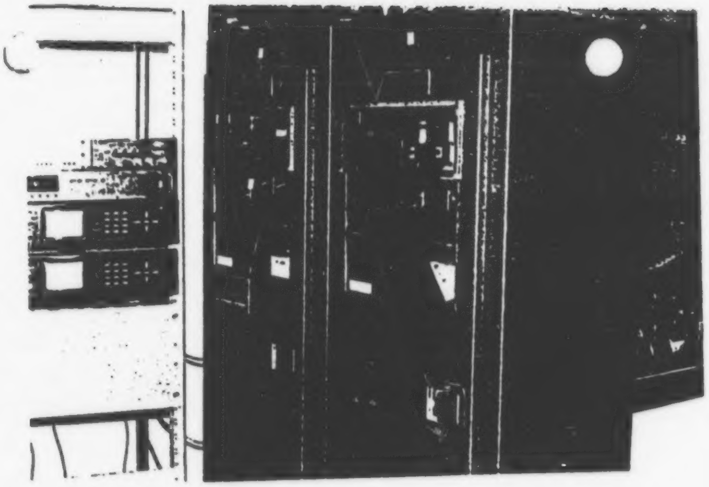

(2)

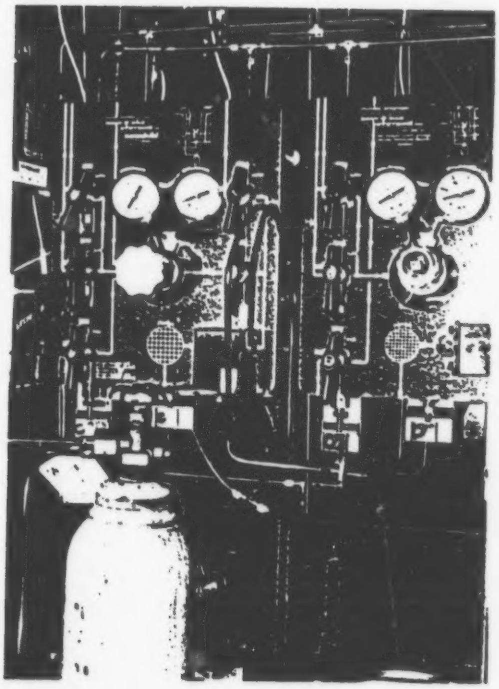

(3)

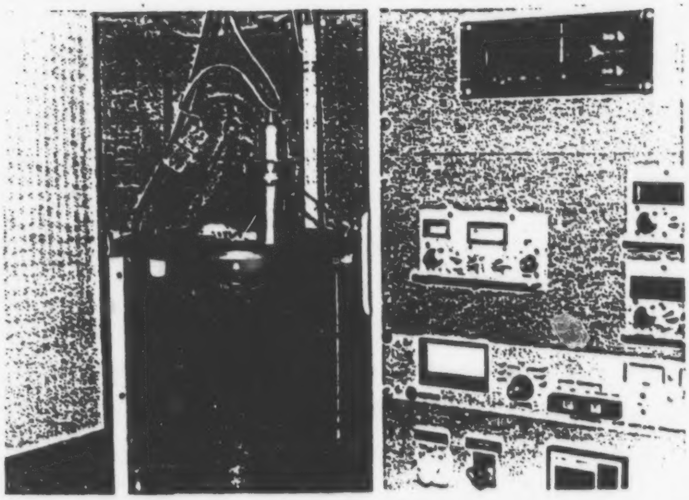

Figure 34

detecting both phosphine and diborane to levels below TLV (Threshold Limit Values) was installed and interconnected with the rest of the alarm system which provides automatic shutoff under any of the following potentially dangerous conditions:

(a) Failure of exhaust system, continuously detected through a pressure difference between the room and the exhaust duct.

(b) Fire or fire potential, continuously monitored by means of temperature sensor.

(c) Toxic gas line disruption. Any flow in excess of a preset limit will trigger shutoff.

(d) Any minimum presence (above 50 ppb) of any of the toxic gases inside the gas cabinet of near the reactor.

The gas lines include fine particulate filters (0.02 µm), mass flow controllers and pneumatically controlled, normally closed, bellow valves. All connections are Parker Vacu-Seal (equivalent to Cajon VCR).

The source of PH_3 is a bottle containing only phosphine. This is then mixed with SiH_4 and with a buffer gas such as Ar, as desired. Since B_2H_6 will react in the gas container, producing higher, explosive boranes, we use diborane in silane as the source. This has one disadvantage: the maximum percentage of B_2H_6 in the reactor is obviously that in the container. This was 0.1 % for all the experiments reported here. After passing through the reactor, any unreacted gas which reaches the mechanical pump is burned in a furnace with a quartz tube, at 1100°C. The gases are then relatively safe, and may be exhausted. In order to eliminate any residual B_2H_6 or PH_3 from the reactor, after a deposition, we installed an argon line with controlled flow, to purge the bell jar before opening, after deposition. In order to completely eliminate traces of B_2H_6, we have to purge approximately ten times before opening the system. One run consequently requires two days: one for deposition, and the second for purging.

7.2 Deposition

Plasma deposition was carried out in our radio frequency deposition chamber, under a feed gas flow rate of 25 sccm at a pressure of 200 mTorr. Deposition took place at a substrate temperature of 300°C, under a power dissipation of 6.5W. The feed gas used for B doping was SiH_4 containing 1000 ppm of B_2H_6.

Initial runs showed no evidence of doping, nor was B detected by XPS surface analysis. It was only on the fourth and subsequent runs that some doping was detected, leading us to suspect that it was necessary to precondition both the gas lines and the deposition chamber with the dopant prior to its incorporation into the depositing a-Si:H. We eventually obtained B-doped material having a conductivity of $\sim 8 \times 10^{-6}$ Siemens and an activation energy near 0.6 eV.

Table 10 shows typical values used in these depositions. High temperature activation energies as low as 0.35 eV were obtained. This is quite satisfactory.

We also began doping a:Si:H with P, using PH_3 as the dopant. Because this gas is stable to compression, it is available as the pure gas. This permits us to vary the ratio of feed gas components (SiH_4 and PH_3) over a wide range. Again, system preconditioning was found to be necessary. Subsequent to such preconditioning, we have thus far obtained samples with conductivities of about 2×10^{-4} Siemens and activation energies near 0.35 eV. Table 11 gives typical values used in these depositions.

Table 10 Conditions for Growth of Some Doped Samples with 0.1 % B_2H_6 in SiH_4

Flow rate (sccm)	Power (W)	T_s (°C)
16	6	300
16	6	300
16	6	300
25	20	300
25	40	300

Table 11: Conditions for Growth of Some n-doped Samples Flow Rate (sccm)

SiH_4	Ar	PH_3	Power (W)	T_s (°C)
9	10	0.76	40	300
9	10	0.76	40	300
9.0	10	0.2	40	300
9.0	10	0.1	40	300
9.0	10	0.36	40	300
9.9	4.0	0.36	40	300
9.0	10	0.36	40	300
9.0	4.0	0.76	10	300
9.0	4.0	0.36	10	300
9.0	4.0	0.20	6	195

The electrical properties of these samples were investigated. As discussed later, we obtained satisfactory reproducibility for samples with activation energies between 0.3 and 0.4 eV, and conductivities as high as 1.4×10^{-2} S/cm.

7.3 Studies of doping mechanisms

7.3.1 Effect of coordination (bond angles)

Mr. Lu has completed his experimental study of Ga implanted into a-Si and a-Si:H, and annealed. He finds that the Ga is initially in an elemental state or is 2-fold coordinated. Annealing produces three- and four-fold coordination, with the same activation energy for both. This energy agrees with that observed elsewhere for bond rearrangements. As a result, he proposes a new model for the doping mechanism, based on bond angles. This model is related to, but is quite distinct from, Street's model. We are in the process of publishing these results. Key extracts of his Ph.D. thesis appear in Appendix A.

7.3.2 Band bending

Mr. Bekkay has been studying the B- and P-doped samples whose preparation was discussed in the previous section. Using a recently developed theory [32, 33], he has shown the presence of band bending, a consequence of doping. The theory may be stated as follows: when surface states exist (due, e.g., to dangling bonds), these may capture electrons or holes from the dopant, forming an electrical double layer. One may show that the depletion depth, d, is

$$d = (2 \varepsilon \varepsilon_0 \phi_S / eN)^{1/2}$$

where ϵ and ϵ_0 are the dielectric constants of substrate and vacuum, ϕ_S is the surface potential caused by the band bending, e is the electronic charge and N is the volume concentration of dopant. Then, the potential in the space-charge region, $\phi(Z)$, is

$$\begin{aligned}\phi(Z) &= (eN/2\epsilon\epsilon_0)\ (Z-d)^2 \text{ when } Z<d \\ &= 0 \text{ when } Z>d\end{aligned}$$

where Z is the depth from the surface.

Now, the reduction in photoelectron signal, as obtained by XPS surface analysis, is

$$A(Z,\theta) = e^{-Z/\lambda \cos\theta}$$

where θ is the angle from the surface normal and λ is the electron mean free path. Defining $i(E,Z)$ as the energy distribution spectrum at binding energy E, the observed intensity as a function of angle, $I(E,\theta)$, is

$$I(E,\theta) = \int i(E,Z)\ e^{-Z/\lambda \cos\theta} dZ$$

In other words, band bending will cause changes in both intensity and energy as the angle is changed. An example is seen, in Figure 35, for P-doped a-Si:H deposited from a feed gas containing 4 % PH_3 (plus symbols), compared to intrinsic material (squares). Note that, while the binding energy is constant for the intrinsic material as a function of the angle θ, the Si 2s binding energy for the P-doped material decreases with increasing θ. This is a demonstration of the incorporation and ionization of P.

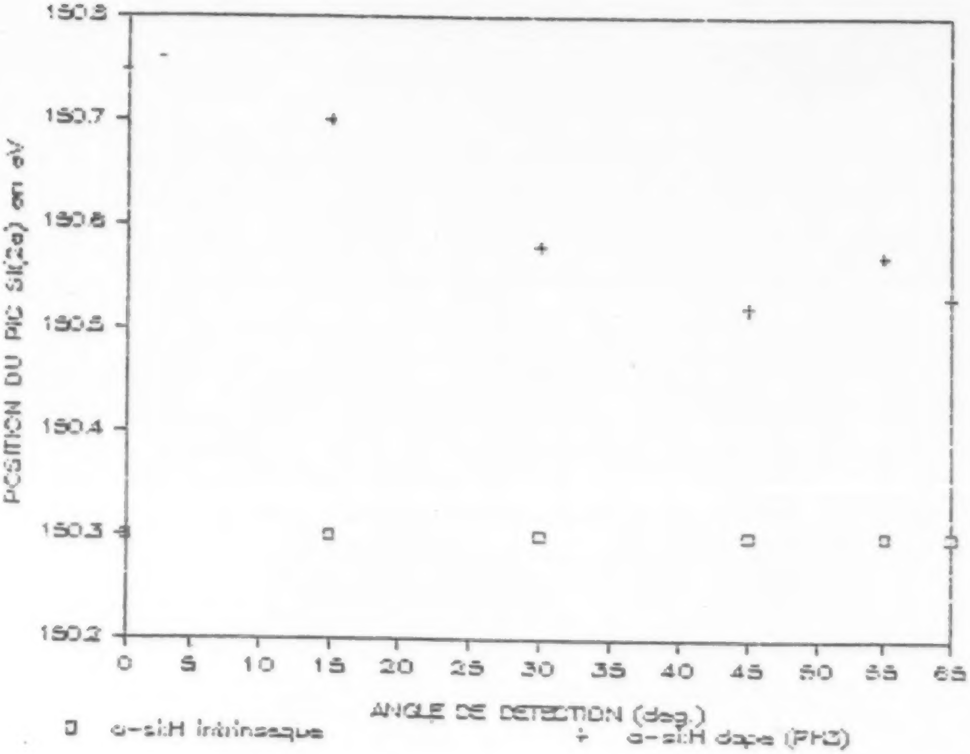

Figure 35 Effect of doping on band bending.

This has been confirmed by valence band XPS. As seen in Figure 36, the spectrum of the intrinsic material is substantially changed on doping. First the region near -10 eV, due to Si 3s electrons, has decreased noticeably and has shifted toward lower binding energy. Second, and more important, the P-doped sample (5 % PH_3) has a much gentler slope as it approaches the top of the valence band, near -1 eV; this is a clear demonstration of traps in the energy gap.

7.3.3 Fermi level shifts of P-doped a-Si:H

Amorphous hydrogenated Si was P-doped using PH_3, as previously described. The volume percent PH_3 in the feed gas ranged from 0-8.4 %. Samples were evaluated by Xray photoelectron spectroscopy. By measuring the binding energy (B.E.) of the Si 2s peak as a function of the volume percent PH_3, and using the C 1s peak at 285.0 eV at a reference, one could explore the shift in Fermi level, since $\Delta E_B = \Delta E_F$. These shifts were not linear in volume percent PH_3:

Volume % PH_3	ΔE_F
0	0
1	0
2.2	0.16
4	-0.18
5	0
8.4	0.32

It should by noted that our instrument is accurate to ± 0.02 eV, so the excursions at 2.2, 4 and 8.4 eV are real. Similar excursions, also showing a slight shift at ~ 2 % PH_3, a return at ~ 5 % PH_3 and a larger shift above 5 % PH_3, have previously been seen, both spectroscopically [34] and electrically (energy of activation) [35].

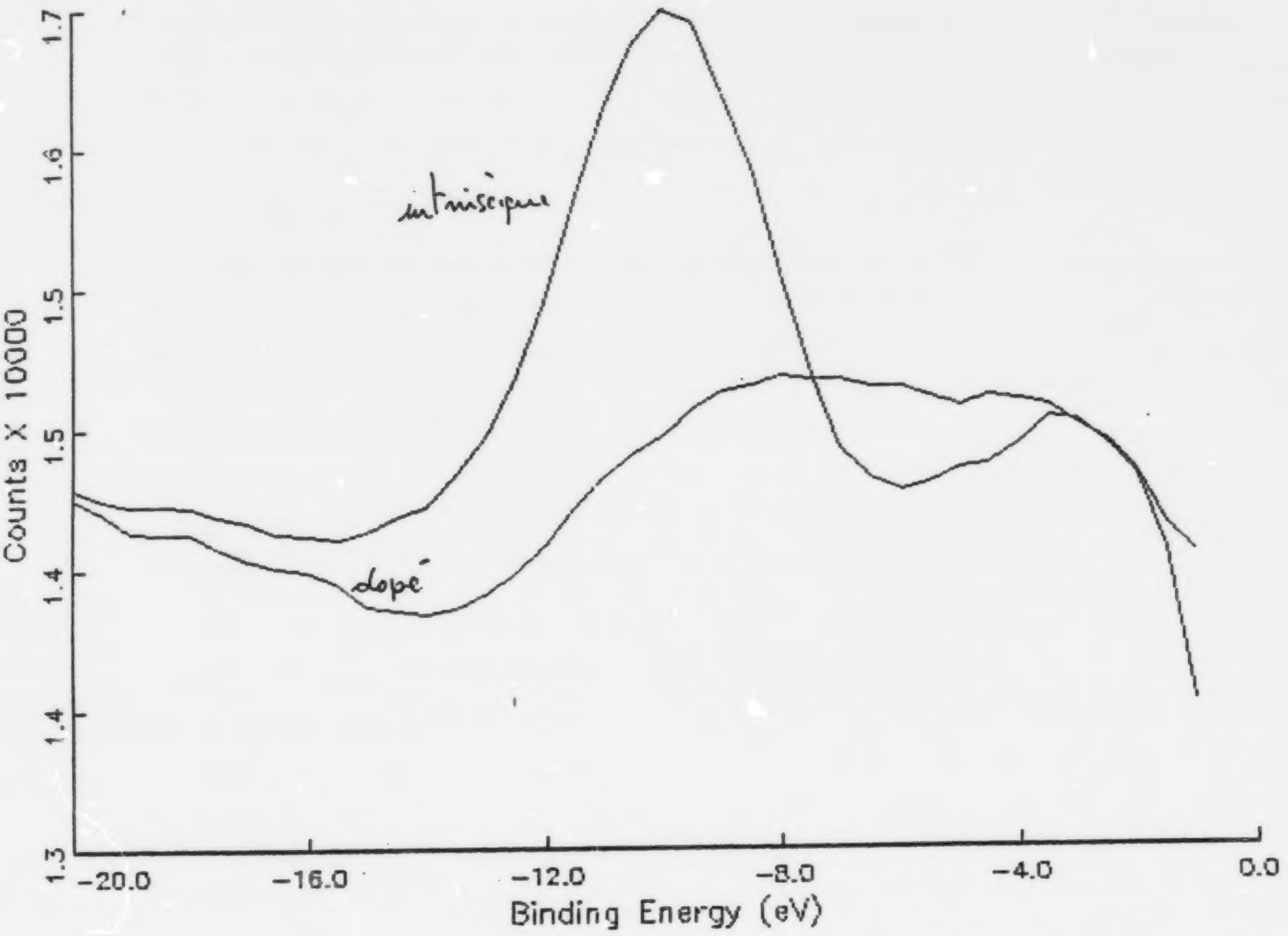

Figure 36 Valence band XPS spectra.

In order to understand this nonlinear behavior, one must quantitatively evaluate the P content and its chemical shift, both possible, in principle, by XPS. First, two problems must be overcome. The first of these problems is seen in Figure 37, a standard XPS spectrum of crystalline (and the essentially identical amorphous) Si. In the region between 100 and 150 eV, one finds several Si bulk plasmon peaks. This is also the region (~ 130 eV) where the P 2p multiplet is manifested (see Fig. 38). Thus, the first step is to extract the P spectrum.

Figure 39 shows an a-Si:H XPS spectrum (noise) in the P 2p region. Digital filtering of this spectrum gives the solid line. This is justified, a posteriori, by the presentation of the difference between these two spectra (not shown): it should consist of a featureless constant amplitude random noise spectrum across the entire energy range. Digital filtering makes use of the power spectrum of the data in Fig. 38, which differs slightly with the energy range taken. As a result, small features, such as those seen at 126 and 130 eV may have no meaning.

Figure 39 should be compared with Figure 40, where the sample contains P dopant, due to the 2 % PH_3 used. Note the new peak at ~ 129 eV, due to the P 2p multiplet. Figure 40 makes clear that the peak at 129 eV is, indeed, representative of P and that its chemical shift is to an energy slightly lower than that of bulk P. This indicates that P may be inducting electrons from the bulk Si matrix. Such behavior is eminently reasonable, since calculations [36] have shown that the te^2 $\underline{te}$ te te structure of P (where te = tetrahedral and the underline indicates the orbital under discussion) has an electronegativity of 2.78 on the Pauling scale while the $\underline{te}$ te te te structure of Si has an electronegativity of 2.23 on the same scale. Because the Si matrices of amorphous and crystalline Si differ little [37] (their coordination numbers are 3.8 and 4, respectively), P would be expected to act in a similar fashion in both materials.

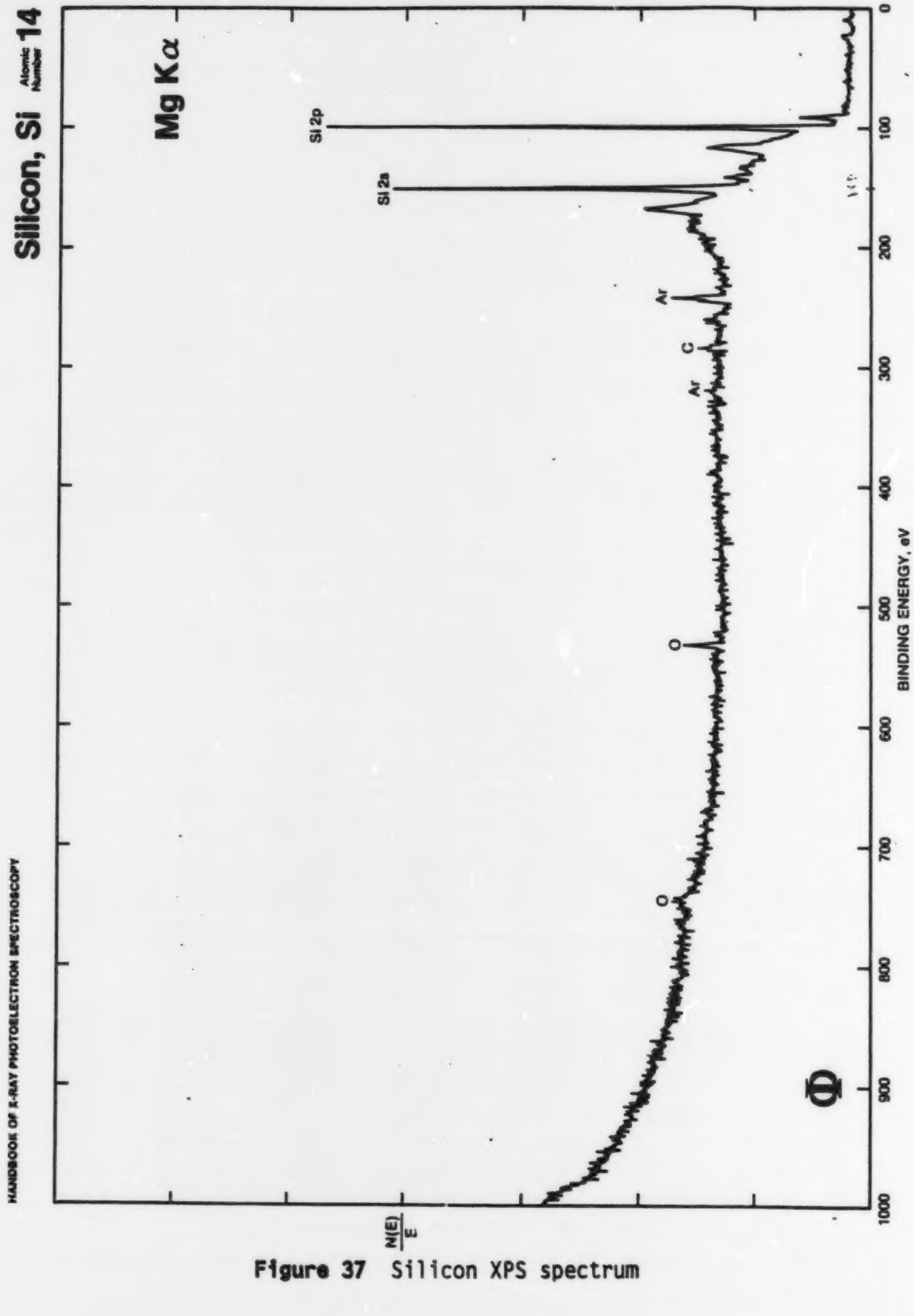

Figure 37 Silicon XPS spectrum

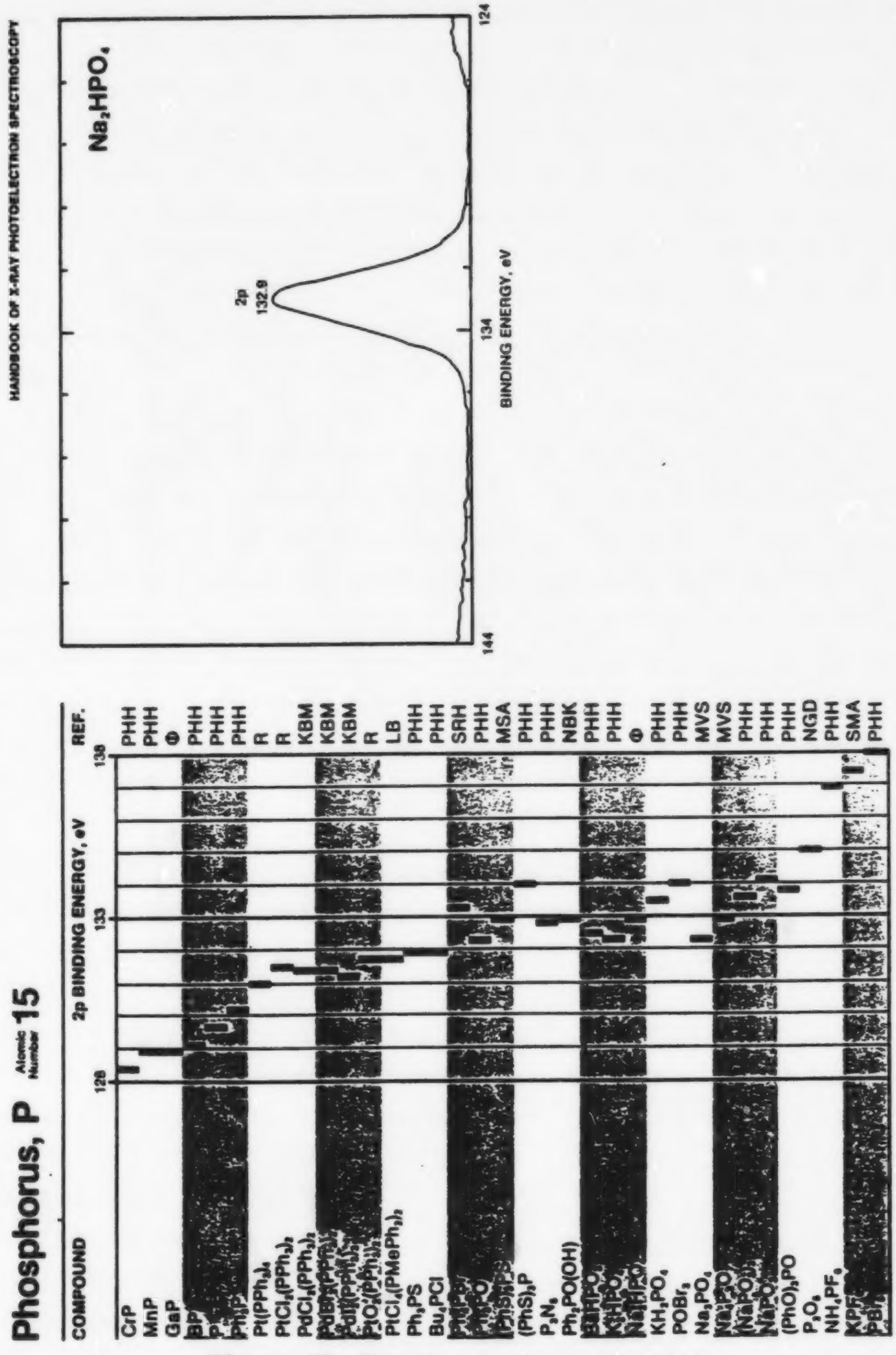

Figure 38 Phosphorus chemical shifts.

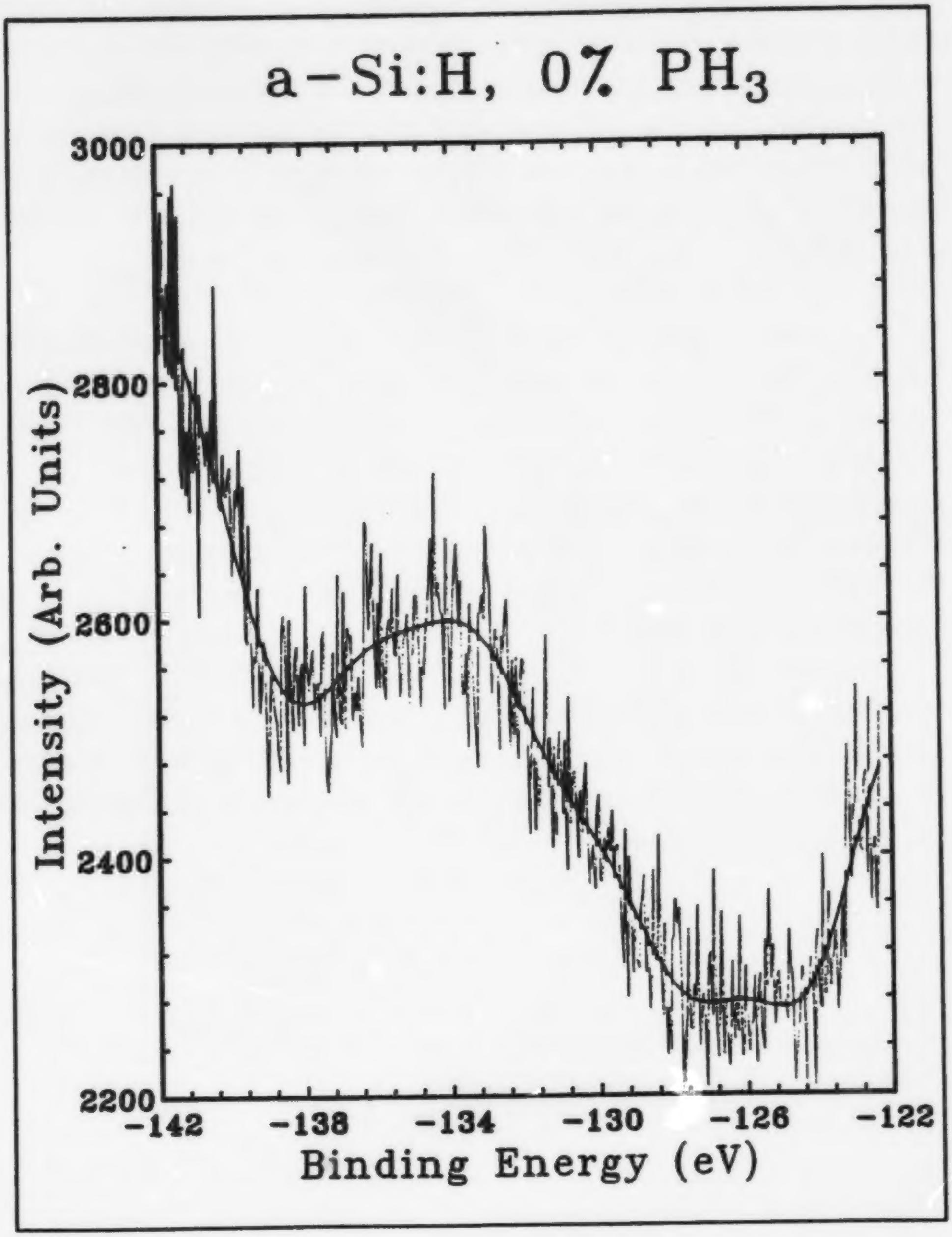

Figure 39 Plasmon region, showing noise and noiseless spectrum

However, it is clear that the P dopant in c-Si acts as a donor while XPS suggests that the P dopant in a-Si:H does not appear to donate its electrons. This is in clear contradistinction to the ΔE_F evidence cited earlier, which indicates electron donation. It may be that the bulk of the incorporated P does not act as a donor and that a small concentration, too small to be detected in our case, actually dopes. It may also be that the P donates its electrons to an atom other than Si.

The P 2p region is seen in Figure 41 as a function of concentration. While the main peak, at ~ 129 eV, does not shift with increasing PH_3 concentration, there is a hint of a peak near 131 eV for the 8.4% PH_3 case. As indicated earlier, this may not be real. However, if it were, and this is presently being pursued, it would give evidence for a small concentration of P more positively charged than the majority of the P. Such a positive charge indicates electron donation.

Another finding seen in Fig. 41 is that P does not seem to have been incorporated at 5 % PH_3. While this helps to explain the ΔE_F data, the reason is presently unknown. Clearly, several factors contribute to the doping.

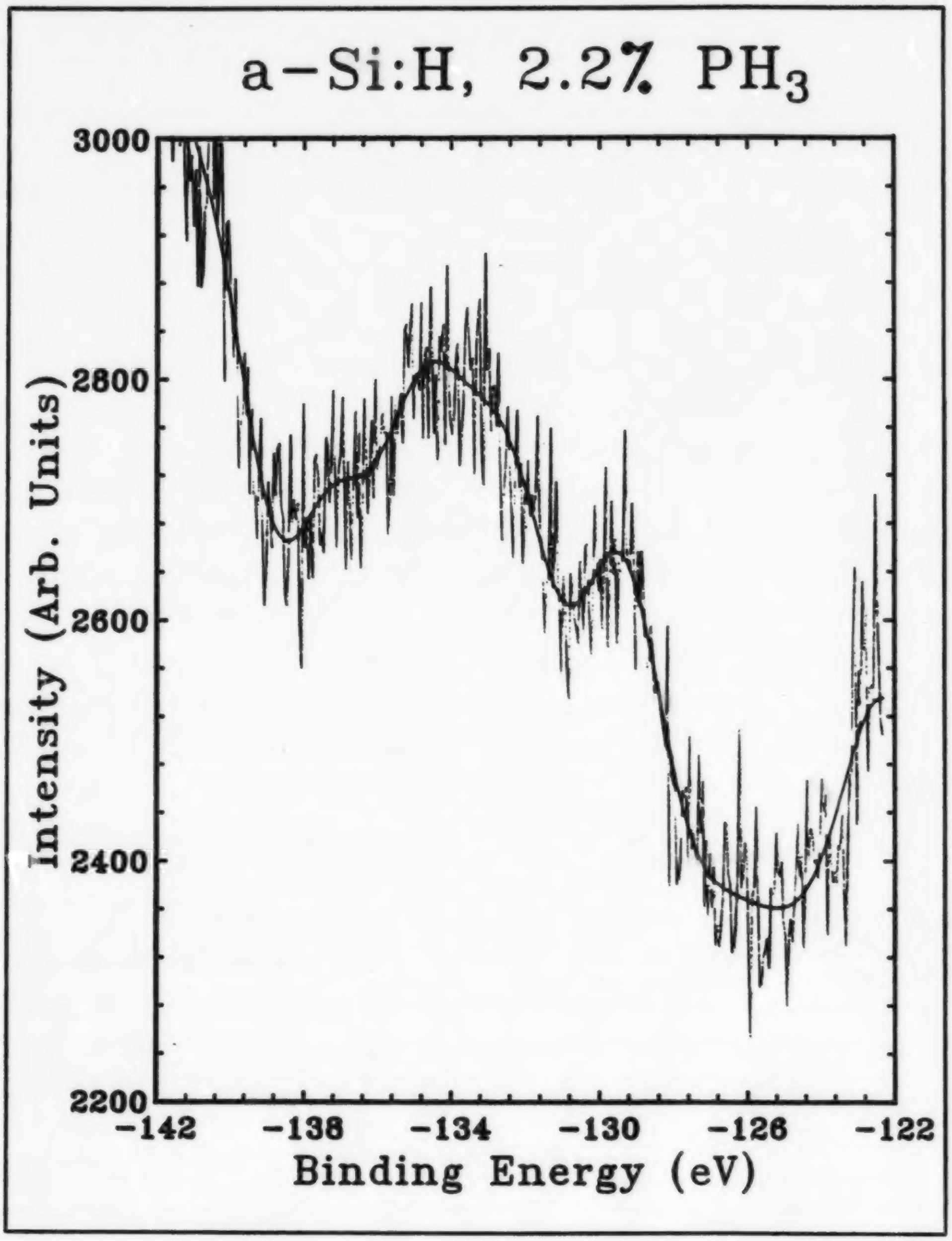

Figure 40 Plasmon region, showing P 2p multiplet at 130 eV.

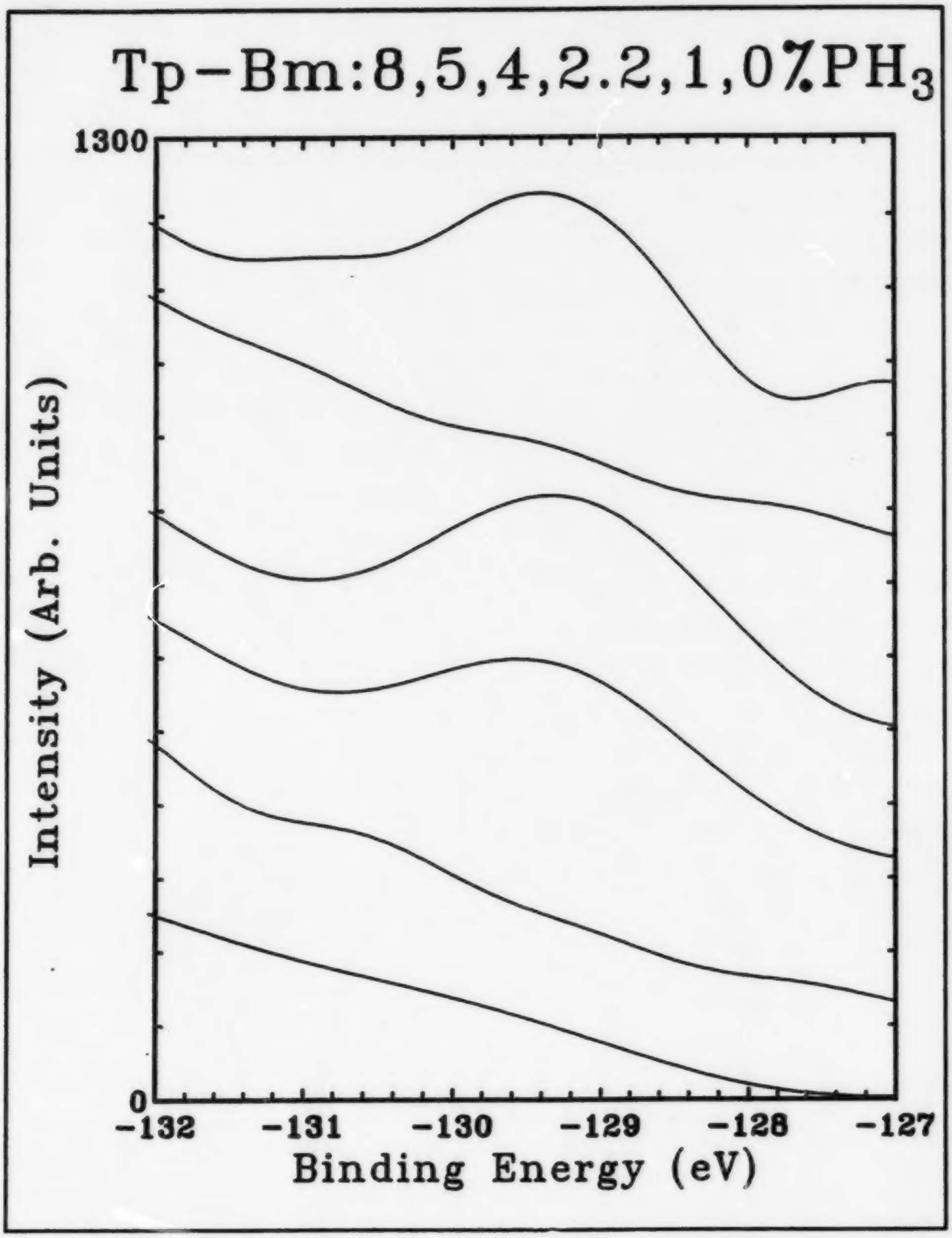

Figure 41 Phosphorus XPS spectrum as a function of concentration of PH_3. From bottom to top, the concentrations are 0, 1, 2.2, 4, 5 and 8.4 % PH_3

7.4 Electrical Characterization of Amorphous Silicon

Several series of electrical measurements have been made in order to characterize the quality and the doping efficiency of both undoped and doped a-Si:H used to form the solar cells. These measurements were in addition to the analysis of the photoresponse of the cells which was used to determine cell efficiencies.

Two principal techniques were employed. The first was the measurement of the d.c. current-voltage characteristics (I-V-T) at various temperatures using a coplanar electrode geometry with millimeter spacing. Hence, the conductivity of the entire thickness of the film was measured rather than the response of the barrier region around the electrode. The variation with temperature leads to the activation energy of the charge carriers. The second technique, measured on selected samples, was a frequency response analysis (FRA) from 10^{-3} Hertz to 10^{+4} Hertz as a function of applied voltage. Since this technique is an a.c. measurement, it provides information on the conductivity as well as the capacitance of the space charge region. Both experimental systems operate under microcomputer control.

These techniques proved to be complementary in the characterization of the materials studied. For the undoped material, the FRA analysis was more sensitive than the I-V one, particularly for the sandwich geometry of the solar cell. For the doped material, the I-V-T measurements in a planar configuration provided the clearest data.

7.4.1 I-V-T Current versus voltage measurements for gas-phase doped samples

As shown in Figure 42, samples for I-V-T analysis are mounted in a temperature-controlled sample chamber closed to light input. Detailed I-V curves at each temperature are analyzed for the conductivity; the slope of the Arrhenius plot of ln (conductivity) versus 1/T gives the activation energy directly. Such data are used to construct Arrhenius plots; these plots are invariably curved above room temperature, characteristic of both the undoped and the doped samples. It indicates the presence of states in the mobility gap region which contribute to the conduction process at and below room temperature. In general, this contribution is relatively less important the more heavily doped the sample.

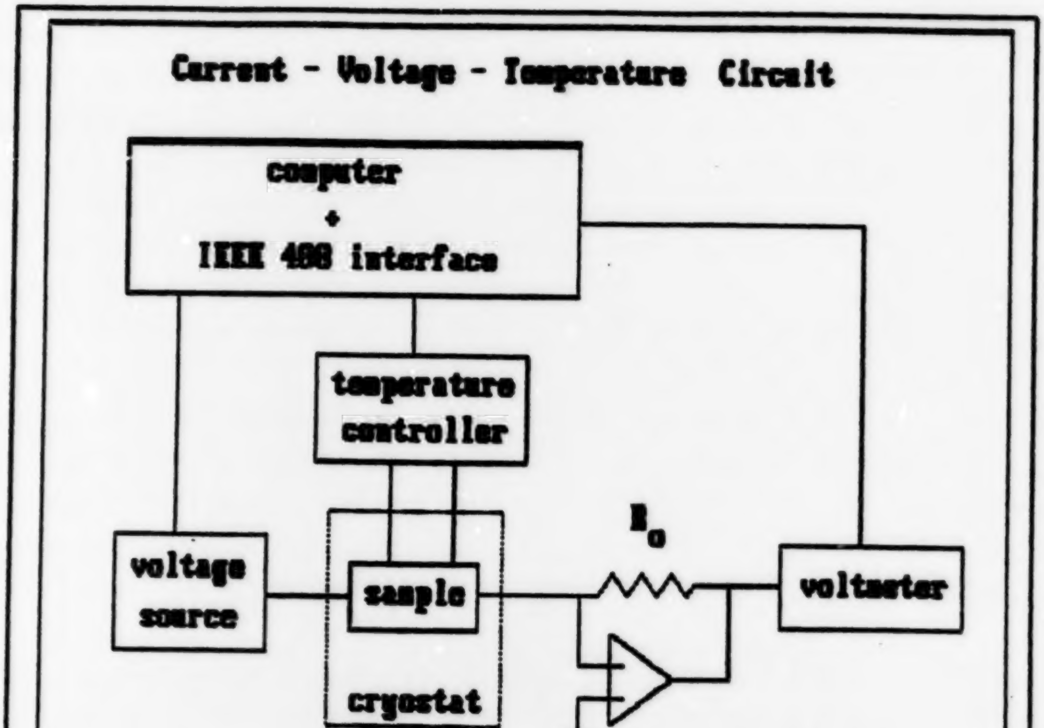
Current - Voltage - Temperature Circuit
computer
+
IEEE 488 interface
temperature
controller
voltage
source
sample
cryostat
R$_o$
voltmeter

Figure 42 Schematic diagram of current-voltage-temperature apparatus

Conductivity data for the samples studied are listed in Table 12; the principal preparation parameters are also included. Several conclusions can be made:

1. Active doping with phosphine (n-doping) has been obtained up to the point of saturation. For PH_3 concentrations above 1 % the room temperature conductivity saturates around 2 x 10^{-4} $(\text{ohm-cm})^{-1}$; at 170°C it has risen to 2 x 10^{-2} $(\text{ohm-cm})^{-1}$.

2. Although the RF power level during sample preparation may have an effect on the growth rate of the cells, it has little apparent effect on the conductivity, i.e. the doping level.

3. However, the temperature of the depositing film has a clear effect. The material deposited at 180°C gives a conductivity characteristic of undoped a-Si:H and that at 195°C shows a lower doping than the films deposited at 300°C.

4. The films doped to saturation show little thermal hysteresis and are quite reproducible from sample to sample.

5. Doping with diborane (p-doping) is relatively inefficient. Since the diborane concentration was fixed by the gas mixture, this lack of effective doping may be an indication that the saturation regime has not as yet been attained.

6. Generally, the activation energies for the n-doped samples rise to about 0.3 eV at saturation doping. They decrease slightly with thermal cycling to 180°C. For p-doping the variation of the activation energy is much greater on heating to 180°C indicating an activation of part of the boron incorporated. The changes in conductivity are correspondingly important.

Table 12 Sample Data

Dopant type	Dopant (gas) (%)	Dep. temp. (C)	Cond. S/cm (@RT)	Cond. S/cm (@ 170°)	High temp. activ. energy (eV)
Boron	0.1	300	3.6E-7	4.1E-5	0.52
Boron	0.1	300	4.4E-8	3.7E-5	0.67
Boron	0.1	300	5.6E-6	2.0E-4	0.35
Boron	0.1	300	5.3E-6	2.1E-4	0.39
Boron	0.1	300	5.9E-6	2.2E-4	0.37
Phos.	3.8	300	1.0E-4	7.3E-3	0.40
Phos.		300	1.6E-4	8.0E-3	0.38
Phos.	1.9	300	4.0E-4	1.4E-2	0.35
Phos.		300	1.2E-4	5.0E-3	0.35
Phos.	0.5	300	9.6E-5	6.3E-3	0.39
Phos.	1.9	300	1.2E-4	6.6E-3	0.36
Phos.	2.7	300	1.6E-4	7.6E-3	0.38
Phos.	1.9	300	2.8E-4	1.4E-2	0.38
Phos.	5.5 2.7	300	1.6E-4	9.3E-3	0.37
Phos.	2.2	195	1.6E-8	4.7E-7	0.33
Phos.		180	4.2E-6	1.3E-3	0.30
Phos.	7.8	300	1.7E-3	7.1E-2	0.37
Phos.		300	2.2E-4	1.0E-2	0.38

It can be concluded that both n- and p-doping have been achieved through gas-phase inclusion of phosphorus or boron into a-Si:H samples. Doping levels up to saturation can be controlled by the partial pressure of the doping gas in the plasma reactor. Hence, p-i-n structures are possible with the present system by control of the feed gas.

7.4.2 FRA: A.C. impedance measurements for intrinsic a-Si:H prepared by simultaneous RF and microwave irradiation

The details of the frequency reponse analysis setup are quite similar to the I-V-T system except that an A.C. modulation is surperimposed on the D.C. polarization of the sample and the in-phase and quadrature A.C. responses of the sample are measured. States in the mobility gap region give rise to steps in the capacitance and peaks in the conductance; these features are activated with temperature with energies in the range of 0.3 to 0.7 eV.

These samples show intrinsic a-Si:H behaviour with features similar to those found for single frequency RF-plasma films. On the basis of these data the double frequency material appears to be a promising intrinsic material for solar cell application.

8. CONCLUSIONS

We have demonstrated that the quality of the a-Si:H produced in our laboratory is the equivalent of the best produced anywhere else. Further, an innovation developed in our laboratory, dual mode frequency deposition, has been shown to be a potential method for the high rate (~ 20 - 30 A/sec) deposition fo a-Si:H having conductivity ratios (σ_{ph}/σ_d) of the order of the highest quality material (~ 20 - 40 x 10^3), previously thought to be producible only at low deposition rates (~ 3 A/sec).

The cosputtering of metal into the plasma from which the a-Si:H is deposited, a potentially attractive method of doping, has been investigated. Although doping has been demonstrated, it has been found to be self-limiting. These limitations include the agglomeration of unreacted, excess metal and the introduction of a large number of traps. Their exploration, and eventual elimination through a change in deposition parameters, must await further study.

We have successfully doped a-Si:H by adding gas phase dopant (i.e., B_2H_6 and PH_3) to the plasma. While the optimization of this technique awaits a continuation of funding, we have made significant progress in understanding the doping mechanism and the effect of dopant on the film surface. This latter subject is extremely important to the commercialization of doped a-Si:H solar cells because it bears on atmospheric contamination and electrode reactions.

REFERENCES

[1] J. Mort and F. Jansen eds, Plasma Deposited Thin Films, CRC Press, Boca Raton 1986.

[2] P. Capezzuto and G. Bruno., Pure Appl. Chem., 60 (1988) 633.

[3] K. Tachiibana. Pure Appl. Chem., 60 (1988) 769.

[4] F. Jansen, p. 1 in ref. 1.

[5] M. Hirose, p. 21 in ref. 1.

[6] M.R. Wertheiimer, M. Moisan, J.E. Klemberg-Sapieha and R. Claude. Pure Appl. Chem., 60 (1988) 815.

[7] M.R. Wertheimer and M. Moisan. J. Vac. Sci. Technol. A, 3 (1985) 2643.

[8] L. Martinu, J.E. Klemberg-Sapieha and M.R. Wertheimer. Appl. Phys. Lett., 54 (1989) 2645.

[9] B. Chapman. Glow Discharge Processes, Wiley-Interscience, New York 1980.

[10] R. Messier, A.D. Giri and R.A. Roy. J. Vac. Sci. Technol. A, 2 (1984) 500.

[11] J.L. Brebner et al., Can. J. Phys., 63, 786 (1985).

[12] R.G. Bosisio, M.R. Wertheimer and C.F. Weissfloch. J. Phys. E., 6, 628 (1973).

[13] D. Masson, L. Paquin, S. Poulin-Dandurand, E. Sacher and A. Yelon, J. Non-Cryst. Solids, 66, 93 (1984).

[14] D. Masson, E. Sacher and A. Yelon, Phys. Rev. B, 35, 1260 (1987).

[15] M.H. Brodsky, M. Cardona and J.J. Cuomo, Phys. Rev. B, 16, 3356 (1977).

[16] E. Sacher, Phil. Mag. B, 51, 285 (1985).

[17] E. Sacher, Phil. Mag. B, 51, 295 (1985).

[18] See, e.g., A.H. Mahan, P. Raboisson, D.L. Williamson and R. Tsu, Paper presented at SERI PV ARGD Conference, Denver, May 13-15, 1986.

[19] J.C. Knights, G. Lucovsky and R.J. Nemanich, Phil. Mag. B, 37, 467 (1978).

[20] L. Ley, J. Reichardt and R.L. Johnson, Phys. Rev. Lett., 22, 1664 (1982).

[21] See, e.g., J. Robertson. Phys. Rev. B, 31, 3817 (1985).

[22] R. West and T.J. Baron. J. Chem. Educ., 57, 334 (1980).

[23] J.L. Brebner, R.W. Cochrane, R. Groleau, S. Gujrathi, D. Kérouak, Y. Lépine, J.P. Martin, M. Vanacek, C. Aktik, M. Aktik, A. Azelmad, J.F. Currie, S. Poulin-Dandurand, B. Ranchoux, E. Sacher, C. Tannous, M.,R. Wertheimer, and A. Yelon, Can. J. Phys., 63, 786 (1985).

[24] M. Toulemonde, P. Siffert, A. Deneuville and J.C. Bruyère, Appl. Phys. Lett., 39, 152 (1981).

[25] C. Brassard, R. Groleau, J. L'Ecuyer, J.P. Martin, J.F. Currie, P. Depelsenaire, M. Wertheimer, and A. Yelon, J. Phys., 42, Colloque C4, 795 (1981).

[26] G. Müller, F. Demond, S. Kalbitzer, H. Damjanschitsch, H. Mannsoerber, W.E. Spear, P. Le Comber and R.A. Gibson, Phil. Mag. B, 41, 571 (1980).

[27] P.C. Schmidt and M.C. Böhn, Ber. Bunsenges. Phys. Chem., 87, 925 (1983).

[28] R.G. Hart and C.B. Cooper, Surf. Sci., 94, 105 (1980).

[29] H. Oechsner, Z. Phys., 238 433 (1980).

[30] J. Currie, P. Depelsenaire, R. Groleau and E. Sacher, J. Colloid Interface Sci., 97, 410 (1984).

[31] See, e.g., C. Calandra, O. Bisi and G. Ottaviani, Surf. Sci. Rept. 4, 271 (1984).

[32] T. Ogama. J. Appl. Phys., 64, 753 (1988).

[33] W.M. Lau, J. Appl. Phys.. 65, 2047 (1989).

[34] B. van Roedern, L. Ley, M. Cardona and F.W. Smith, Phil. Mag. B, 40, 433 (1979).

[35] R.H. Williams, R.R. Varma, W.E. Spear and P.G. LeComber, J. Phys. C: Solid State Phys., 12, L 209 (1979).

[36] D. Bergmann and J. Hinze, in "Electronegativity", edited by K.D. Sen and C.K. Jorgensen, Springer-Verlag, New York, 1987, p. 145.

[37] S.R. Elliot, Adv. Phys., 38, (1989).

APPENDIX A

Key extracts of Z. Lu's Ph.D. thesis on the fundamental doping mechanisms in a-Si:H

Chapter 4

Results and Discussion

4.1 Structural Relaxation and Crystallization of Amorphous Silicon Studied by Photoemission VB Spectroscopy

In Fig. 4.1. we show the photoemission valence band (VB) density of states (DOS) spectra obtained from crystalline Si(100) and GD a-Si:H samples. The valence band maxima of the spectra are set at the zero binding energy position. The valence electron density of states N_v is shown in an arbitary scale. The inelastically scattered electron background of the spectra were removed using the method developed by Shirley(1976).

The four valence electrons of Si atoms are distributed among three peaks in the VB-DOS in such a way that the area under peak I corresponds to 2 electrons. and the areas under peaks II and III to one electron per Si atom each. States at the top of the valence bands are predominantly 3p-like and those at the bottom (peaks II and III) mainly of 3s character (Ley. 1984b. Bose et al. 1988).

Peaks II and III in the DOS of c-Si are related to the presence of sixfold rings in the diamond structure (Weaire and Thorpe.1971: Joannopoulos and Cohen. 1976).

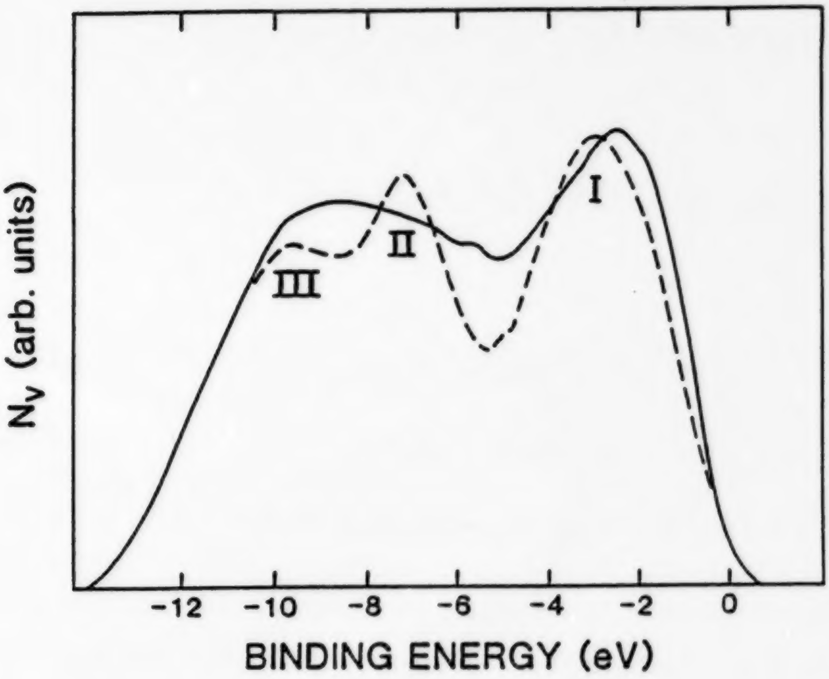

Figure 4.1: Experimental VB-DOSs of c-Si and a-Si:H derived from photoemission spectra. —— a-Si:H; - - - - c-Si.

In models of the amorphous network. topological freedom of the atoms allows for five, seven. and perhaps eightfold rings while preserving the tetrahedral units. The most common five-fold rings. for example. can be formed with only a slight adjustment of the tetrahedral bond angle. It has been suggested by Weaire and Thorpe (1971) that five-fold rings should introduce states between those of peaks II and III and thereby fill the gap. This conjecture has been confirmed by a series of calculations(Joannopoulos and Cohen. 1976: Ortenburger et al. 1972; Ching et al. 1976. 1977). Therefore. the featureless appearance of the lower portion of the amorphous silicon DOS is due to an averaging of a variety of local bonding topologies.

The centroids of the 3p-like bands of states (peak I) of both c-Si and a-Si:H were determined by a curve-fitting method. with an accuracy of 0.1 eV. We find that the the centroid for a-Si:H has been shifted. compared to c-Si. by 0.4 eV towards the VBM. The same amount of shift has also been reported by Ley et al (1972). From their calculations. Joannopoulos and Cohen (1976) have concluded that the shift of peak I is due largely to bond-angle variations in the amorphous silicon continous random network (CRN).

In Fig. 4.3. we show the variations of VB-DOSs of Ga$^+$ ion-implanted a-Si:H with post-annealing at temperatures from 250 °C to 350 °C. We found that the 3s-like band density of states (peaks II and III) of samples annealed at 250 and 300 °C still form a simple hump. basically the same structure feature as observed on unimplanted a-Si:H except for a higher electron density of states at about 10 eV energy on the ion-implanted and annealed samples. The 'extra' density of states at about 10 eV energy is interpreted as being due to the contribution of implanted Ga. This will be discussed in the next section. Peaks II and III in the VB become distinct after an anneal at 350 °C. We attribute this to structural relaxation of the silicon CRN. which results in a more ordered silicon lattice and thereby reduces the density of states between Peaks II and III. This agrees with the measurement of ΔE_{3p}, the centroid energy shift of the 3p-like band of states. The ΔE_{3p} measurement will be presented below.

Samples of a-Si:H thin film stripped off the c-Si substrates at annealing temperature ≥ 400 °C. This may be due to crystallization of the amorphous silicon network, which is accompanied by strain release and changes in the film density. Studies of reconstruction of the damaged silicon lattice and of the dopant activation process at higher post-annealing temperatures (≥ 400 °C) were, therefore, carried out only on c-Si samples. The valence electron energy distribution curves (EDCs) of Ga^+ ion-implanted c-Si are shown in Fig.4.3 as a function of annealing temperature. From the figure, we see that the general feature of the VB-DOS of a c-Si sample implanted and annealed at 300 °C is similar to that of amorphous silicon, as discussed above. However, typical crystalline silicon VB-DOS features are found for all valence electron spectra obtained on samples annealed at temperatures ≥ 400°C. The centroid of the 3p-like band of states of these samples is also found at the same energy as that of unimplanted c-Si(see details below). LEED was used to examine the crystallinity of the sample surfaces. Diffraction spots can only be observed on samples annealed at temperatures ≥ 500 °C. We thus conclude that the damaged silicon crystallizes at annealing temperature ≥ 500 °C. The two distinct 3s-like peaks observed for samples annealed at 400 °C indicate that the silicon CRN is subject to a structural relaxation process prior to crystallization.

As discussed above, the energy location of the centroid of the 3p-like band is one of the characteristic parameters distinguishing the valence electron distributions of the Si crystalline lattice and the amorphous CRN. Values of ΔE_{3p}, the centroid energy shift of the ion-implanted and annealed c-Si and a-Si:H samples (compared to unimplanted c-Si) are given in Table 4.1. From the table, we can see that the binding energies of virgin a-Si:H, as implanted a-Si:H and c-Si, and implanted a-Si:H and c-Si samples annealed at temperatures ≤ 300 °C are all the

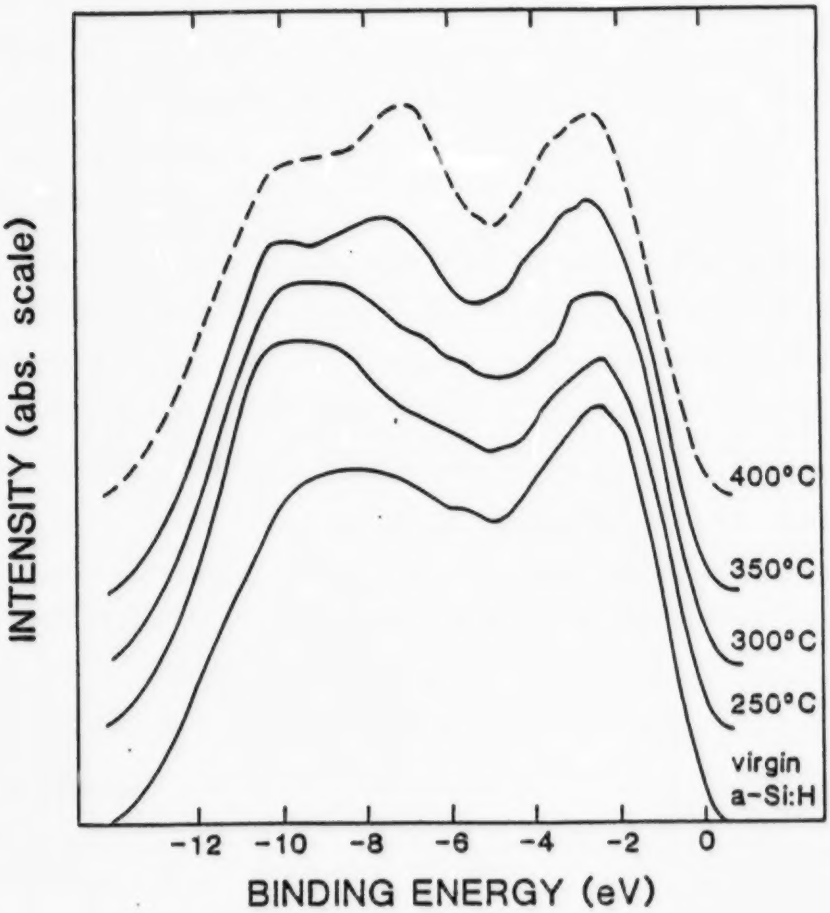

Figure 4.2: VB-DOS of Ga ion-implanted and annealed a-Si:H. The dashed curve is obtained on a c-Si sample.

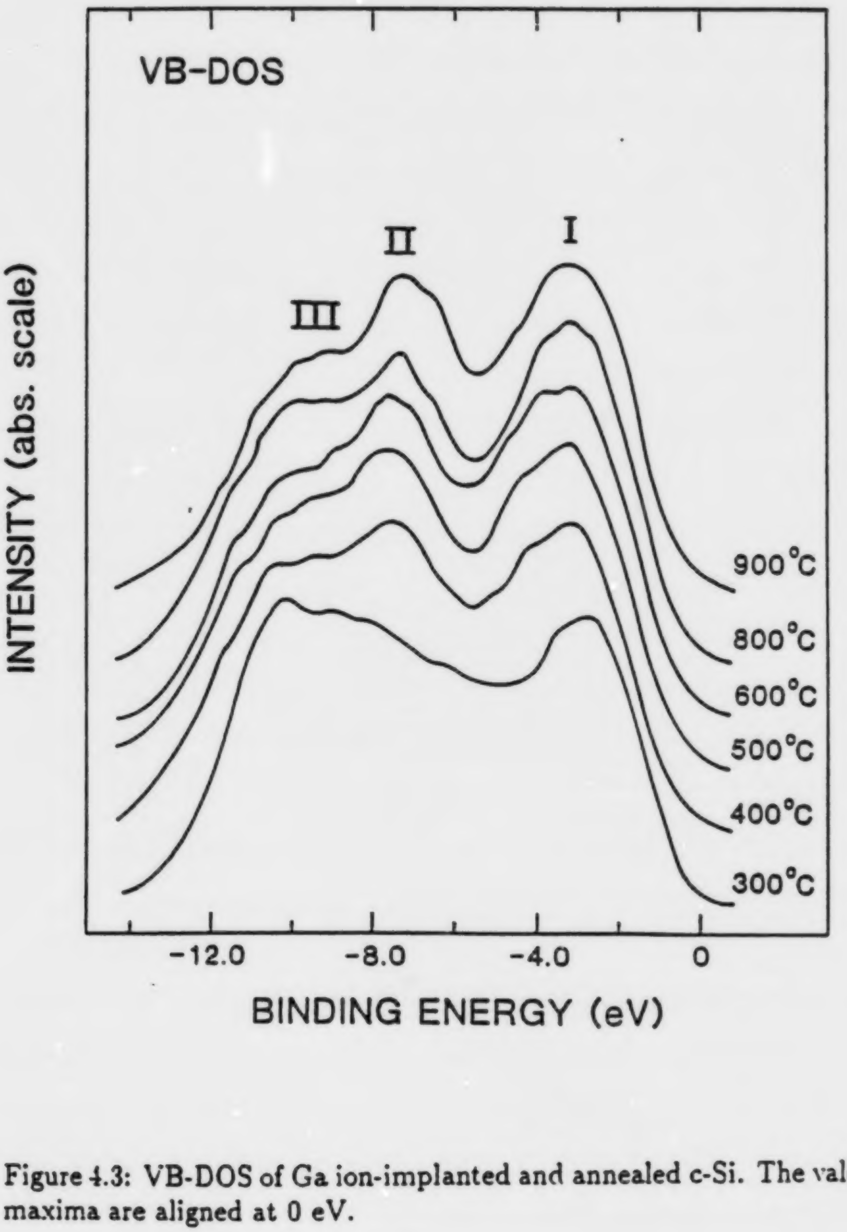

Figure 4.3: VB-DOS of Ga ion-implanted and annealed c-Si. The valence band maxima are aligned at 0 eV.

same. The centroid of the 3p-like peak of all these samples is shifted towards the top of the valence bands by 0.4 ± 0.1 eV. compared to virgin c-Si. For samples annealed at 350 °C, ΔE_{3p} is reduced to 0.1 eV. After an anneal at temperatures ≥ 400 °C, it is reduced to zero. This again suggests that the damaged silicon crystallizes at annealing temperatures ≥ 500 °C. and that the silicon CRN undergoes a structural relaxation or bond-angle ordering prior to crystallization.

From Raman scattering and neutron-diffraction studies, Fortner and Lannin (1988, 1989) also concluded that Ar^+ ion amorphised Si and Ge lattices transformed to a more ordered structure by way of structural relaxation upon annealing. $\Delta\theta$, the average Si-Si bond-angle variation or the width of Si CRN bond-angle distribution function $P(\theta)$. was found to decrease about 2° (Fortner and Lannin 1988 and 1989) for ion-amorphized Si and Ge upon annealing at 350 °C. The bond-angle deviation stored elastic potential energy release. which is brought about by structural relaxation or bond-angle ordering. was also measured on ion-implanted Ge (Donovan et al. 1985) and more recently on ion-implanted Si (Roorda et al 1989, Jacobson et al 1989) by differential scanning calorimetry (DSC) experiments. Structural relaxation and lattice ordering prior to crystallization. were also studied on low temperature deposited and post-annealed a-Si and a-Ge CRN using Raman scattering and extended X-ray-absorption fine-structure (EXAFS) experiments (Paesler et al 1983 and Tsu et al 1984).

4.2 VB-DOS Variations with Ga Atomic Orbital Hybridization

One interesting feature of VB-DOS of Ga ion-implanted Si is that there is a significant increase in the density of states at the bottom of the VB at an energy ~ 10 eV, as shown in the EDCs of Fig. 4.2 and 4.3. This can be more easily seen in Figure 4.4. where we have aligned the 3p-like band density of states N_v to

Table 4.1: ΔE_{3p} as a function of annealing temperatures.

TEMPERATURE (°C)	500	400	350	300	250	as-implanted	virgin
ΔE_{3p} (eV) (a-Si:H)			0.1	0.4	0.4	0.4	0.4
ΔE_{3p} (eV) (c-Si)	0.0	0.0		0.4		0.4	0(reference)

the same value. This clarifies changes in density of states in the 3s-like. peak-III. region.

We believe that the 'extra' density-of-states in this region is due principally to the two 4s electrons of unactivated. free. or elementary gallium Ga^{o}. The binding energy of the $Ga^{o}4s^{2}$ electrons is 11.55 eV (see Table 4.2) , roughly the same energy at which we found an increased density of states. The 4p electrons of Ga^{o}. have a binding energy of 5.67 eV. The $Ga^{o}4p^{1}$ electron, however, did not produce any significant features in the EDCs shown in Fig. 4.4. This may be due to the 4p electron of Ga atom having a lower photo-electric cross section than the 4s electron. as shown in Fig. 2.3. In addition. the Ga 4p orbitals are only half filled.

We shall show in the following section that the valence electrons $4s^{2}4p^{1}$ of Ga atoms are promoted to either an sp^{2} or an sp^{3} hybrid with increasing annealing temperature. This corresponds to a decrease in free gallium valence electrons. and consequently a decrease in the density of states in the region of peak III. as shown in the figure. The Ga atoms also diffuse upon annealing (the change in Ga concentration will be discused in later sections).

We are unable to identify any additional density of states contributed by newly created sp^{2} and sp^{3} Si-Ga bonding states in the EDCs of Fig. 4.4. This may be because the number of hybridized Ga is small at annealing temperature at or below 400 °C(see Section 4.4). For samples annealed at 500 °C. however. 10 at.% tetrahedral sp^{3} Ga has been found in the Si matrix through measurements of the Si2p core level(see section 4.6). The supersaturated tetrahedral Si-Ga bonding state . however, does not produce a distinct feature in the EDCs. Although there is no quantum chemical or energy band calculations of our specific case available at the time of writing. we believe that the energy distributions of the electrons at Si-Si and Si-Ga bonds should be similar because both of them are described by a non-localized Bloch wave function in a periodical Si lattice arrangement. An increase in the absolute value of the VB density of states. however. would

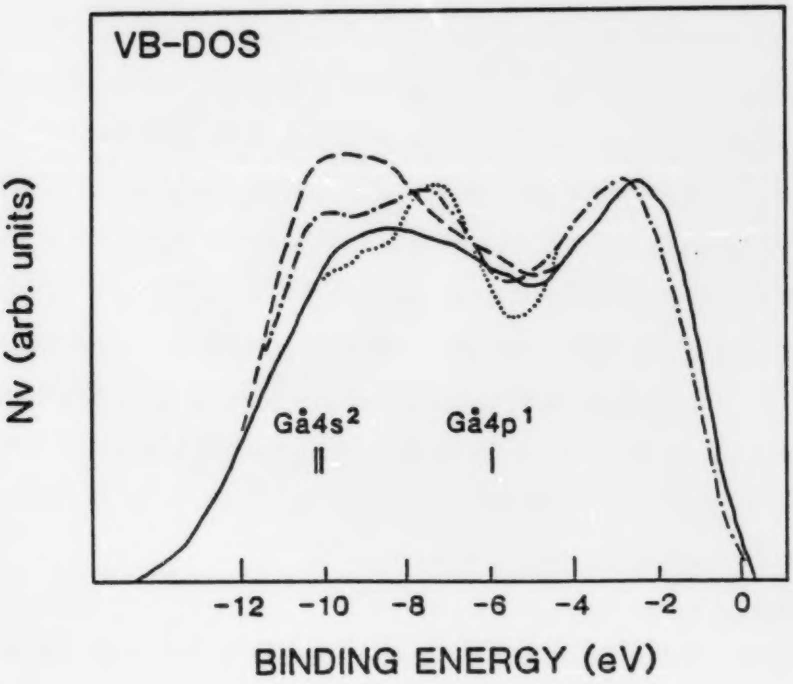

Figure 4.4: VB-DOSs of virgin a-Si:H, ——; Ga ion-implanted and annealed at 250 °C, - - - -, and 350 °C, - · - · - · -; Ga ion-implanted c-Si annealed at 500 °C, ······.

Table 4.2: Hartree-Fock s- and p-orbital energies in eV(Harrison 1981).

	Si	B	Al	Ga	In	Tℓ
$-E(s)$	14.79	13.46	10.70	11.55	10.14	9.82
$-E(p)$	7.58	8.43	5.71	5.67	5.37	5.23
$-E(s^2p^1)$[a]	12.39	11.78	9.04	9.59	8.55	8.29
$-E(sp^2)$[b]	9.98	10.11	7.37	7.63	6.96	6.76
$-E(sp^3)$[c]	9.38	9.69	6.96	7.14	6.56	6.34

a Calculated as $E(s^2p^1) = 2/3E_s + 1/3E_p$

b Calculated as $E(sp^2) = 1/3E_s + 2/3E_p$

c Calculated as $E(sp^3) = 1/4E_s + 3/4E_p$

be expected simply due to the fact that real space silicon density is increased by the introduction of Ga atoms. To measure the absolute N_v, nevertheless, is a non-trivial experiment.

The tetrahedral Si-Ga bonds do affect the VB-DOS by moving it toward the vacuum level. This will be disscussed in detail in Section 4.6.

4.3 Ga Coordination Numbers in Amorphous Silicon Determined by Core Level Photoemission Spectra

We have discussed in Chapter 2 that valence electron redistributions brought about by the forming of different chemical bonds will lead to changes in the core level binding energy, or a chemical shift. As gallium has an electronegativity of 1.13 (Phillips scale: Phillips 1973), which is lower than that of Si, at 1.41, we would expect the Ga3d core levels to shift to higher binding energy with the formation of Si-Ga bonds.

In Fig. 4.5, we show Ga3d core level spectra recorded on as-implanted and annealed c-Si samples The spectra become very faint on samples annealed at temperatures ≥ 500 °C, and the signal-to-noise ratio is too weak for any quantitative analysis. The Ga3d core levels were curve-resolved using a least-squares curve-fitting method. The input data for the Ga3d core level doublet are the spin-orbit splitting energy of 0.4 eV, an intensity ratio of $3d_{3/2}$ to $3d_{5/2}$ of 2:3, a full width at half maximum (FWHM) of the convolving function of 1.2 eV, and a Gaussian to Lorentzian mixing ratio of 0.6. The above parameters were found to best fit the experiment data, and were fixed for all Ga3d core levels.

In Fig. 4.5, the deconvoluted peaks are shown as dashed curves, which are the sums of the $3d_{3/2}$ and $3d_{5/2}$ spin-orbit doublets. The sums of these deconvoluted peaks are shown as dotted curves. The experimental data are shown as solid lines.

For as-implanted samples, two peaks, at binding energy of 18.8 and 19.5 eV, were found to best fit the experimental data, as shown in the figure. For annealed samples, however, three peaks at binding energies of 18.8, 20.0 and 21.1 eV (with an accuracy of 0.1 eV) were deconvoluted. The positions of each of these peaks were obtained from different samples and confirmed by measuring the energy difference between $Si2p_{3/2}$ and $Ga3d_{5/2}$ lines.

The peak at 18.8 eV corresponds to elementary gallium Ga^0(Bringans et al 1987). We assign the chemically shifted peaks at energies of 19.5 and 20.0 eV, to Ga^2 and Ga^3, which are two- and three-fold coordinated gallium bonded to Si, respectively. The chemical shifts of Ga^2 and Ga^3 of 0.7 and 1.2 eV are in good agreement with synchrotron radiation measurements (Bringans et al 1987) on Si surfaces covered with Ga. We interpret the peak at 21.1 eV with a chemical shift of 2.3 eV, as the 4-fold coordinated substitutional gallium Ga^4. We have pointed out in Chapter 3 that the sample surface contaminants are less than one atomic layer while the sampling depth of XPS is about 25 atomic layers . This makes it unlikely that the peak with a 2.3 eV chemical shift is due to Ga oxides. Further, the Ga oxides, if any, should have a chemical shift of 1.3 eV, as we reported elsewhere (Lu et al 1988, 1989).

The chemical shift per Si-Ga bond can be calculated by dividing the decovoluted chemical shift by the coordination numbers of the corresponding peak. This gives the chemical shift per Si-Ga bond of 0.35, 0.4, and 0.59 eV for Ga^2 ,Ga^3, and Ga^4, respectively. The significantly large shift per Si-Ga bond for Ga^4 state may be explained by its specific orbital properties. As a subsititutional dopant in the Si matrix, the Ga atom has to draw an extra electron from somewhere in the material to form the tetrahedral sp^3 hybrid orbital state Ga^4. The Ga^3, however, is believed to be a trigonal sp^2 hybrid in the amorphous silicon-CRN

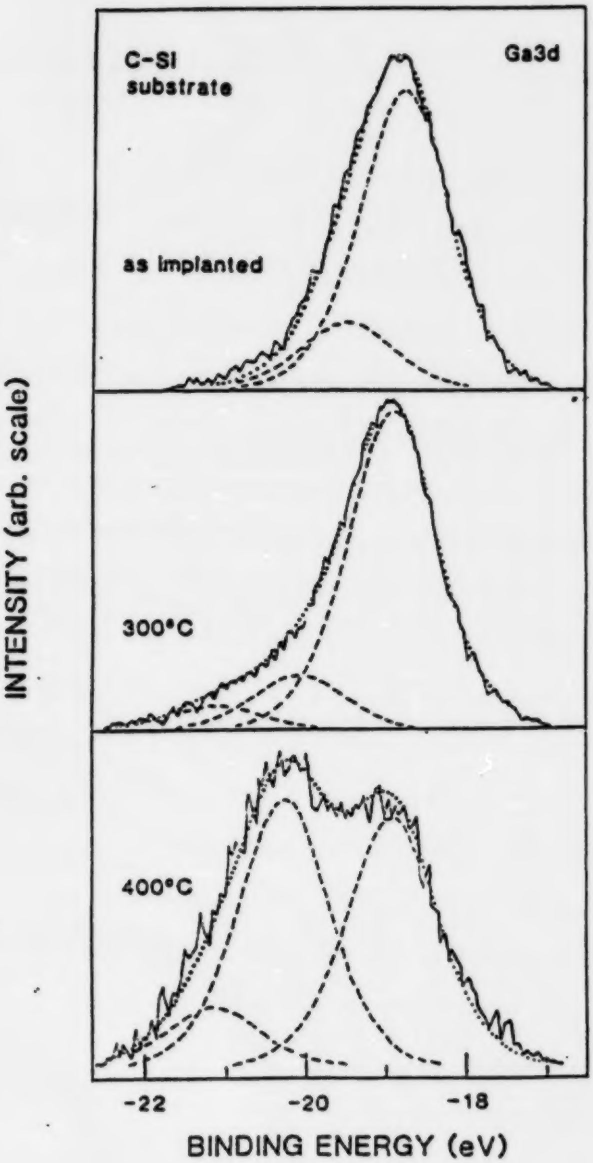

Figure 4.5: Ga3d core level spectra measured on c-Si samples, as-implanted, and annealed at 300 and 400 °C. The experimental signals are shown by solid line. The dashed curves show the results of deconvolution into different components and the dots are the sums of the components. Intensities are shown on an arbitary scale.

(Robertson 1983). It is well known that the electronegativity depends strongly upon the orbital hybrid state: since s electrons are bound more tightly than are p electrons, the electronegativity of an atom increases with the s character of the orbit (Huheey 1978). In Fig. 4.6. we show the electronegativities of carbon, nitrogen and oxygen as a function of s character. Electrons in an sp^3 hybrid with 25% s character. have a lower electronegativity than electrons in an sp^2 state with 33% s character. This means that Ga^4 will lose more electrons to Si atoms, which remain sp^3 hybridized. than does Ga^3. and consequently a larger chemical shift is expected from the tetrahedral Ga-Si bond. The smallest chemical shift of Ga^2 leads us naturally to think that it may be the linear sp hybrid.

The annealing activated. 3- and 4-fold coordinated. Ga are also observed on ion-implanted a-Si:H samples. In Figure 4.7. we show the Ga3d core level electron spectra recorded on ion-implanted and annealed a-Si:H. The three deconvoluted peaks correspond to (from right to left) Ga^0. Ga^3 and Ga^4 respectively. The binding energies and chemical shifts of these peaks are the same as those observed on c-Si samples.

It is interesting to note that most of the as-implanted Ga atoms are in the elementary state. along with very small amounts of Ga atoms 2-fold bonded to the damaged Si lattice. The 2-fold coodinated Ga configuration is an unstable state and disappears on annealing. Because of the amorphous nature of the ion-implanted and low temperature annealed ($\leq$ 400 °C) silicon lattice, the anneal-activated Ga atoms can occupy either 3- or 4-fold coordinated sites. This is due to large Si-Si bond-angle and bond-length deviations in the amorphous silicon CRN. For a well reconstructed crystalline silicon lattice after an anneal $\geq$ 500 °C. however. only tetrahedral Ga (aside from interstitial gallium) is allowed, due to topological constraints(see section 4.6).

It should be pointed out that Ga 3d signals from samples annealed at temperatures higher than 500 °C become too weak to be detected using normal data

	sp^3	sp^2	sp
C	2.48	2.75	3.29
N	3.68	3.94	4.67

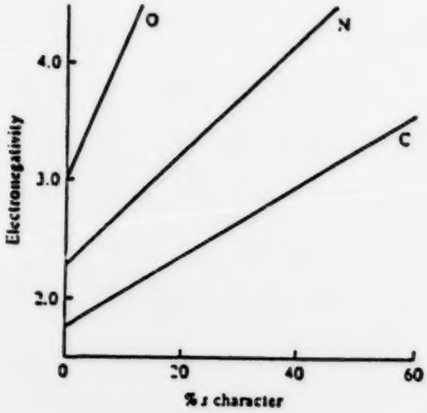

Figure 4.6: Electronegativities of carbon, nitrogen and oxygen as a function of percent s character(Hueey (1978)).

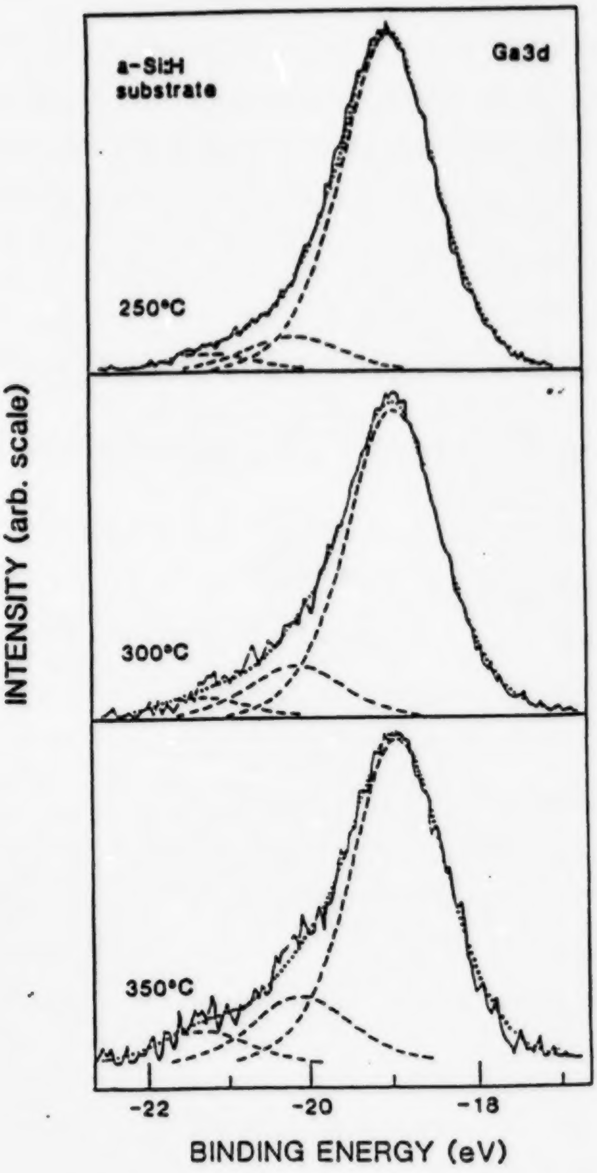

Figure 4.7: Ga3d core level spectra measured on ion-implanted and annealed a-Si:H samples. The experimental signals are shown by solid lines. The dashed curves show the results of deconvolution into different components and the dots are the sums of the components. Intensities are shown on an arbitary scale.

accumulation times (about one hour for an energy scan of 10 eV). We have not attempted to record Ga 3d spectra of those samples. In a similar study of As$^+$-implanted Si (with an As dose of ~ 3 at.%), Lau (1989) has found that it takes about 5 hours to record an As 3d core level spectrum with reasonable signal-to-noise ratio.

4.4 Activation of Ion-Implanted Ga Atoms and Doping Efficiency of Amorphous Silicon

In Table 4.3, we show the fractions of differently coordinated Ga in Si as well as the total Ga concentration shown in Figs. 4.5 and 4.7. In Fig. 4.8, we show the logarithm of Ga^3/Ga and Ga^4/Ga as a function of reciprocal annealing temperature. Ga^3/Ga and Ga^4/Ga, which means the fraction of 3-fold or 4-fold coordinated gallium, are obtained simply by dividing the intensity of the Ga^3 or Ga^4 peak by the sum of the intensities of all the deconvoluted peaks. From Table 4.3 and Fig. 4.8 we can see that both Ga^3 and Ga^4 concentrations increase with annealing temperatures, and that the number of activated Ga^3 atoms is approximately twice that of Ga^4 atoms, in both a-Si:H and c-Si samples, for the temperature range of 250 to 350 °C. The variations of Ga^3/Ga and Ga^4/Ga with annealing temperature T_a can be fitted to the form

$$Ga^{3,4}/Ga \propto e^{-E_a/kT_a} \tag{4.1}$$

where $Ga^{3,4}$ means either Ga^3 or Ga^4, and E_a is an activation energy. This yields an activation energy of 0.14±0.05 eV for both three- and four-fold coordinated Ga atoms over the temperature range of 250 to 350 °C.

Fortner and Lannin (1988) have reported an activation energy of 0.16 eV for the heat, H_{SR}, released upon structural relaxation during an anneal of ion-implanted Si and Ge, from room temperature to 325 °C. On the basis of Raman scattering

Table 4.3: Fractions of Differently Coordinated Gallium, (Ga^i/Ga), and Total Ga Concentrations, C, Measured after Annealing at Various Temperatures[a].

Ta (°C)	250	300	350	400
Ga^0/Ga	0.85	0.82 (0.78)	0.77	(0.43)
Ga^3/Ga	0.10	0.13 (0.14)	0.15	(0.47)
Ga^4/Ga	0.05	0.05 (0.08)	0.08	(0.10)
C (at.%)[b]	15 (15)	12 (11)	6	(9)

a) Values in parenthese are for c-Si; other values are for a-Si:H

b) The Ga concentration was determined by $Ga3d_{5/2}$ and $Si2p_{3/2}$ core level peak intensities with sensitivity factors of 0.31 and 0.25 respectively (Briggs and Seah 1983).

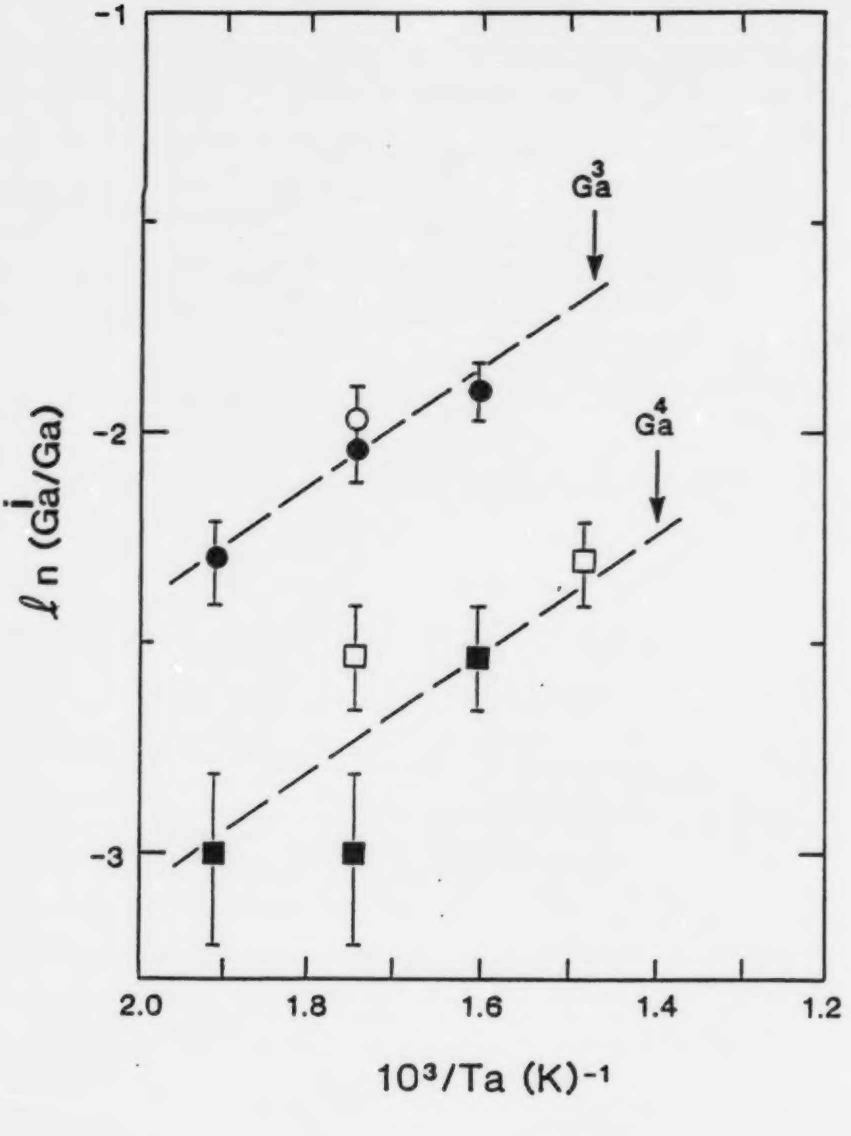

Figure 4.8: Variations of three- and four-fold coordinated Ga^i components (Ga^3/Ga and Ga^4/Ga) as a function of annealing temperature T_a. Data are measured on c-Si (solid circles and squares) and a-Si:H (open circles and squares).

experiments, they concluded that H_{SR} is the stored elastic potential energy released upon the relaxation of the bond angle deviation through the relation $H_{ij} = C(\Delta\theta_i^2 - \Delta\theta_j^2)$, where C is a constant, $\Delta\theta$ is the deviation, and i and j refer to the initial and final state in the annealing process.

The activation energy we found is quite close to that reported by Fortner and Lannin. This suggests that H_{SR} is the primary energy source promoting the Ga into sp^2 or sp^3 bonding states. This relaxation also affects the valence electron density of states spectra, as discussed above.

In Table 4.2, we show the energies of different orbital states. From the table we see that the energy difference between sp^2 and sp^3 is 0.49 eV, while the energy differences between the s^2p^1 state and sp^2 and sp^3, are 1.96 and 2.45 eV, respectively. It is possible that the barriers to s^2p^1-to-sp^2 and to $(s^2p^1 + e^-)$-to-sp^3 conversion might differ only slightly so that the activation energy of 0.14 eV is observed in both cases. The energy of the sp^2 orbit is lower than that of the sp^3 orbit. This may explain why the number of activated 3-fold coordinated Ga atoms is higher than that of substitutional gallium atoms.

One of the most important and most controversial physical parameters in amorphous semiconductors is the solid-phase doping efficiency, η_{sol}. This is defined as the number of donors or acceptors, which are presumably 4-fold coordinated dopants N_4(Robertson 1983, Stutzmann 1986), divided by the total dopant concentration N_o(Stutzmann 1986). That is, Ga^4/Ga in our studies. The core level spectral measurements in Table 4.3 indicate that η_{sol} varies from 5% to 10% for Ga concentrations ranging from 15 at.% to 6 at.%.

Various experimental techniques have been used deduce the doping efficiencies. EXAFS and NMR measurements on As and P in a-Si:H suggested that 4-fold coordinated donors could be as numerous as as 20% for samples with total concentrations around 1 at.% (Knights, Hayes and Mikkelsen 1977; Reimer and Duncan 1983). This is believed to be overestimated (Stutzmann 1986, Street et al

1988). Based on electrical measurements, however, Stutzmann (1986) and Jousse et al (1987) showed that the solid-phase doping efficiency is less than 10% for various dopants over a wide range of doping levels. We found that the doping efficiency estimated by Stutzmann and Jousse et al is consistent with our experiment results. That is, the doping efficiency is generally less than 10%.

4.5 Amorphous Silicon Doping Mechnism

In 1967, Mott introduced the "8-N" (N is the number of valence electrons) rule to account for the absence of doping in covalent, amorphous chalcogenide semiconductors. The suggestion was that element coordinations in an amorphous network satisfy their valence requirements locally in the absence of constraints due to periodicity: electrons are paired and the bond number n_c obeys the "8-N" rule, that is, $n_c=8-N$ for $N>4$ and $n_c=N$ for $N<4$. Thus the coordination of Si is 4, of Ga is 3, etc.. When, in 1975, Spear and LeComber showed that hydrogenated amorphous silicon (a-Si:H) could be substitutionally doped by the addition of small amounts of phosphine and diborane to the silane plasma, however, this discovery came as a surprise to many workers in the field. The "8-N" rule has since been regarded to be inadequate to explain the doping of amorphous Si and Ge. In 1982, Street proposed a modified "8-N" auto-compensation doping model. He proposed that the occurrence of 4-fold coordinated dopants is associated with the production of defects, in order to prevent a violation of the "8-N" rule for ionized doping impurities. He suggested that the Fermi level E_F is not able to move up the donor level during deposition because the occupied donor states would be in violation of the "8-N" rule. The auto-compensation doping model has been found unable to explain some experimental results, such as a constant doping efficiency at high dopant levels(Stutzmann, 1986; Stutzmann, Biegelsen and Street, 1987).

From XPS measurements, we have shown in previous sections that 3-fold and

4-fold coordinated Ga can co-exist in the amorphous Si CRN. The fraction of substitutional Ga is closely related to the local Si matrix topological arrangement and to the bond-angle distribution P(θ). This can be seen by the increasing fraction of 4-fold coordinated Ga with increasing annealing temperature. We have shown earlier that P(θ) is determined by the thermal history of the sample. For as-implanted amorphous silicon. the width $\Delta\theta$ of P(θ) is generally very large, and can be decreased through structural relaxation by an anneal. We assume that the dopants have only two possible configurations. sp^2 and sp^3. in an a-Si CRN: this is true for conventional gas-phase GD doped materials. The smaller the $\Delta\theta$ of the Si-Si bond-angle deviations in the tetrahedral Si CRN should give the larger the number of tetrahedral sp^3 dopant. and smaller the number of trigonal sp^2 dopant. In perfect crystalline silicon. $\Delta\theta = 0$. Therefore. Ga atoms are only permitted in substitutional sites (aside from interstitial ones). due to the constraints of periodicity. However. structural relaxation or Si-Si bond-angle ordering of the amorphous silicon CRN does not lead continuously to a crystalline structure. Various experiments. such as differential scanning calorimetry (DSC) (Roorda et al 1989). Raman scattering (Paesler et al 1983. Fortner et al 1988). neutron diffraction (Fortner and Lannin 1989). extended x-ray absorption fine structure (EXAFS) (Paesler et al 1989). and VB-DOS photoemission spectra (section 4.1 of this thesis) have shown that there exists a minimum Si-Si bond-angle deviation $\Delta\theta_{min}$, for which the amorphous silicon CRN is stable . prior to crystallization. This suggests that there should be a corresponding maximum number of subsitutional dopants or a maximum doping efficiency , η_{max}. in this most 'ordered' amorphous silicon. From our XPS measurement. and deductions from electrical measurements by Stutzmann (1986) and Jousse et al.(1987). we found that the solid-phase doping efficiency never exceeds 10 %. We therefore think that the highest doping efficiency (in terms of the fraction of the tetrahedrally bonded dopant) should be around 10 % .

Based on these experimental findings, we propose an alternative way of understanding doping in amorphous silicon, which leads to verifiable predictions of doping efficiency over a wide range of dopant concentrations. The model is based on two main propositions. The first is that when a dopant, say boron, is deposited on a growing a-Si surface, the B atoms may form either sp^2 (B_3^o) or sp^3 (B_4^-) configurations, as shown in Figure 4.9. The relative ratio of the two obviously depends upon the surface Si-Si bond struture, its time of relaxation, and the surface atom mobilities. These are mainly determined by deposition conditions such as substrate temperature and growth rate. We have shown in a previous section that the energy of an sp^2 orbital is lower than that of an sp^3. Therefore, the 3-fold coordinated structure is favored. The tendency of a dopant to occupy a hybrid orbital also depends on its electronegativity relative to that of silicon. According to Bent's rule (Bent 1960, 1961; Huheey, 1978), an sp^3 orbital, which has less s character than that of an sp^2 orbital, is favored when more electronegative substituents such B, P, etc. (see the electronegativities given in Table 4.4) are incorporated into a tetrahedral Si lattice, which we may regard as a "giant silicon molecule". This proposition can be expressed as

$$B_p \rightarrow (1-\alpha)B_3^o + \alpha B_4^- \tag{4.2}$$

where B_p is plasma phase boron and α is the probability of forming a 4-fold configuration.

The second proposition is that when the surface layer is buried into the subsurface and then bulk matrix with the growth of the film, a structural relaxation or Si-Si bond-angle ordering will take place in order to maintain a stable tetrahedral Si CRN. This suggests that bond-angle distortion at a B_3^o site will raise its energy, and it thereby becomes unstable. Heat released during structural relaxation then promotes the unstable B_3^o into a substitutional B_4^-, accompanied by creation of

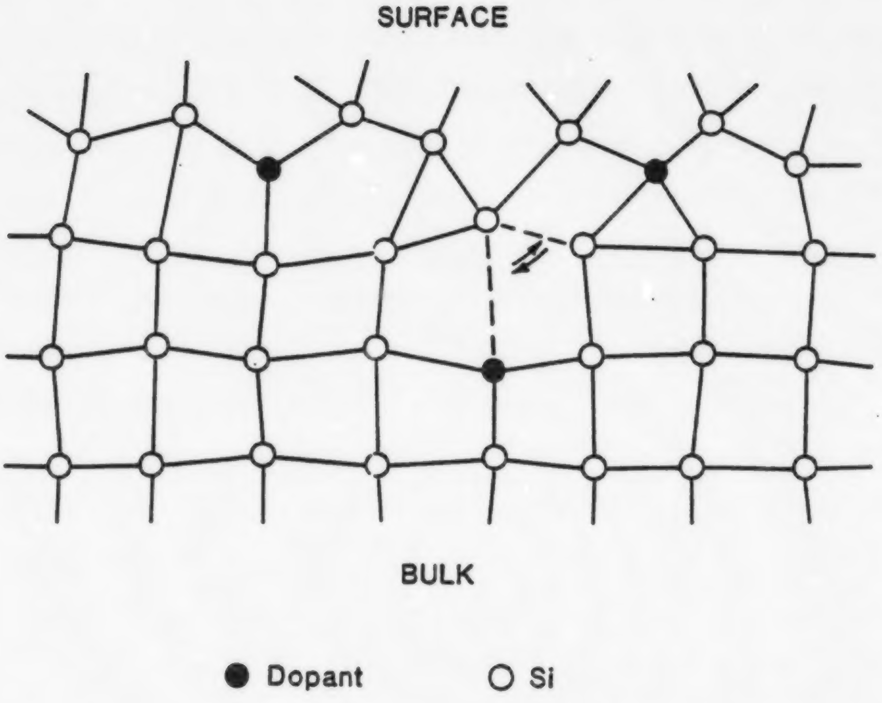

Figure 4.9: A two dimensional a-Si growth model for the incorporation of dopant. At the growing surface, two possible sites for the impurities are shown. At the subsurface, a 3-fold to 4-fold tranition along with the creation of one Si dangling bond is illustrated.

Table 4.4: Elemental Electronegativities of Nontransition Atoms in Tetrahedrally Coordinated Enviroments

Li	Be	B	C	N	O	F
1.00	1.50	2.00	2.50	3.00	3.50	4.00
Na	Mg	Al	Si	P	S	Cl
0.72	0.95	1.18	1.41	1.64	1.87	2.10
(0.9)	(1.2)	(1.5)	(1.8)	(2.1)	(2.5)	(3.0)
Cu	Zn	Ga	Ge	As	Se	Br
0.79	0.91	1.13	1.35	1.57	1.79	2.01
(1.9)	(1.6)	(1.6)	(1.8)	(2.0)	(2.4)	(2.8)
Ag	Cd	In	Sn	Sb	Te	I
0.57	0.83	0.99	1.15	1.31	1.47	1.63
(1.9)	(1.7)	(1.7)	(1.8)	(1.9)	(2.1)	(2.5)
Au	Hg	Tl	Pb	Bi		
0.64	0.79	0.94	1.09	1.24		
(2.4)	(1.9)	(1.8)	(1.8)	(1.9)		

• For the first row these have been scaled to agree with Pauling's definition. For other rows Pauling's values are also given (in parentheses)(after Phillips 1973).

one Si dangling bond T_3^+. as shown in Fig. 4.9. This means

$$B_3^o \rightarrow B_4^- + T_3^+ \tag{4.3}$$

However. an increased sustitutional dopant level can increase bond-length and bond-angle variations to the dopant surrounding Si-Si bonds, and consequently increasing Si CRN randomness. which means large Si-Si bond-length deviations. The tetrahedral Ga-Si bonds. for example. are responsible for the Si-Si bond-length and bond-angle deviations in crystalline silicon (see details in section 4.7). The tetrahedral As–Si–Si bond angle in crystalline silicon. has also been found to produce about a 3° deviation from the ideal Si–Si–Si bond-angle, as indicated by EXAFS measurements(Erbil et al 1986). So the B_3^o to B_4^- transition is maintained at a thermal equilibrium which is controlled by the a-Si CRN topological arrangement or bond-angle distribution function $P(\theta)$. Then. the above equation can be written as

$$B_3^o = B_4^- + T_3^+ \tag{4.4}$$

From the law of mass action. we have

$$N_3 = Const..N_4^2 \tag{4.5}$$

where N_4 is the substitutional B concentration promoted from trigonal B_3^o. along with same amount of silicon T_3^+ defect created. The solid-phase doping efficiency η_{sol} is then given by

$$\eta_{sol} = (\alpha N_o + N_4)/N_o = \alpha + const..N_3^{1/2}/N_o \tag{4.6}$$

where N_o is the total solid-phase dopant concentration. As the doping efficiency is generally very low, we can make the aproximation $N_o \approx N_3$. We know that α is only related to the dopant's chemical properties and deposition conditions. Therefore η_{sol} can be expressed as

$$\eta_{sol} = \alpha(Z,\kappa) + \beta(Z,P(\theta)) \cdot N_a^{-1/2} \tag{4.7}$$

where $\alpha(Z,\kappa)$ and $\beta(Z,P(\theta))$ are constants related to the doping element Z (group III and V elements), deposition parameter κ, and the Si CRN bond-angle distribution function, $P(\theta)$.

The above equation indicates that the doping efficiency of all group III and V dopants, will be dominated by the square-root term at low dopant concentrations. A constant value is expected at higher dopant concentrations. The experimental variations of doping efficiency with dopant concentrations are shown in Figure 4.10 (Stutzmann, 1986). The results indicate that η_{sol} has a square-root relation for B and P in a-Si:H and P in a-Ge:H, and a constant value for As in a-Si:H and B in a-Ge:H over the dopant range measured. This is in excellent agreement with the predictions of our doping model.

As we have discussed above, the B_3^0 to B_4^- transition is related to adjustments in the bond-angle distribution, $P(\theta)$. Therefore a decrease in the width, $\Delta\theta$, of $P(\theta)$ will lead to an increase in doping efficiency. It has been reported that a-Si:H films deposited at low temperature possess larger $\Delta\theta$ than those deposited at high temperature, and $\Delta\theta$ can be reduced by post-annealing (Beeman 1985; Paesler et al 1983; Tsu et al 1984). Fiorini et al (1987) have found a significant increase in doping efficiency by annealing low temperature deposited a-Si:H. This, in our view, is due to an increasing $\beta(Z,P(\theta))$ induced by annealing, which narrows the bond-angle distribution function $P(\theta)$ of the Si CRN.

Eq.(4.4) indicates that creation of a 4-fold coordinated acceptor from a 3-fold coordinated boron is accompanied by the creation of one defect. Such a dopant-defect pair formation or auto-compensation mechanism was first proposed by Street (1982), but based on a very different physical principle. That is, Street suggested that the transition between B_3^0 and B_4^- is controlled by the carrier Fermi level E_F. However, we believe that the fraction of substitutional dopant is

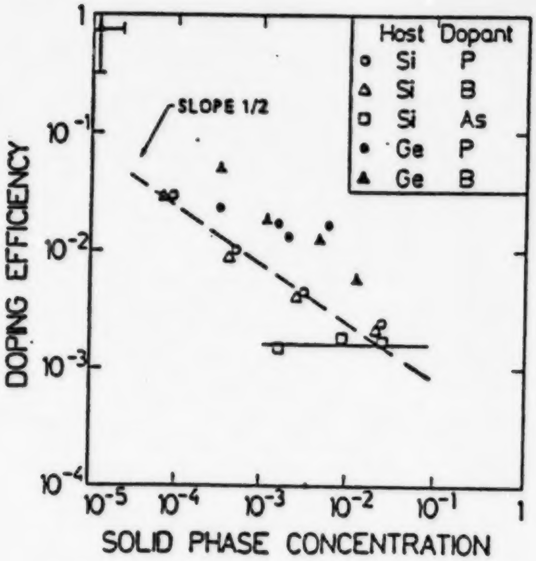

Figure 4.10: Doping efficiency for P. As and B in glow discharge deposited a-Si:H and a-Ge:H as a function of the dopant concentration in the solid-phase(from Stutzmann (1986)).

determined by the Si amorphous CRN bond-angle distribution function P(θ).

4.6 Supersaturated Substitutional Ga in Crystalline Silicon Studied by Si 2p Core Level Spectra

In Figure 4.11, we show the Si 2p core level spectra recorded on ion-implanted c-Si samples annealed at temperatures from 500 to 900 °C. Binding Energies are aligned at 99.6 eV. The Si 2p spin-orbit doublet with an energy separation of 0.60 eV and intensity ratio of 1:2 is well described by a mixed Lorentzian (0.8) and Gaussian (0.2) convolution function. The FWHM of the convolution function ranges from 0.8 to 0.7 eV, depending upon the Ga-induced strains. The strains and static charge fluctuations in the c-Si lattice will be discussed in detail in the next section.

Two Si 2p doublets, one at 99.6 eV and the other, shifted by 0.6 eV to 99.0 eV, are deconvoluted for samples annealed at temperatures ranging from 500 to 800 °C, as shown in the figure. Only one doublet, at 99.6 eV is found to best fit the experiment data for samples annealed at 900 °C. The peak at 99.6 eV binding energy is from Si atoms which are normally bonded to 4 other Si atoms in a c-Si lattice. The peak with a chemical shift of 0.6 eV to low binding energy is interpreted as being due to the Si which is bonded to three other Si, and to one tetrahedrally coordinated Ga. This is based on the following: First, the good crystalline structure of the solid-phase regrown silicon lattice makes other Ga bonding formulas such as the trigonal sp^2 hybrid, very unlikely. Second, we can exclude the possibility that the peak is due to $SiGa_2$, $SiGa_3$ or $SiGa_4$ clusters , as shown in Figure 4.12, because the probability of those arrangements is very small in comparison to the isolated Ga-in-Si structure of Fig. 4.11(d).

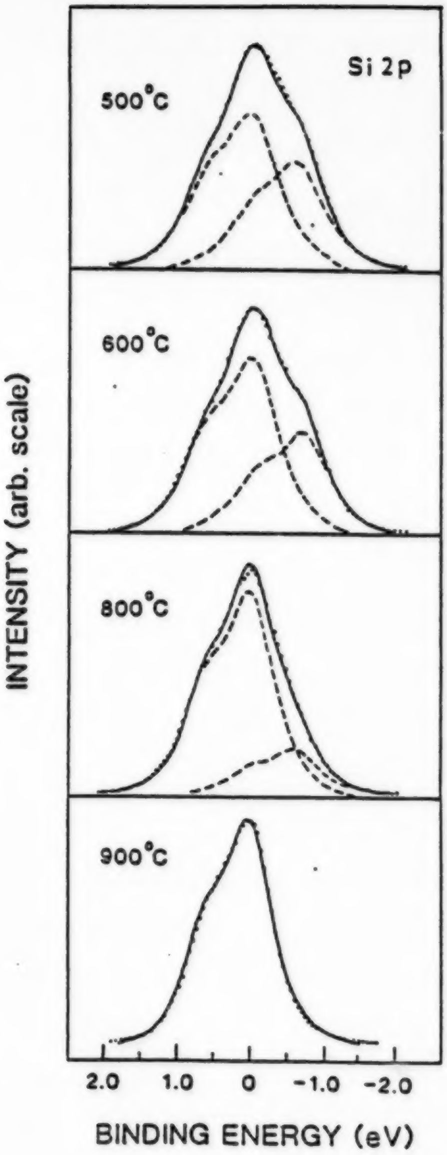

Figure 4.11: Si2p core level spectra recorded on Ga$^+$-implanted c-Si samples after being annealed at various temperatures. The data points are shown as dots. The dashed curves show the bulk and chemically shifted peaks and the solid curve is the sum of the two components. Intensities are shown on an arbitary scale and binding energies are aligned to 99.6 eV.

and only one chemically shifted peak is observed. A quantum chemical ab-initio calculation of the isolated substitutional Ga-in-Si structure model indicates that this Ga configuration should produce a Si 2p core level shift of 0.6 - 0.7 eV toward lower binding energy(Selmani 1989). in excellent agreement with the experimental result.

No indication of a Si 2p core level shift has been found for samples annealed at low temperature(≤400 °C). From Ga 3d core level measurements on these samples, we have shown that only a small fraction of gallium is in the tetrahedral sp^3 state. the majority being in either a 3-fold coordinated trigonal sp^2 hybrid or an interstitial elementary state Ga^0. The broadened Si 2p peak makes the Si-Ga bond-induced shift too small to be resolved. The correlation between Si 2p core level FWHM and valence shell static charge fluctuations will be the subject of a comprehensive discussion in the next session.

The tetrahedrally coordinated gallium concentration is determined by measuring the intensity ratio of Si2p(-Ga)/Si2p. where Si2p(-Ga) and Si2p mean the shifted and total spectra intensity. respectively(the first row of Table 4.5). and dividing by 4 (4 Si-Ga bonds for each Ga atom). The results are shown in the second row of Table 4.5. where we can see that 10 at.% substitutional Ga has been obtained after annealing at 500 °C. We also see that the Ga concentration decreases with increasing annealing temperatures. to a value too low to be detected by XPS after an anneal at 900 °C. We explain this as due to increased silicon lattice structural relaxation at increased annealing temperature. This releases the Si-Ga bond-induced strains: that is. it reduces the Ga induced bond-angle and -length deviations of the surrounding Si-Si bonds. This process is accompanied by an evolution of heat. Consequently. the substitutional Ga atoms are excluded from the lattice and diffuse. This hypothesis is strongly supported by the observation of an activation energy of 0.2(±0.1) eV in an Arhenius plot of the Ga concentration and annealing temperature. as shown in Fig. 4.13. A comparable

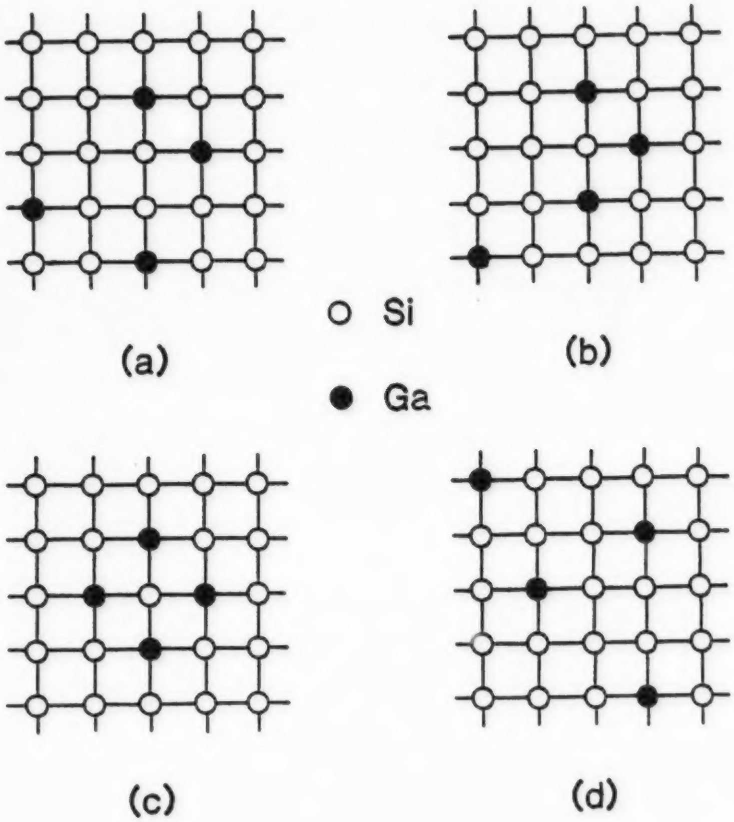

Figure 4.12: A two dimentional model of four different possible Ga-in-Si configurations; cases (a), (b) and (c) correspond SiGa$_2$, SiGa$_3$ and SiGa$_4$ clusters, respectively; case (d) is the isolated Ga-in-Si structure.

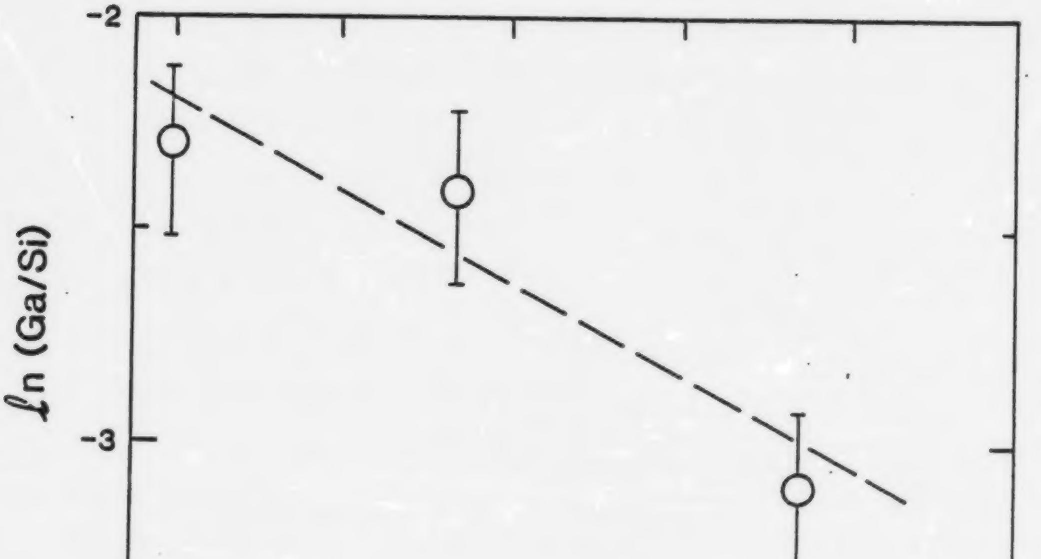

Figure 4.13: Arrhenius plot of the substitutional gallium and annealing temperature.

activation energy of 0.16 eV has been reported by Fortner and Lannin (1988) in the exothermic bond-angle ordering process. by annealing Ar^+-implanted Si and Ge. The same physical mechanism. as we have discussed in section 4.4, is responsible for the promotion of trigonal and tetrahedral Ga from the elementary as-implanted state at low annealing temperatures.

Several reseach groups have reported (Matsuo et al 1987: Harrison et al 1987: Lin et al 1988) that the hole-carrier levels of Ga^+-implanted Si, at doses over the Ga solid solubility limit in Si. decrease with increasing annealing temperatures higher than 600 °C. This "abnormal" activation behaviour of Ga-in-Si, however. can be easily understood from our data. That is. strains produced by the supersaturated substitutional Ga are released at increased annealing temperatures. excluded the Ga from the substitutional sites. and consequently there is a reduction of hole-carrier levels.

The valence-band density-of-state (VB-DOS) spectra of these samples recorded at the same time were shown in Fig. 4.3. The valence band maxima (VBM) were determined in the usual way (Ley 1984). through the extrapolation of the steepest descent of the leading edge of the VB-DOS. We measured the binding energy difference between the Si $2p_{3/2}$ core level and the VBM. and found it changed significantly, while the width of the VB remained unchanged.

It is interesting that the binding energies of Si 2p levels of those samples vary randomly less than 0.2 eV. in reference to the Fermi level of the spectrometer. This is mainly due to the statistical fluctuations and sample surface charge or contamination level variations.

The shift towards vacuum level of the VBM, ΔE_{VBM}, relative to a virgin silicon sample, is given in Table 4.5. This shift cannot be due to surface band bending, as band bending will move both the core level and VB-DOS in the same direction. We attribute the shift on samples annealed at 300 °C to the amorphous nature of the damaged layer. The same shift has been found on as-implanted Si samples and

Table 4.5: XPS Data for Ga$^+$-Implanted c-Si as a Function of RTA Temperature.

RTA Temperature (°C)	300	400	500	600	800	900	Virgin Si(100) (0.003-0.007Ωcm)
Si(-Ga)/Si			0.41	0.36	0.18	0.0	
Ga/Si (at.%)			10	9	4.5	0	
ΔE_{VBM} (eV)	0.4	0.1	0.7	0.6	0.1	0.0	0(reference)
LEED Pattern observed	no	no	yes	yes	yes	yes	

also on sputtered a-Si (Ley 1984). The recession of the VBM for samples annealed at 400 °C again suggests that the Si lattice has been partially reconstructed, as we have discussed in section 4.2. However. ΔE_{VBM} increases drastically, as does the substitutional Ga concentration. on samples annealed at temperatuires higher than 500 °C (see Table 4.5). We believe these shifts to be due to Si-Ga bonding states, which induce a shift of the Si valence electrons to lower binding energy. In comparison. Si-H bonds are found. by both photoemission spectroscopy and various band calculations (Ley 1984). to produce a VBM recession, consequently enlarging the energy band gap as the conduction band minimum (CBM) remained unaffected by the Si-H anti-bonding states. Unforturnately. based on current experiments, we are unable to determine whether the CBM is changed by Si-Ga anti-bonding states. There are no corresponding energy band calculations available at the time of writing. However. other experimental studies on Al. which also has a lower electronegativity than that of Si, show that Al can narrow the a-Si:H energy band gap at concentrations higher than 3 at.% (Thompson and Reinhard 1980: Lu 1986: Liu and Lu 1986: Saito et al 1989). This suggests that the c-Si energy band-gap might be narrowed by the supersaturated subsitutional Ga.

The surface crystallinity of the implanted and annealed samples was examined by LEED measurements. The results are given in table 4.5. The observation of LEED patterns on Ga^+-implanted c-Si after annealing at temperatures ≥ 500 °C, suggests that SPE regrowth of the damaged layer has been extended to the surface, in good agreement with VB-DOS measurements.

4.7 Static Charge Fluctuations in Si

We have shown in the previous section that the FWHM of the Si 2p core levels decreases with increasing annealing temperatures. This is shown in Table 4.6.

As the data were collected under identical instrument conditions, the FWHM contributed by X-ray source and electron energy analyser should be the same. So the symmetric broadening of Si 2p core levels in ion-implanted and annealed samples, measured under identical instrument conditions, is due to the static charge fluctuations in the valence shell electron distributions, as it is in sputtered a-Si (Ley 1982) and silicon oxides (Grunthaner 1987). The valence shell electron fluctuations, which means either electron rich or lean in compared to ideal charge distributions in the Si valence shell, will cause the core levels to shift on both sides of the ideal peak position. The broad peak observed, therefore, is actually the sum of all these shifted and unshifted peaks. We can write such interpretation as

$$f(E,\zeta) = B \cdot f(E,\zeta_o) + \sum_{E_i \neq E} C_i \cdot f(E_i,\zeta_o) \qquad (4.8)$$

where $f(E,\zeta)$ is the convolution function with binding energy E and FWHM ζ; ζ_o is the FWHM measured on virgin c-Si under identical instrument conditions, i.e., 0.7 eV. E_i is the binding energy of those silicon atoms with valence charge deviation of Δq_i. B and C_i are the corresponding spectra intensities. As an approximation, we may rewrite the above equation as

$$f(E,\zeta) \approx B \cdot f(E,\zeta_o) + C \cdot f(E + \Delta E_{rms},\zeta_o) + C \cdot f(E - \Delta E_{rms},\zeta_o) \qquad (4.9)$$

where B, C and ΔE_{rms} can be determined using a least-square fitting of the sum of right-hand terms to the left-hand term, for a given ζ and E. The goodness of fit obviously depends on the value of ζ. The physical meaning of the above equation is that the overall effects of these Si atoms with valence charge fluctuation of Δq_i and with core level chemical shift of $(E - E_i)$ are summarized as Si atoms with a percentage of 2C/B, and with a mean charge fluctuation of Δq_{rms}, which causes the same core level shift of ΔE_{rms}. The two terms with opposite signs of chemical shifts represent the observed symmetric broadening of the 2p core levels.

It has been reported (Grunthaner et al 1979) that the loss or gain of one electron in the Si valence shell will lead to a 2p core level shift of 2.2 eV. We know that the chemical shift is related to charge transfer through eq.(2.10). Therefore. the mean static charge fluctuations Δq_{rms} on each Si atom can be estimated by $2C\cdot\Delta E_{rms}/2.2B$. The calculated Δq_{rms} and corresponding ζ are given in Table 4.6.

From the table we see that a large FWHM value of 1.0 eV for samples annealed at or below 400 °C. yields a static charge fluctuations of 0.11 electrons units rms. The same amount of Δq_{rms} in sputtered a-Si was reported by Ley et al (1982) using a different method of estimation. A value for Δq_{rms} of 0.2 electrons on atoms of an amorphous silicon cluster was also calculated by Guttman et al (1980). This indicates that static charge fluctuations in these samples are due to the unreconstructed Ga^{+}-ion amorphized Si lattice, in good agreement with VB-DOS and LEED measurement results.

For samples annealed at or above 500 °C. a significant amount of Ga has been promoted to substitutional sites in a well reconstructed Si lattice. The static charge fluctuations in these samples is explained as largely being due to substitutional Ga. This is understandable. As the Si-Ga bond-length (2.398 Å) is larger than that of Si-Si bond (2.346 Å) (Phillips 1973) in pure silicon, the substitutional Ga will induce bond-angle and bond-length deviations in the first. second. or further neighbor Si-Si bonds. Consequently. the bond-angle and bond-length deviations will lead to Si valence shell charge distribution fluctuations as indicated by the calculation (Guttman et al 1980).

Table 4.6: Calculated Static Charge Fluctuations in Ga^{+}-Implanted Si as a Function of Annealing Temperature.

RTA Temperature (°C)	300	400	500	600	800	900	Virgin Si(100) (0.003-0.007Ωcm)
FWHM (eV)	1.00	1.00	0.80	0.75	0.72	0.70	0.70
Ga/Si (at.%)			10	9	4.5	0	
$\langle \Delta q \rangle$ ($\lvert e \rvert$)	0.11	0.11	0.04	0.02	0.003		

Bibliography

[1] Appelbaum, J.A., Hamann, D.R. (1976) *Rev. Mod. Phys.*,**48**, 479; (1978),*Crit. Rev. Sol. State Sci.*,**6**, 357.

[2] Beeman, D., Tsu, R., and Thorpe, M.F.(1985) *Phys. Rev.* **B**, **32**, 874.

[3] Bent, H.A.(1960) *J. Chem. Phys.*,**33**, 1258; (1961) *Chem. Rev.*,**61**, 275.

[4] Bose, S.K., Winer, K., and Anderson, O.K.(1988) *Phys. Rev.* **B**,**37**, 6262.

[5] Brebner, J.L. et al(1985) *Can. J. Phys.*, **63**, 786.

[6] Briggs, D., and Seah, M.P.(1983) in *Practical Surface Analysis by Auger and X-ray Photoelectron Spectroscopy*, edited by D. Briggs and M.P. Seah, (John Wiley & Sons, New York), p.511.

[7] Bringan, R.D., Olmstead, M.A., Uhrberg, R.I.G., and Bachrach, R.Z.(1987) *Phys. Rev.* **B**, **36**, 9569.

[8] Burrows, V.A., Chabal, Y.J., Higashi, G.S., Raghavachari, K., and Christman, S.B. (1988) *Appl. Phys. Lett.*,, **53**, 998.

[9] Cardona, M., and Ley, L.(1978) in *Photoemission in Solids I*, edited by M. Cardona and L. Ley, (Springer-Verlag, New York), p.1.

[10] Chabal, Y.J., Higashi, G.S., and Raghavachari, K.(1989) *J. Vac. Sci. Technol.* **A**, May(in press).

[11] Chen P.W.(1985) in *Handbook of University Physics*, edited by Chen P.W. (Xinhua, Shandong), p.433.

[12] Ching, W.Y., Ling, C.C., and Huber, D.L.(1976) *Phys. Rev.* **B**, **14**, 620.

[13] Ching, W.Y., Ling, C.C., and Guttmann, L.(1977) *Phys. Rev.* **B**, **16**, 5488.

[14] Donovan, E.P., Spaepen, F., Turnbull, D., Poate, J.M., and Jacobson, D.C.(1984) *J. Appl. Phys.*, **57**, 1795.

[15] Eastman, D.E., Heimann, P., Himpsel, F.J., Reihl, B., Zehner, D.M., and White, C.W.(1981) *Phys. Rev.* **B. 24**. 3647.

[16] Elliott, S.R.(1983) *Physics of Amorphous Materials*, Longman, London, p.94.

[17] Fenner, D.B.,Biegelsen, D.K., Bringans , R.D., and Krusor, B.S. (1989a) *Materials Research Society Symposium Proceedings*, San Diego, April 24-29 (in press).

[18] Fenner, D.B., Biegelsen, D.K., Bringans, R.D. (1989b) *J. Appl. Phys.*, July (in press).

[19] Fiorini, P., Haller, I., Nocera, J.J., Cohen, S.A., and Brodsky, M.H.(1987) *J. Appl. Phys.*, **62**. 1425.

[20] Forstmann, F. (1977) in *Photoemission from Surfaces*, edited by B. Feuerbacher, B. Fitton, R.F. Willis(Wiley, New York), Chap.8.

[21] Fortner, J. and Lannin, J.S.(1988) *Phys. Rev.* **B**, **37**. 10154.

[22] Fortner, J. and Lannin, J.S.(1989) *Phys. Rev.* **B**, **39**. 5527.

[23] Fritzche, H.(1984) in *Semiconductors and Semimetals*, edited by J.I. Pankove, (Academic Press, New York), vol.21C, p.309.

[24] Ghosh, P.K.(1983) *Introduction to Photoelectron Spectroscopy*, John Wiley and Sons, New York, p.161.

[25] Graf, D., Grundner, M., and Schulz, R.(1989) *J. Vac. Sci. Technol.* **A**, May(in press).

[26] Grunthaner, F.J., Grunthaner, P.J., Vasquez, R.P., Lewis, B.F., Maserjian, J., and Madhukar, A. (1979) *Phys. Rev. Lett.*, **43**, 1683.

[27] Grunthaner, P.J., Hecht, M.H., Grunthaner, F.J., and Johnson, N.M. (1987) *J. Appl. Phys.*, **61**. 629.

[28] Guttman, L., Ching, W.Y., and Rath, J. (1980) *Phys. Rev. Lett.*, **44**, 1513.

[29] Harrison, H.B., Iyer, S.S., Sai-Halasz, G.A., and Cohen, S.A. (1987) *Appl. Phys. Lett.*, **51**, 992.

[30] Harrison, W.A.(1981) *Phys. Rev.* **B**, **24**. 5835.

[31] Huheey, J.E.(1978) *Inorganic Chemistry*, 2nd ed., (Harper and Row, New York), p.159.

[32] Jacobsen, D.C., Poate, J.M., Eaglesham, D.J., and Chen, H.S. (1989) *Materials Research Society Symposium Proceedings*, San Diego, April 24-29 (in press).

[33] Joannopoulos, J. and Cohen, M.H.(1976) *Solid State Phys.* **31**, edited by H. Ehrenreich, F. Seitz, and D. Turnbull, (Academic , New York).p.71.

[34] Jousse, D., Bruyere, J.C., Bustarret, E., and Deneuville, A. (1987) *Phil. Mag. Lett.*, **55**, 41.

[35] Knights, J.C., Hayes, T.M., and Mikkelsen, Jr., J.C.(1977) *Phys. Rev. Lett.*, **39**, 712.

[36] Kazahaya, T., and Hirose, M.(1986) *Japan. J. Appl. Phys.*, **25**, L75.

[37] Lang, B., and Taofik, A.(1986) *Appl. Phys.* **A**, **39**, 95.

[38] Lau, W.M.(1989), private communication.

[39] Ley, L., Kowalczyk, S.P., Pollak, R.A., and Shirley, D.A.(1972). *Phys. Rev. Lett.*, **29**, 1088.

[40] Ley, L., Reichardt, J., and Johnson, R.L. (1982) *Phys. Rev. Lett.*, **49**, 1664.

[41] Ley, L. (1984a) in *The Physics of Hydrogenated Amorphous Silicon II*, edited by J.D. Joannopoulos and G. Lucovsky, (Springer-Verlag, New York), p.61 and references therein.

[42] Ley, L.(1984b) In *Semiconductors and Semimetals*, edited by J.I. Pankove, (Academic Press, New York), vol.21B, p385.

[43] Lin, C.M., Steckl, A.J., and Chow, T.P. (1988) *Appl. Phys. Lett.*, **52**, 2049.

[44] Liu, J.M. and Lu, Z.H. (1986) *Proc. of 2nd Intern. Photovolt. Sci. and Eng. Conf.*, Beijing, p.537.

[45] Lu, Z.H. (1986) *M.S. Thesis*, Yunnan University.

[46] Lu, Z.H., Lagarde, C., Currie, J., and Yelon, A. unpublished.

[47] Lu, Z.H., Sacher, E., and Yelon, A.(1988) *Phil. Mag.*, **58**, 385.

[48] Lu, Z.H., Sacher, E., Selmani, A., and Yelon, A.(1989a) *Appl. Phys. Lett.*, **54**, 2665.

[49] Lu, Z.H., Largade, C., Sacher, E., Currie, J., and Yelon, A. (1989b) *J. Vac. Sci. Technol.* **A**, **7**, 646.

[50] Lu, Z.H., Azelmad, A., Trudeau, Y., and Yelon, A.(1989c) *Appl. Phys. Lett.*, **55**, 846.

[51] Margaritondo, G. and Weaver, J. (1985) in *Solid State Physics: Surfaces*, edited by L. Park and M.G. Lagally, (Academic Press, New York), p.131.

[52] Matsuo, J., Kato, I., Horie, H., Nakayama, N., and Ishikawa, H. (1987) *Appl. Phys. Lett.*, **51**, 2037.

[53] Michel, E., Kastl, R.H., Mader, S.R., Masters, B.J. and Gardener, J.A. (1984) *Appl. Phys. Lett.*, **44**, 404.

[54] Mott, N.F.(1967) *Adv. Phys.*, **16**, 49.

[55] Nakazawa, M., Nishioka, Y., Sekiyama, H., and Kawase, S.(1989) *J. Appl. Phys.*, May(in press).

[56] Ortenburger, I.R., Rudge, W.E., and Herman, F.(1972). *J. Non-Cryst. Solids*, **8-10**, 653.

[57] Paesler, M.A., Sayer, D.E., Tsu, R., and Hermandez, J.G.(1983). *Phys. Rev.* **B**, **28**, 4550.

[58] Pankove, J.I.(1984) *Semiconductors and Semimetals*, edited by J.I. Pankove (Academic, New York), vol21A-C. In these four volumes, both the physical and technical aspects of hydrogenated amorphous silicon were critically reviewed by numerical experts in this field.

[59] Pauling, L. (1967) *The Nature of the Chemical Bond*, (Cornell Univ. Press, New York).

[60] Phillips, J.C.(1973) *Bonds and Bands in Semiconductors*, (Academic Press, New York & London), p.54.

[61] Reimer, J.A., and Duncan, T.M.(1983) *Phys. Rev.* **B**, **27**, 4895.

[62] Robertson, J.(1983) *Phys. Rev.* **B**, **28**, 4666.

[63] Roorda, S., Doorn, S., Sinke, W.C., Scholte, P.M.L.O., and van Loenen, E. (1989) *Phys. Rev. Lett.*, **62**, 1880.

[64] Sacher, E., Klemberg-Sapieha, J., Wertheimer, M.R., Schreiber, H.P. and Groleau, R.(1984) *Phil. Mag.*, **B**, **49**, L47.

[65] Saito, N., Tomioka, Y., Yamaguchi, T., and Kawamura, K.(1989) *Phil. Mag. Lett.*, **59**, 43.

[66] Selmani, A.(1989) to be published.

[67] Shirley, D.A. (1972) *Phys. Rev.* **B. 5.** 4709.

[68] Siegbahn, K., Nordling, C., Fahlman, A., Nordberg, K., Hamrin, K., Hedman, J., Johansson, G., Bergmark, T., Karlsson, S.E., Lindgren, I., and Lindberg, B. (1967) *ESCA: Atomic, Molecular and Solid State Structure By Means of Electron Spectroscopy*, (Almqvist and Wiksells, Uppsala), p.71.

[69] Spear, W.E. and LeComber, P.G.(1975) *Solid State Commun.*, **17**, 1193.

[70] Spicer, W.E. (1958) *Phys. Rev.*, **112**, 114.

[71] Stern, Z.A., Bouldin, C.E., Von Roedern, B., and Azoulay, J. (1983) *Phys. Rev.* **B, 27**, 6557.

[72] Street, R.A.(1982) *Phys. Rev. Lett.*, **49**, 1187.

[73] Stutzmann, M.(1986) *Phil. Mag.* **B, 53**, L15.

[74] Stutzmann, M., Biegelsen, D.K., and Street, R.A.(1987) *Phys. Rev.* **B, 35**, 5666.

[75] Swartzentruber, B.S., Mo, Y.W., Webb, M.B., and Lagally, M.G. (1989) *J. Vac. Sci. Technol.* **A.** (in press).

[76] Thompson, M.G., and Reinhard, D.K. (1980) *J. Non-Cryst. Solids*, **37**, 325.

[77] Tsu, R., Hermandez, J.G., and Pollak, F.H.(1984) *J. Non-Crys. Solids*, **66**, 109.

[78] Vasquez, R.P., Madhukar, A. and Tanguay, A.R.(1985) *J. Appl. Phys.*, **58**, 2337.

[79] Wach, W. and Wittmaack, K.(1983) *Phys. Rev.*, **B, 27**, 3528.

[80] Weaire, D. and Thorpe, M.F.(1971) *Phys. Rev.* **B, 4**, 2548, 3517.

[81] Wertheim, G.K. (1978) in *Electron and Ion Spectroscopy of Solids*, edited by L. Fiermans, J. Vennik and W. Dekeyser, (Plenum Press, New York), p.192.

[82] Winer, K.(1987) *Phys. Rev.* **B, 35**, 2366.

[83] Ziegler, J.F., Biersack, J.P. and Littmark, U.(1985) *The Stopping and Range of Ions in Solids*, Pergamon Press, New York.

APPENDIX B

Members of the Thin Film Group (GCM)

INTRODUCING THE G.C.M.

The GCM, the "Groupe des couches minces" or "Thin Film Group" is a group of scientists belonging to three different laboratories in two institutions: l'Université de Montréal and l'Ecole Polytechnique, which is the engineering school affiliated with the University of Montreal. These are the solid state and nuclear physics laboratories at the Université de Montréal, and the solid state physics laboratory of the Ecole Polytechnique.

The GCM began its activities in 1980 and became an official organization of the sponsoring institutions in 1984. It presently consists of 17 senior members, 16 research staff and technicians, and close to 50 graduate students.

The main objective of the GCM is to do high quality fundamental and applied research on the physics of thin films and on the applications of these films. Much of this work is applicable to industrial needs.

The GCM spectrum of activities is quite broad. It ranges from fabrication of new materials and of electronic, and integrated optical devices, to various nuclear, physicochemical, electrooptical as well as plasma techniques for materials processing and characterization studies. In addition, some members of the GCM are involved in theoretical analysis of numerous properties of materials and devices.

At present, the senior members of the GCM are:

Name	Affiliation
Brebner, John L.	Physics Université de Montréal
Cochrane, Robert W.	Physics Université de Montréal
Currie, John F.	Engineering physics École Polytechnique
Gujrathi, Subhash	Nuclear Physics Laboratory Université de Montréal
Hamel, Louis-André	Nuclear Physics Laboratory Université de Montréal
Hinrichsen, Peter	Nuclear Physics Laboratory Université de Montréal
Houdayer, Alain	Nuclear Physics Laboratory Université de Montréal
Leonelli, Richard	Physics Université de Montréal
Lépine, Yves	Physics Université de Montréal
Lewis, Laurent	Physics Université de Montréal
Masut, Rémo	Engineering Physics

	École Polytechnique
Meunier, Michel	Engineering Physics Ecole Polytechnique
Najafi, Iraj	Engineering Physics École Polytechnique
Sacher, Edward	Engineering Physics École Polytechnique
Vasilopoulos, Panagiotis	Engineering Physics École Polytechnique
Wertheimer, Michael R.	Engineering Physics École Polytechnique
Yelon, Arthur	Engineering Physics École Polytechnique